POLITECNICO DI MILANO

SCHOOL OF INDUSTRIAL AND INFORMATION ENGINEERING
Department of Chemistry, Materials and Chemical Engineering "G. Natta"
Master Degree in Materials Engineering and Nanotechnology

Characterisation of Rare Earth Oxide/III-V Nitride semiconductor systems for electronic applications

Candidate:
Sara Iacopetti
Matricola 837811

Supervisor:
Prof. Carlo Casari

External Supervisor:
Prof. Moshe Eizenberg

Academic Year 2015/2016

Abstract

The metal oxide semiconductor field effect transistor (MOSFET) is one of the foremost semiconductor devices, for its importance in logic circuits that delivers powerful and accessible computers. The efficiency and cost of microchips go hand in hand with the decreasing dimension of the devices; however, this impressive downscaling resulted in a no longer reliability of Silicon, key material in semiconductor industry, because of quantum effects such as tunnelling of electrons through the SiO_2 gate. As a result, new materials and devices are researched intensively.
In this work, the focus is the characterisation of a particular high-κ dielectric/new generation semiconductor gate stack: hexagonal epitaxial $GdScO_3$ on GaN grown on Si(111) wafers, already considered ground-breaking for optoelectronic devices and high electron mobility transistors. The correlation between structure, electronic bands and electrical properties are investigated. X-ray diffractography evidenced that the oxide layer is hexagonal, epitaxial relaxed with respect to Wurtzite GaN. The relative permittivity emerged by capacitance-voltage measurements fulfils the requirements of high-κ dielectrics. The staggered band alignment between GaN and $GdScO_3$, measured with X-ray photoelectron spectroscopy, finds evidence in a asymmetric dielectric breakdown strength in current-voltage measurements.
Closely related systems are studied along with the aforementioned crystalline $GdScO_3$/GaN: amorphous $GdScO_3$ and epitaxial $LaLuO_3$ on the edge of dielectrics, $Al_{0.5}Ga_{0.5}N$ and GaN grown on sapphire wafers on the edge of semiconductors. All the systems presented the staggered band alignment. The strong influence of growth defects on the gate performances are evident and discussed. Thanks to the evaluation of the behaviour of different systems, the possible sources of staggered band alignment are hypothesised. In the end, an outline to further research and imaginable applications of the systems are depicted.

Estratto

I MOSFET *(metal oxide semiconductor field effect transistors)* costituiscono alcuni fra i più importanti componenti per l'elettronica, a causa del ruolo fondamentale che ricoprono nei circuiti integrati ad uso elettronico ed informatico. L'efficienza e i costi dei MOSFET vanno di pari passo con la riduzione delle dimensioni dei componenti; tuttavia, questa miniaturizzazione spinta è recentemente sfociata in un drastico deterioramento dell'affidabilità e delle presazioni dei dispositivi, a causa della non compatibilità del Silicio e del suo ossido SiO_2 - materiali chiave per decenni nell'industria elettronica - approcciando la scala nanometrica, per via del sorgere di effetti di confinamento quantistico come il tunnelling di elettroni attraverso l'ossido nella regione del *gate*. Di conseguenza, lo studio di nuovi materiali per applicazioni elettroniche è estremamente sviluppato e di notevole importanza per l'evoluzione dei circuiti integrati. In questo lavoro di tesi, lo scopo è la caratterizzazione dell'accostamento di un ossido ad alta permittività con un semiconduttore ad alte prestazioni: $GdScO_3$ cristallino, ottenuto per crescita epitassiale, su GaN, già considerato un materiale rivoluzionario nel campo dell'optoelettronica e nei transistor ad alta mobilità elettronica, a sua volta cresciuto per *molecular beam epitaxy* (MBE) su wafer di Silicio (111). La ricerca si focalizza sulla correlazione fra struttura cristallografica, bande elettroniche e proprietà elettriche di GSO-GaN/Si(111), analizzate facendo uso di *MOS capacitors* che rappresentano macroscopicamente il comportamento del *gate* nei MOSFET.
L'elaborato è strutturato in cinque capitoli, di cui un'introduzione ed una conclusione, ed un'appendice. Nell'**Introduzione** sono illustrati i contenuti dei capitoli. Nel **Capitolo 1** è fornito un background teorico per inquadrare lo scopo della ricerca, seguito da una dettagliata lista di obiettivi; sono esposte le caratteristiche di ossidi ad alta permittività e di semiconduttori ad alta mobilità, con particolare attenzione verso gli ossidi di terre rare e la classe dei *III-V nitrides semiconductors*; il funzionamento del *MOS capacitor* è descritto. Nel **Capitolo 2**, sono forniti gli elementi teorici delle tecniche analitiche impiegate, e per l'interpretazione dei risultati. Nel **Capitolo 3** sono elencati i dettagli dei sistemi in analisi e dei parametri utilizzati sperimentalmente nelle misure, mentre l'**Appendice A** fornisce i dettagli sulla preparazione dei campioni eseguita esternamente, alleggerendo la discussione dei risultati nel **Capitolo 4**. In quest'ultimo sono esposti e progressivamente discussi i risultati ottenuti dalle diverse analisi. Analisi di diffrattografia a raggi X (XRD) mostrano la cristallinità del layer di ossido e l'effettivo ottenimento della crescita epitassiale di GSO su GaN (Wurtzite, esagonale), con un rilassamento dei parametri reticolari rispetto al semiconduttore causato dal maggior raggio ionico delle specie costituenti l'ossido. La costante dielettrica derivata da misure di capacità in risposta ad un potenziale applicato ai terminali del *MOS capacitor* presenta valori sufficienti da giustificare l'annoveramento di GSO fra gli ossidi ad alto κ. Spettroscopia XPS è usata per determinare la natura dei legami nei layer e descrivere le bande elettroniche all'interfaccia fra ossido e semiconduttore. Questo risulta non centrato (*staggered*), dove la banda di conduzione del GaN è energeticamente più elevata della banda di conduzione del GSO, contrariamente

a quanto verificato generalmente nei *gate*. Ciò trova conferma nell'asimmetria della risposta elettrica (corrente) alla stimolazione dei campioni con potenziali di polarità opposta. Sistemi strettamente correlati a GSO-GaN/Si(111) sono studiati in parallelo: dal versante degli ossidi è stato fatto uso di GSO amorfo e LLO ($LuLaO_3$), mentre $Al_{0.5}Ga_{0.5}N$ e GaN depositato su wafer di zaffiro sono stati adottati come semiconduttori alternativi. Tutti i sistemi hanno presentato lo stesso disallineamento delle bande elettroniche. Grazie all'analisi di diversi sistemi che differiscono di caratteristiche di base, è possibile ipotizzare la sorgente di disallineamento delle bande; inoltre, la forte influenza dei difetti di crescita nel semiconduttore sull'ossido epitassiale, con conseguenti effetti sulle prestazioni del sistema, è evidente da analisi di microscopia e discussa alla luce dei comportamenti rilevati nelle precedenti caratterizzazioni. In **Conclusione** sono ripresi i risultati ottenuti correlando le diverse analisi, con un elenco degli interessanti spunti per la ricerca futura.

Il lavoro di tesi sperimentale è stato svolto presso il Technion, Israel Institute of Technology.

Contents

Abstract iii

Estratto v

Contents viii

Introduction 1

1 Properties and applications of Rare Earth Oxides and III-V Nitride semiconductors 5

1.1 Electronic and Optoelectronic devices: introduction and classification . . . 5

1.1.1 Optoelectronic devices . . . 6

1.1.2 Power Electronic devices . . . 7

1.2 Integrated circuits: challenges . . . 7

1.3 High-κ dielectrics . . . 9

1.3.1 Rare Earth Oxides . . . 13

1.4 High Electron Mobility Semiconductors . . . 15

1.4.1 III-V Nitrides . . . 16

Applications of III-V Nitrides . . . 18

1.5 Electrical properties of the Metal Oxide Semiconductor Capacitor . 19

Goal of the research 29

2 Experimental techniques 31

2.1 X-ray Diffractography (XRD) . . . 31

2.1.1 Theory of diffraction . . . 31

2.1.2 XRD experimental apparatus . . . 33

2.1.3 X-ray diffractometry for the characterisation of crystalline films . . . 37

Symmetric scattering: XRD θ-2θ . . . 37

Asymmetric scattering: XRD ω-2θ . . . 38

In-plane XRD . . . 38

Pole Figures . . . 38

Rocking Curves . . . 39

X-ray Reflectivity (XRR) . . . 39

2.2 X-ray photoelectron spectroscopy (XPS) . . . 40

2.2.1 Theory of photoelectric emission for XPS analysis . . . 41

2.2.2 Experimental apparatus . . . 44

2.2.3 XPS spectral interpretation . . . 47

2.2.4 Determination of Band Alignment . . . 51

2.3 Two-point probe electrical characterisation method . . . 52

2.3.1 Current-Voltage (IV) measurements of MOS capacitors . . . 53

2.3.2 Capacitance-Voltage (CV) measurements of MOS capacitors 54

Oxide relative permittivity evaluation 55

3 Materials and Methods **57**
3.1 Metal/Oxide/Semiconductor systems: sample stacks 57
3.2 Structural characterisation of the systems 59
3.2.1 X-ray diffractography characterisation of semiconductors and epitaxial oxides 59
3.2.2 Transmission electron microscopy imaging of oxide-semiconductor interface 61
3.3 X-ray photoelectron spectroscopy and band alignment on thin oxide film samples 62
3.4 Electrical measurements 62
3.4.1 Current-Voltage measurements 62
3.4.2 Capacitance-Voltage measurements 63

4 Results and Discussion **65**
4.1 Crystal structure of the oxides on III-V nitrides studied by XRD . . 65
4.1.1 Crystalline structure of epitaxial rare earth oxides 65
4.1.2 Hexagonal cell parameters 66
4.1.3 Quality of the substrates 71
4.1.4 Oxide layer thickness 72
4.2 Bonds and Band Alignment of the oxide/III-V nitride systems from XPS investigation 73
4.2.1 Elemental and bond analysis 73
4.2.2 Oxide energy gap measurement 80
4.2.3 Valence band offset 80
4.2.4 Staggered Band Alignment 80
4.3 Electrical behaviour of Al/oxide/III-V nitride systems 85
4.3.1 Current-Voltage curves 85
4.3.2 Capacitance-Voltage curves and determination of relative permittivity κ 89
4.4 TEM imaging of the oxide/III-V nitride interface 90
4.4.1 Nature and influence of interface layers on asymmetry . . . 90
4.4.2 Influence of dislocations and pinholes on performances . . . 92

Conclusion **97**

A Samples preparation **101**

Bibliography **103**

Acknowledgements **107**

List of Figures

1.1 Semiconductor devices examples 6
1.2 Moore's law 8
1.3 High-κ dielectrics effect 9
1.4 Band Gap and Relative Permittivity of high-κ oxides 10
1.5 Gate-first and gate-last fabrication 11
1.6 MOSFET materials evolution 12
1.7 Rare Earths 13
1.8 Binary Rare Earth Oxides polymorphism 14
1.9 Channel materials 15
1.10 GaN-based blue LEDs: 2014 Nobel Prize 16
1.11 III-V Nitrides Bandgap and Lattice constant 17
1.12 Ga-face and N-face of Wurtzite GaN 18
1.13 MOS capacitors 20
1.14 MOS capacitor band diagram 22
1.15 Band diagrams for accumulation, depletion and inversion 23
1.16 Small-signal alternation 24
1.17 C-V of MOS capacitors 27
1.18 Series resistance equivalent circuit 27

2.1 3D Bravais lattices 31
2.2 Miller indexes 33
2.3 d-spacings in XRD 33
2.4 XRD apparatus angles 34
2.5 Sample rotation angles 34
2.6 XRD dummy scheme 35
2.7 Vacuum tube for X-ray generation 36
2.8 Pole figure construction 38
2.9 XRR fringes 40
2.10 Levels alignment of sample and instrument (XPS) 43
2.11 Escape depth and inelastic scattering 43
2.12 XPS apparatus 46
2.13 Hemispheric electron analyser 48
2.14 XPS peak parameters 49
2.15 Chemical shift 49
2.16 Band alignment 51
2.17 Probe station 53

3.1 Thin film and thick film samples stack 58
3.2 Systems under analysis 58
3.3 MOS capacitor cross section 59
3.4 Working XRD θ-2θ photo 60
3.5 Working XRD Pole Figures photo 61
3.6 I-V and C-V two-point contacts photo 63

4.1 XRD Pole Figures of LLO-GaN/Si(111) 66
4.2 XRD θ-2θ of crystalline, amorphous GSO-GaN/Si(111) and bare GaN/Si(111) 67
4.3 XRD θ-2θ LLO-GaN/Si(111) 68
4.4 XRD θ-2θ GSO-AlGaN/Si(111) 68
4.5 XRD θ-2θ GSO-GaN/Sapphire 69
4.6 XRD in-plane GSO-GaN/Si(111) 70
4.7 XRD tilted θ-2θ GSO-GaN/Si(111), LLO-GaN/Si(111) 70
4.8 XRD Rocking Curves GSO-GaN/Si(111) 72
4.9 XRR spectrum sample 72
4.10 XPS Ga*3p* crystalline GSO-GaN/Si(111) and bare GaN/Si(111) . . . 74
4.11 XPS Ga*3p* amorphous, crystalline GSO-GaN and GSO-AlGaN . . . 75
4.12 XPS N*1s* GSO-GaN/Si(111), LLO-GaN/Si(111) 76
4.13 XPS N*1s* amorphous, crystalline GSO-GaN and GSO-AlGaN 77
4.14 XPS O*1s* peak in amorphous, crystalline GSO-GaN and GSO-AlGaN 78
4.15 XPS O*1s* peak of GSO-GaN/Si(111) and LLO-GaN/Si(111) 78
4.16 XPS of GSO-GaN/Sapphire 79
4.17 XPS E_{gap} of the oxide evaluation 81
4.18 XPS valence band offset evaluation 82
4.19 Band alignment: amorphous and crystalline GSO-GaN 83
4.20 Band alignment: crystalline systems under analysis 84
4.21 Asymmetric I-V of crystalline GSO-GaN/Si(111) 86
4.22 I-V crystalline and amorphous GSO-GaN/Si(111) 87
4.23 I-V crystalline GSO-GaN/Si(111) and GSO-GaN/Sapphire 88
4.24 I-V crystalline GSO-AlGaN/Si(111) 88
4.25 C-V multifrequency sample 89
4.26 TEM, GSO-GaN interface layer in crystalline GSO-GaN/Si(111) . . 91
4.27 TEM, GSO-GaN interface layer in crystalline GSO-GaN/Sapphire . 91
4.28 TEM, GSO-GaN interface layer in amorphous GSO-GaN/Si(111) . 93
4.29 TEM, pinholes in GSO-AlGaN/Si(111) 94
4.30 Optical microscopy, pinholes density comparison 96

List of Tables

1.1 Electronic properties of GaN and Si 18

2.1 Bravais lattices 32

4.1 Hexagonal cell parameters 71
4.2 XRR layer thicknesses 73
4.3 XPS oxides E_{gap} 81
4.4 XPS valence band offsets 82
4.5 Band alignments 84
4.6 GSO and LLO relative permittivities 90

Introduction

Semiconductor devices are all around us. They define the society we live in, the knowledge we access, the objects we use. Among the colourful landscape of these modern tools, transistors play a fundamental role as switches in integrated circuits for electronic applications: the possibility to miniaturise and integrate impressive numbers of devices per chip not only goes hand in hand with cost reduction and better energetic efficiency of memories and microprocessors, but also with the rapidity and complexity of operations, achieving objectives unthinkable of until a few decades ago. Production process optimisation and device design have allowed the transistors downscaling at the aggressive rate of Moore's law, up to reaching billions of logic nodes per chip and feature sizes effectively used in devices of tens of nanometers.
Materials play a fundamental role in the electronic industry development. Historically, complementary metal oxide semiconductors (CMOS) field effect transistors (FETs) are based on Silicon and its outstanding oxide, SiO_2, the latter used in the gate region of the MOSFET to induce the electric field in the channel, that allows or blocks the flow of electrons from source and drain. Nevertheless, getting closer and closer to the nano-world, Silicon and SiO_2 present strong limitations related to quantum confinement effects, such as tunnelling of electrons through the overly-thinned dielectric layer, that hinder strongly the efficiency and reliability of transistors. The importance of materials choice on the overall performance of the device is therefore emerging. Several approaches have been formulated to overcome the problem and continue with the constant empowering of integrated circuits: materials-wise, one of the approaches consists of the substitution of SiO_2 with higher relative permittivity gate dielectrics, increasing the oxide thickness and lowering therefore the leakages. Another approach is to substitute Silicon making use of higher mobility or breakdown resistance semiconductors, such as III-V Arsenides or Nitrides, to improve the channel performances.

Understanding how the materials involved eventually affect the overall microchip performance is therefore the crucial aspect of research in the field. In this work, the focus is the correlation between the structure, the electronic band alignment and the electrical behaviour of high performing materials for the MOSFET gate region. The systems under analysis are ternary Rare Earth Oxides/III-V Nitride semiconductors, namely crystalline $GdScO_3$ and GaN deposited on Si(111) wafers, as well as crystalline $LaLuO_3$, amorphous $GdScO_3$, $Al_{0.5}Ga_{0.5}N$ and Sapphire substrates. The experimental characterisation is performed by: X-ray diffraction methods, to investigate the crystalline structure and quality of the rare earth oxides grown on the semiconductors; X-ray photoelectron spectroscopy, to evaluate the chemical bonds and the band alignment of oxide and semiconductor; electrical current-voltage and capacitance-voltage two-point probe measurements are used to assess the electric behaviour of the MOS gate stack. Transmission electron microscopy is used to check the GSO-GaN and GSO-AlGaN interface.

All the experimental work has been performed in the Technion, Israel Institute of Technology, Haifa.

In Chapter 1, an overview about the potentialities of semiconductor devices is made, alongside the issues in obtaining higher performance and smaller size integrated circuits from complementary metal oxide semiconductor (CMOS) field effect transistors (FET). The electronic materials role in recent research is exposed by treating the literature background on two possible approaches to improvement that involve materials replacement in the gate stack: high-κ dielectrics instead of SiO_2 and high-mobility semiconductors instead of Si. The properties of Rare Earth Oxides and III-V Nitride semiconductors, pivotal in this work, are delineated. Later in the chapter the basics of MOS capacitor working are exposed, and how the informations on gate stacks can be deduced from macroscopic capacitors. Finally, the goal of the research is extensively outlined.

In Chapter 2, the theoretical basis of the techniques personally employed is provided. X-ray diffractography (XRD) of single crystalline materials is mainly used to investigate the structure, epitaxy and quality of the crystalline film, therefore the principle of the technique is exposed along with the experimental setup and spectral interpretation; X-ray reflectivity (XRR) technique is also outlined. Basics of X-ray photoelectron spectroscopy (XPS) working principle, experimental apparatus are provided to understand the data acquisition, while spectral analysis is explained in order to understand the discussion of the results in chapter 4. In the end, the basic experimental features for current and capacitance testing with an applied bias are exposed, in light of the MOS capacitor working theory exposed in Chapter 1, and the methods to extract breakdown field and relative permittivity of the dielectric are explained.

In Chapter 3, the gate stacks under analysis in the work are described: crystalline *GSO-GaN/Si(111)* is the central system, where *GSO* is the $GdScO_3$ and */Si(111)* refers to the fact that GaN is grown on a Silicon substrate wafer. Other systems include the use of an amorphous GSO, crystalline LLO ($LaLuO_3$), $Al_{0.5}Ga_{0.5}N$ semiconductor and the GSO-GaN system grown on a Sapphire wafer. Details on the experimental procedures and the information derived from each analysis are provided, as a preamble to the results exposed in chapter 4.

In Chapter 4, results of the experimental analyses are shown in the following order: the structural characteristics, the band alignment, the electrical behaviour and the interface nature. Results are progressively discussed in light of the technique itself and of cross-references with the information acquired from other analyses. In the structural results, the epitaxy of GSO and LLO crystalline layers is evaluated with pole figures; symmetric and tilted-sample symmetric scattering determine the lattice parameters of the hexagonal layers, along with the amorphous nature of the oxide layer in amorphous GSO-GaN grown on Si(111) wafers; the crystal quality is evaluated with rocking curve measurements, comparing Si(111) and Sapphire substrates; the oxide layer thickness is evaluated with X-ray reflectivity. XPS spectral analysis confirmed the chemical bonds nature of each III-V nitride and rare earth oxide layer, along with the evidence of hygroscopicity of the oxide layers; energy gap of the oxides evaluated from electron energy loss tails made evident that the amorphous and crystalline GSO have the same band gap, while LLO is characterised by larger band gap than GSO; valence band offset and energy gap provide a very well defined picture of staggered band alignment of all the systems under analysis, where the conduction band of the semiconductor is higher

in energy than the conduction band of the oxide. This is clearly reflected in the asymmetric response of the current to a negative or positive gate bias. The relative permittivity deduced by capacitance-voltage measurements classifies both GSO and LLO as high-κ dielectrics, with higher κ for LLO with respect to GSO. In the end, transmission electron microscopy imaging of the oxide-semiconductor interfaces are shown: from the situation captured, the evidence of a Scandium-rich interface layer is crucial to speculate on the staggered band alignment of the systems. The TEM imaging also justifies the electrical behaviour of GSO-AlGaN systems, as function of the defects density and extension.

In the Conclusions, the results obtained in the thesis work are summarised. Special importance is given to: the evidence of staggered band alignment reflection on the electric behaviour of the gate stack; the role of the so-called Sc-rich interface layer in the unexpected staggered band alignment; the impact of defects, function of the structural parameters and MOS capacitors stack production, on the electrical performances. In light of these considerations, hints for further work are outlined.

In **Appendix A**, the details on samples preparation are provided: molecular beam epitaxy of the nitrides on the substrate wafers, cleaning procedures prior to the oxide growth, pulsed laser deposition of the oxides and reactive ion etching of the oxide layer to produce the substrate (body) contacts.

Chapter 1

Properties and applications of Rare Earth Oxides and III-V Nitride semiconductors

This chapter introduces the challenges that the semiconductor industry faces for the improvement of very large scale integration devices: in particular, the role of high-κ dielectrics and new generation semiconductors in metal oxide semiconductor field effect transistors is highlighted. The various semiconductor devices are briefly described, with a focus on major issues in transistors downscaling. High-κ dielectrics and rare earth oxides are introduced to substitute the SiO_2 gate region; high mobility semiconductors and III-V nitrides are introduced to substitute the channel material in a post-SiO_2 gate era. In the end, the working principle of the MOS capacitor used for macroscopic simulation of the gate stack is shown, and the goal of this research on ternary Rare Earth Oxides/III-V Nitride semiconductor MOS capacitors is defined.

1.1 Electronic and Optoelectronic devices: introduction and classification

Semiconductor devices are all around us. They define the society we live in, the knowledge we access, the objects we use. They send us to Mars, they allow our bridges to be safe and beautiful, they make us share videos of kittens.
Since the invention of the bipolar transistor in 1947 the field has grown exponentially, thanks to physical properties of semiconductor materials, *pn*-junctions, coupling with dielectrics, and numerous breakthroughs in device concepts and optimisations.[1] Hence, the variety of semiconductor devices is vast: bipolar and field effect transistors are capable of providing current and voltage amplification, as well as to work as switches in logic nodes; therefore they allow the production of integrated circuits for signal transmission, amplifiers, sensors and computer microprocessors. The examples in figure 1.1 are just some among the possible functionalities. After a first use of Germanium, the combination of semiconductor properties, great native oxide and optimised processing imposed Silicon to the world wide semiconductor industry, rapidly allowing the diffusion of computational power through the most diverse environments and applications.[1]
Semiconductors are not only limited to Silicon. An important feature of the direct band gap semiconductors is the interaction with light by absorption and conversion of photons into current, or viceversa the emission of light from the

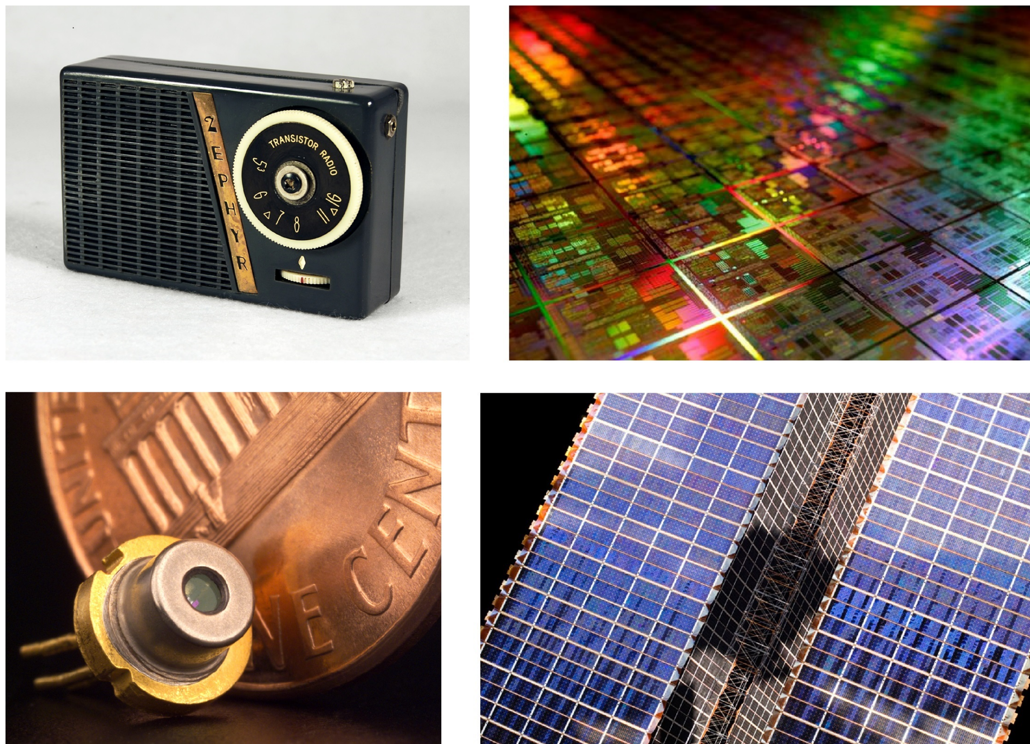

FIGURE 1.1: examples of electronic devices. From top left to bottom right: a transistor radio, microchips on a wafer, a semiconductor laser diode, solar panels of the ISS.

spontaneous or stimulated radiative recombination of electrically excited charge carriers.
This, and the continuous objective of improving semiconductor devices for the important tools they represent in our lives, is the driving force of the materials, devices and processes research carried on extensively until now, and on.

1.1.1 Optoelectronic devices

A whole class of semiconductor devices is dedicated to the interaction of semiconductors with photons around the visible range, and takes the name of *optoelectronic devices*. The main optoelectronic devices are:

- **light emitting diodes (LEDs)**: mono- or poly-chromatic light sources consisting of a diode in a resin lens. Light is emitted by spontaneous radiative relaxation transitions of electrons, brought in the conduction band by the application of a bias.
- **laser diodes**: monochromatic, bright and coherent light sources exploiting stimulated emission of photons in analogous relaxation transitions; the resonator consists of the semiconductor layer (photoemitter) that works as a waveguide.
- **photodiodes**: detectors of incident photons of energy equal to the bandgap of the semiconductor. Charge migration to different electrodes occurs after

the photogeneration of an electron-hole pair in the diode; consequently, a current proportional to the incident photons is produced and measured.

- **photovoltaic cells**: analogous photogeneration of an electron-hole pair by incident photons of light in the NIR-visible-UV range, depending on the semiconductors used and their stack (availability of different bandgaps induces the absorption of a wider range of photon energies). The electron-hole pair generates a voltage in an open circuit, that can be used by an external load to allow the recombination of the charge carriers afterwards.[2]

1.1.2 Power Electronic devices

The main *power electronic devices* can be grouped in the following classes:

- Bipolar devices:
  - ***pn*-junction diode**;
  - **bipolar transistor**;
  - **thyristor**;
- Unipolar devices:
  - **junction field effect transistor (JFET)**;
  - **metal insulator semiconductor (MIS) diode**;
  - **microwave devices** and **microwave tunnel devices**;
  - **metal oxide semiconductor field effect transistor (MOSFET)**.

Many of the bipolar devices and the microwave devices are used for their rectifying properties, for example for signal manipulation and transmission, and their basics are beyond the scope of this work.
The basic device for very large scale integration in logic circuits and random access memories is the MOSFET, and its further level integration constituted by the complementary metal oxide semiconductor (CMOS) field effect transistor (FET), that couples two different channel MOSFETs in the same region. Other devices undergoing very large scale integration are bipolar transistors for the production of random access memories.[1, 3]

1.2 Integrated circuits: challenges

The paramount importance of semiconductors is the production of complementary metal oxide semiconductor (CMOS) field effect transistors (FETs) to obtain integrated circuits for very large scale integration (VLSI) of devices onto microchips. The reduction of the dimension of the logic nodes, having the direct consequence of the constant increase of number of components per chip, has gone hand-in-hand with the improvement of the performance, power consumption reduction and decrease of the cost of the device along the last forty years.[4] The downscaling of the logic nodes follows a linear trend in time well renowned as "Moore's Law", expressed by number of the components per chip that doubles roughly every two years (figure 1.2a). The evolution of the feature size reduction was achieved by a

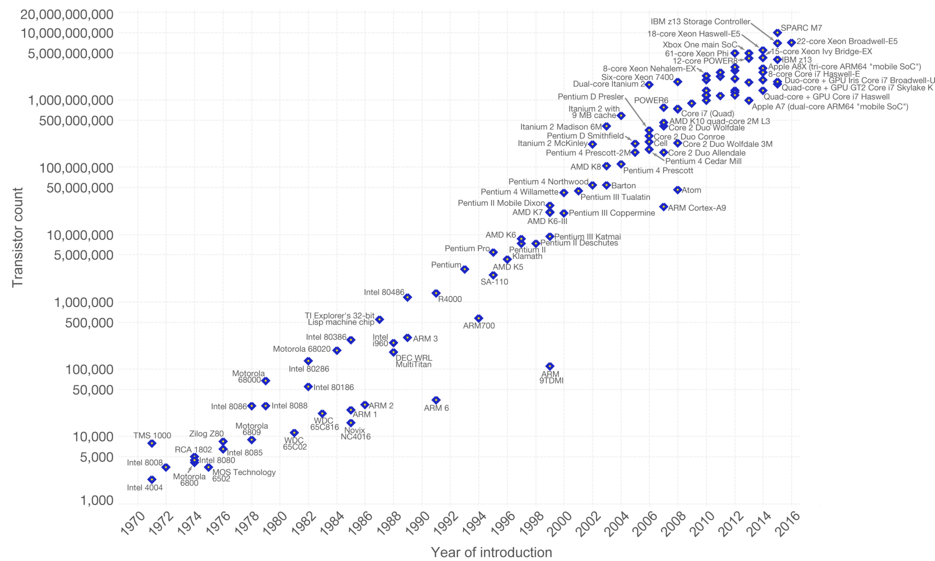

(A) Moore's law predicts the doubling of the number of the devices on a single chip every roughly two years since 1965.

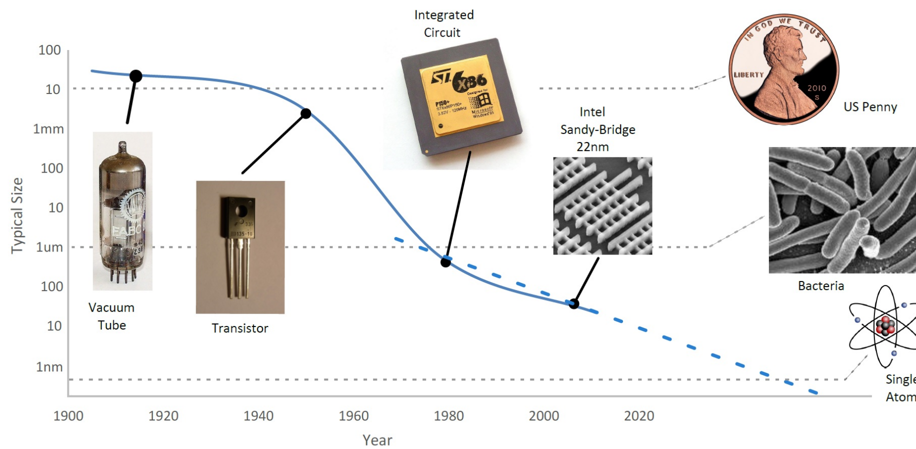

(B) nodes feature size in time.

FIGURE 1.2: evolution of logic nodes integration by (a) number of transistors per chip and (b) nodes feature size.

continuous optimisation of the microfabrication processes, while only recently a revolution in the fundamental design of the devices and in the materials employed took place (figure 1.2b). Mapping of this evolutionary path in the semiconductor industry and guidelines for future research are recorded by the International Technology Roadmap for Semiconductors.[5, 6]

Further and further downscaling, at Moore's law pace since 1965, resulted in an eventual reach of feature sizes where quantum effects due to electrons tunnelling and confinement take place within the thinning SiO_2 gate dielectric layer. As a result, the devices are no longer scalable without a drastic reduction of performances and reliability. To keep on downscaling the devices, even deviating from Moore's law, strong efforts are nowadays put in the research of new materials and architectures for MOS field effect transistors.[4]

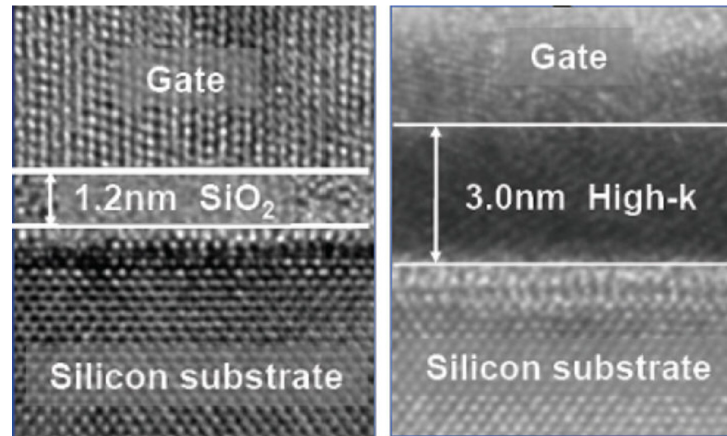

FIGURE 1.3: comparison between SiO_2 and high-κ dielectric (HfO_2) gate stacks.[7] It is possible to notice the abrupt Si-oxide interface but the interdiffusion at the oxide-gate electrode interface.

1.3 High-κ dielectrics

The scaling of MOSFETs in CMOS technology has led to the silicon dioxide layer historically used as gate dielectric to become extremely thin: as a consequence, the electrons tunnel through the oxide and the gate leakage current becomes unacceptable. To prevent this, a thicker gate oxide layer is required along with the preservation of the gate capacitance, and thus oxides with higher relative permittivity (κ) than SiO_2 (3.9), so-called high-κ dielectrics, are studied to allow CMOS transistors downscaling as well as enhancing the dielectric properties, with the goal of performances improvement of the device.[4, 7, 8] An example of thickening of the gate oxide thanks to the application of a high-κ dielectric is reported in figure 1.3.

An additional aspect of the materials selection for MOS gate region is represented by the substitution of the highly doped poly-Si gate electrode with a metallic gate, reducing greatly the depletion region thickness in the electrode and therefore the carriers density at the dielectric interface. The restricted choice of gate metals, based on the compatible workfunction with the rest of the gate stack, results in an additional constrain for the investigation over the high-κ dielectric.
In general, the implementation of dielectrics of different chemical nature on Silicon leads to physical and technological issues never presented with the use of SiO_2. The new dielectrics are required to:

1. have a κ **enough higher than SiO_2** to allow a reasonable scaling of the nodes that economically justifies the conversion of the production lines, that is usually defined with $\kappa > 12$ at least;
2. be **chemically (thermodynamically) stable with Silicon** for the presence of interfaces with the semiconductor and the poly-Si gate electrode, to avoid the formation of a SiO_2 interface layer by reaction of Si and oxygen from the foreign oxide;
3. be **kinetically stable** at high processing temperatures and during the device lifetime, for no phase transformation of the oxide and metallurgical reaction

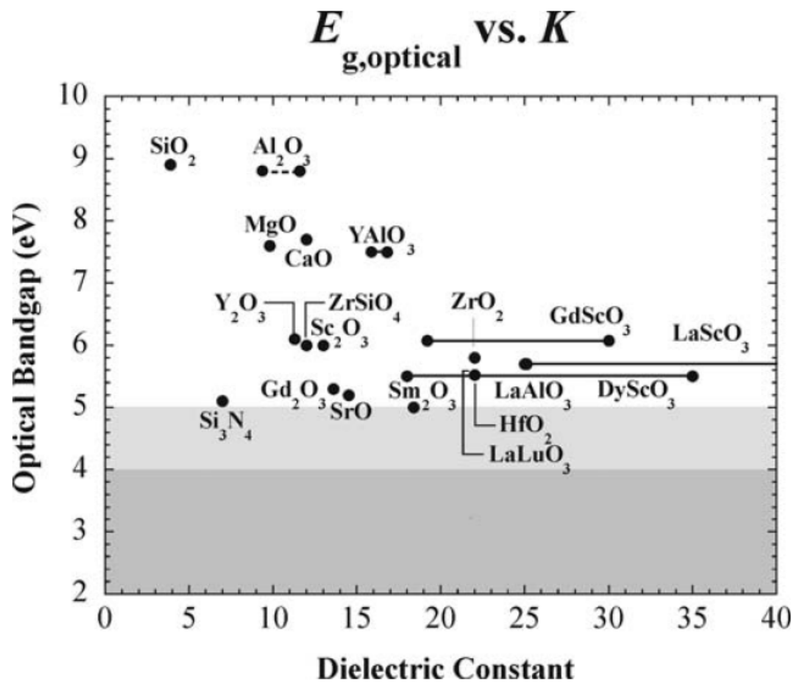

FIGURE 1.4: band gap plotted in function of the relative permittivity of SiO_2 and the main high-κ oxides.

with the gate electrode should take place with an uncontrolled alteration of the properties, and hence of the response of the device;

4. produce a **minimal density of electrically active defects** and dislocations at the interface;
5. have sufficiently **high band offsets** with respect to Silicon, in order to avoid carriers injection from the gate.

Condition 1) and 5) are in general conflictual, because an increase of relative permittivity is usually associated with a decrease of the band gap, and hence a reduction of the band offsets with respect to the semiconductor.
First studies lead to Hafnium oxide **HfO_2** to be preferred as high-κ dielectric on Si over other candidates since the 90s; nonetheless, HfO_2 still shows some crucial problems of stability of the amorphous phase and high oxygen diffusivity, that leads to oxygen vacancies states and possibility of carriers injection through the oxide. Alternative dielectrics in crystalline and amorphous phases are largely studied to overcome the HfO_2 drawbacks.

The major exponents of the high-κ oxides are, aside HfO_2 and Hf-based dielectrics, **Al_2O_3, ZrO_2** and **rare earth oxides**, with dielectric constants spanning from 8-9 up to values of 35 and higher. Each of the alternative high-κ dielectrics show technical drawbacks, such as reactivity with Si for ZrO_2 to form $ZrSi_2$, high density of defect generated with Al_2O_3, hygroscopicity of binary rare earth oxides; the issues can be partially overcome by studying ternary oxides, like rare earth silicates, aluminates and zirconates, and pure rare earth ternary oxides.[7, 9–11] Figure 1.4 shows the E_{gap} and κ of the most important high-κ oxides.
The relative permittivity is highly influenced by the crystalline structure of the

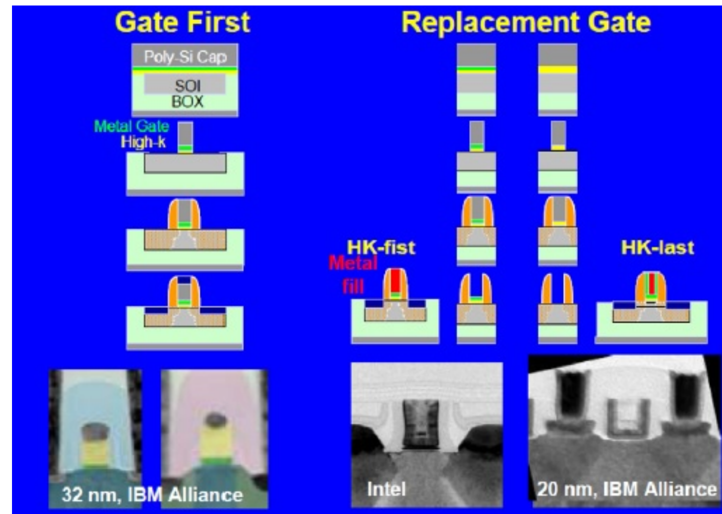

FIGURE 1.5: gate-first and gate-last approach to gate stack deposition.[7]

dielectric. In principle, crystalline phases are characterised by higher κ, although this is usually not verified practically. In fact, the density of defects generated by crystalline reorganization and mismatch-derived dislocations lower consistently the quality of dielectric properties of the crystalline materials; therefore, amorphous oxides are generally preferred over crystalline. The variety of crystalline arrangements and the tunability of lattice parameters is one of the advantages of ternary rare earth oxides, which will be better discussed in section 1.3.1.
A way to compare high-κ dielectrics is to define the capacitance equivalent thickness (CET), defined as the thickness of SiO_2 necessary to provide the dielectric capacitance shown by the high-κ dielectric in the gate stack. High-κ dielectrics with subnanometric CET were successfully achieved.[11, 12]

The choice of the high-κ dielectric for gate applications is largely influenced by technological aspects related to the device fabrication. The gate dielectric and metal need to be sequentially deposited, and the device is fabricated by lithography, etching and doping of source and drain; further on, the interconnections layers are produced, but in less critical conditions with respect to the previous steps.
Si/SiO_2/poly-Si process flow consists in the thermal growth of SiO_2 from Si wafer, the deposition of poly-Si gate electrode on SiO_2, the lithography and etching step to isolate the gates, perform source and drain doping implantation and finally anneal at $\approx$ 1000°C to promote diffusion of the doping species. The gate-first approach for the production of Si/high-κ/Metal MOSFET is similar to the process flow of the Si/SiO_2/poly-Si gate stack, often with the addition of an intermediate layer between the gate dielectric and the metal in order to tune the gate electrode workfunction. Therefore in the gate-first process flow, the dielectric-metal interface is subjected to an intense annealing at $\approx$ 1000°C, too high for avoiding metallurgical reactions in many high-κ dielectrics.
Gate-last process flow overcomes the problem of the high-T exposition of the oxide-metal interface during the annealing by two approaches:

1. depositing the gate electrode after the annealing;
2. depositing the gate dielectric and the gate electrode after the annealing.

In order to do so, a poly-Si dummy gate electrode (for the first approach) or

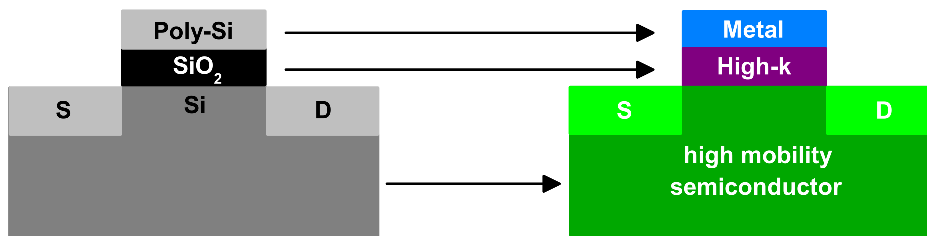

FIGURE 1.6: evolution of the MOSFET based on the choice of materials for the performances improvement and the nodes downscaling.

dummy gate dielectric+electrode (for the second approach) is deposited before the gate etch, the ion implantation and the subsequent annealing. After that, chemical mechanical polishing (CMP) is used to planarise the surface, the dummy gate is etched and the trench is filled with the gate metal (or first the dielectric and then the gate metal in the second approach). This leads to a maximum temperature to which the oxide-metal interface is subjected of around 500°C, that induces much less unwanted reactions than in the gate-first process.[7] The process is illustrated in figure 1.5. The main techniques to deposit gate dielectrics are physical vapour deposition (PVD) and chemical vapour deposition (CVD). Particular relevance is found for:

- Sputtering, that allows the deposition of stoichiometric oxides, but the conformal coverage of the trenches in gate-last approach is not excellent;
- Deposition of metal by e-beam evaporation, with subsequent UV or O_3 oxidation, that can raise problems in stoichiometry and homogeneity;
- Pulsed laser deposition (PLD), especially indicate to grow amorphous and epitaxial thin films maintaining the stoichiometry of the target, either ceramic or metallic in reactive PLD, ablated by the laser;
- Atomic layer deposition (ALD), very slow and requiring costly oxide-specific precursors, but allows superconformal coverage of the trench in gate-last approach;
- Molecular beam epitaxy (MBE), presenting the same advantages and drawbacks of ALD;
- Metallorganic chemical vapour deposition (MOCVD), which is typically used in microelectronics processes, but that exploits oxide-specific and expensive precursors: stable forms of the metallorganic precursors are not available yet for many oxides, especially rare earth scandates.

Usually MBE and ALD are considered too slow to be feasibly applied in a industrial process, while MOCVD and sputtering can be used in a specific industrial process but the optimisation of the growth conditions or of the precursors are excessively time consuming for experimental studies on new high-κ dielectrics.[13] The rapidity of the deposition, the relatively lower cost of the technique with respect to the alternatives and the non-selective process (oxide-specific precursors are not required) make PLD the ideal deposition method for screening of possible gate dielectrics, especially on MOS capacitors where the device is not fabricated:

FIGURE 1.7: the group of rare earth oxides displayed in the periodic table.

the semiconductor surface is macroscopically planar and no conformal coverage of any trench is needed.
A crucial aspect of the high-κ dielectrics adoption and the new-found independence over SiO_2 is the **removal of the constrain of using Silicon as semiconductor**. In fact, the advantages of using the cheap, abundant, process-optimised, but utterly average-performing Silicon were counterbalanced by the possibility to thermally grow an excellent insulator such as SiO_2. With the decadence of the advantages in the use of silica and the development of foreign dielectrics to be deposited on the gate region in MOSFETs, the doors to the development of higher mobility semiconductors characterised by a poor proper oxide, like Ge and III-V semiconductors that will be extensively discussed in section 1.4, were open. The overall evolution of the MOSFET is represented in figure 1.6. Indeed the low cost, abundance, good mechanical properties and large wafer diameter (up to 450mm) that allow a very high scalability of the dyes production will still maintain Si as a key material for very large scale integration (VLSI) devices.[3, 6, 7]

1.3.1 Rare Earth Oxides

Rare earth elements include Scandium, Yttrium, Lanthanium and the Lanthanides, as shown in figure 1.7. Rare earth elements are characterised by asymmetric d and f orbitals that allow the enhancement of magnetic, electric, optical and catalytic properties of many materials.[14] In particular, the oxides of rare earth elements raised interest in the study of alternative gate dielectrics, along with Hf-based oxides, because of the high relative permittivity κ, the high band gap, the chemical compatibility with Silicon and the affinity with III-V semiconductors they showed.[4, 15–17] Special interest is kept in dielectrics of rare earth elements with stable oxidation state (+3) for their lower sensibility to electric field and temperature, that is associated to higher dielectric stability. The most diffused stable phases at room temperature encountered for binary rare earth oxides are cubic (bixbyite), hexagonal (characterisic of La_2O_3 and Nd_2O_3) and monoclinic, as shown in figure 1.8.

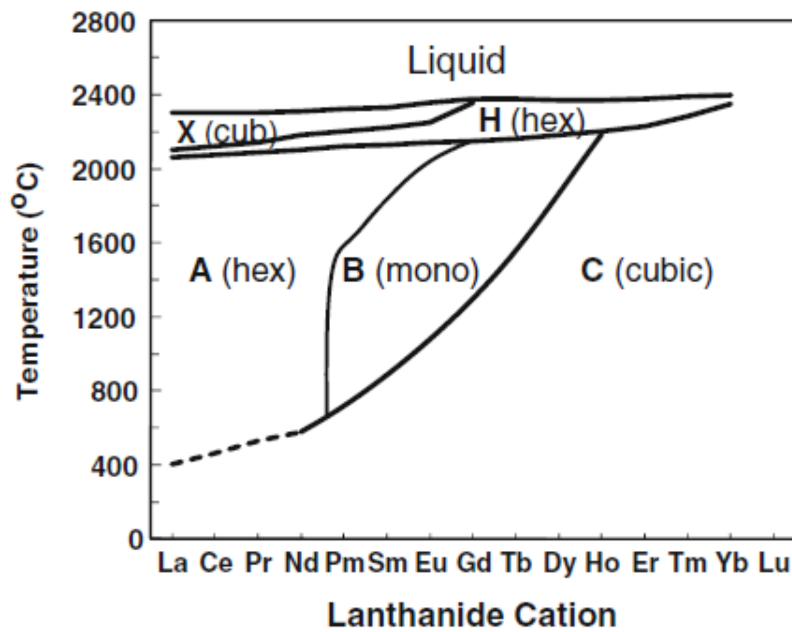

FIGURE 1.8: phase diagram of binary rare earth oxides as function of the lanthanide cation. Binary and ternary rare earth oxides crystallise in a wide variety of lattice structures.

Binary oxides tend to react to form hydroxides according to their atomic number with a consequent reduction of the relative permittivity, therefore creating a dependence of the performances on atmospheric humidity; ternary compounds instead tend to show high stability with respect to the atmospheric exposure without the use of a capping layer.[18–20]
To limit the current leakages through the oxide, research focused mostly on amorphous dielectrics, despite the material characteristics tend to evolve in reason of thermodynamically favoured recrystallisations, taking place at the interfaces or in nucleation points such as defects, during the high temperature processes of growth of the layers following the gate dielectric deposition.[21] Gate-last processes limit the high-T exposition of the gate dielectric, but the process is more costly and delicate, and one of the major advantages of rare earth oxides with respect to HfO_2 is the higher thermal stability that allows a gate-first process. Therefore, crystalline rare earth oxides are also studied: the relative permittivity of an epitaxial crystalline phase on the semiconductor is expected to be higher with respect to the corresponding amorphous dielectrics, while crystalline rearrangements for different phases grown on top of the semiconductor would result in higher leakages and therefore lower permittivity. In general, the outline of several studies on binary rare earth oxides is that the crystalline structure is more influent on the value of relative permittivity than the atomic number of the rare earth elements.[14, 22–26] For rare earth oxides on Silicon applications, an alternative to achieve even higher chemical stability is to consider rare earth silicates: the resulting κ is lower but no SiO_2 phase is formed at the interface with the semiconductor, resulting in an advantage of rare earth oxides with respect to Hf-based dielectrics especially, again, for gate-first processes of production.[9, 20]
Another approach to the improvement of rare earth oxides amorphous phase stability is to use lanthanide-rare earth ternary oxides as dielectrics, such as $LaLuO_3$,

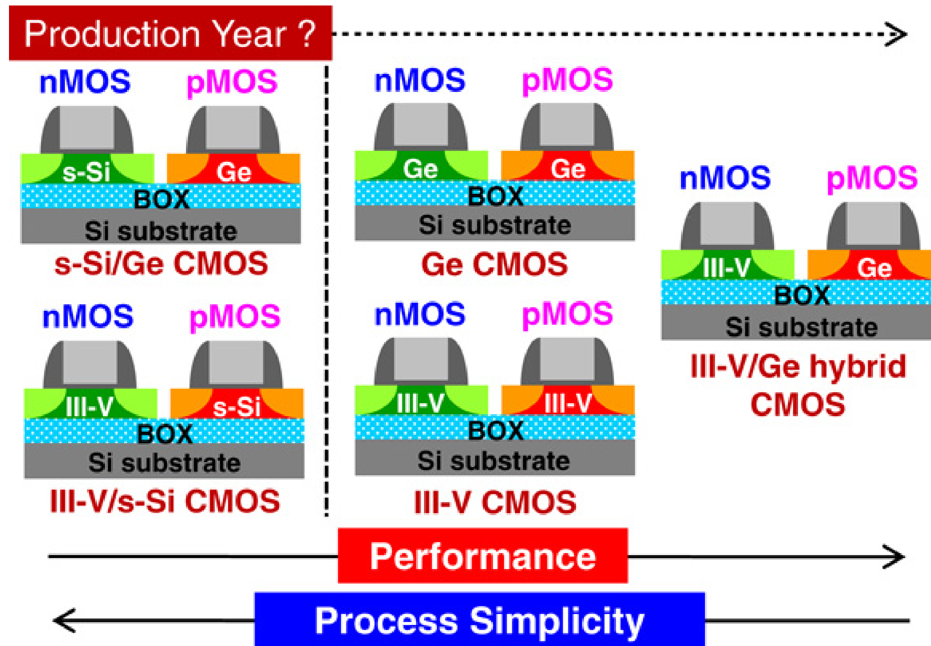

FIGURE 1.9: use of alternative channel materials in p-channel and n-channel MOSFETs.[29]

$LaGdO_3$ and $GdScO_3$. Typically, this stability is to be found in:

- higher temperature stability of the amorphous film;
- the aforementioned higher chemical inertia to the formation of the hydroxide when exposed to atmospheric humidity;
- tunability of the crystallographic structure with consequent possibility of epitaxial growth of crystalline films on either Silicon or III-V semiconductors.

The last point elects the study of ternary rare earth oxides on III-V nitride semiconductors to a particularly appalling aspect of the high-κ dielectrics investigation, for the coupling of a high-κ dielectric and a high mobility semiconductor with chemical compatibility of the materials and low density of traps at the interface.

1.4 High Electron Mobility Semiconductors

As mentioned in section 1.2, the continuous improvement of the device performances and energy consumption is cardinal for the semiconductor industry.
The use of new channel materials with improved transport properties over Silicon offer the potential for further device scaling, along with the channel architecture engineering that was initially adopted with Silicon channels as a first approach to downscaling.
For example, Silicon-On-Insulator technology was used to electrostatically control the charge in the channel by means of an oxide layer underneath Si channel; the production the thin buried oxide and ultra-thin buried oxide (BOX and UTBOX) are of interest in the Si-based and beyond-Si channel design and influence the materials testing (ref. section 1.5 and chapter 3), but are not treated extensively in this work.[27, 28]

FIGURE 1.10: Blue LEDs using GaN as photoemitter allowed the production of white LEDs and the substitution of obsolete and more dissipative light sources.

Among the new channel materials, wide interest was put in the **stress-induced** improvement of carriers mobility by the addition of the larger atomic radius Ge in the Si lattice, with significant improvement. However, the development of high-κ oxides as replacement for SiO_2 enabled the substitution of Si for the channel material integrally.
Ge shows a very high density of states in the conduction band and better holes mobility than Silicon, making possible to obtain large channel currents. However, the realisation of Ge n-type MOSFETs is still an issue, therefore hindering the fabrication of CMOS nodes; the low melting point of Ge induces thermal activation of dopants in the source and drain regions around 400-500°C, limiting the high-T applications of Ge MOSFETs.
III-V semiconductors such as **GaAs, InSb** and **InP** are particularly promising; GaAs was particularly considered to produce n-channel MOSFETs, to associate with Ge p-channel MOSFETs in CMOS integration (figure 1.9, because of the similar lattice constant they show and the poor native oxide that leads to the need of a foreign oxide deposition in all the cases. InGaAs and InGaSb are also of great interest for n-channel and p-channel MOSFETs respectively, because of their balance of high mobility, low contact resistance, interface compatibility with high-κ dielectrics and higher bandgap with respect to Silicon.[30, 31]
As mentioned in section 1.1.1, III-V semiconductors show direct band gap and are extremely important for optoelectronic devices. The possibility of integration of n-MOSFETs and optoelectronics constitutes a driving force towards the research in the III-V channel semiconductors field.

1.4.1 III-V Nitrides

III-V Nitrides such as GaN gained the attention of the research because of the high direct band gap, an interesting feature to achieve light emitters in the blue-UV range. The 2014 Nobel Prize for Physics was won by Isamu Akasaki, Hiroshi Amano and Shuji Nakamura "for the invention of efficient blue light-emitting diodes which has enabled bright and energy-saving white light sources" (figure 1.10).[32] GaN-based blue LEDs in fact allowed the production of white LEDs, that are of paramount importance in everyday life and allow a significant energy saving by replacing incandescent and fluorescent lightbulbs.

GaN is stable in a Wurtzite crystal structure that shows a direct bandgap of 3.4 eV, corresponding to a wavelength in the ultraviolet; it can also crystallise in a Zincblende structure, with lower band gaps.[33–36] Other III-cations that can

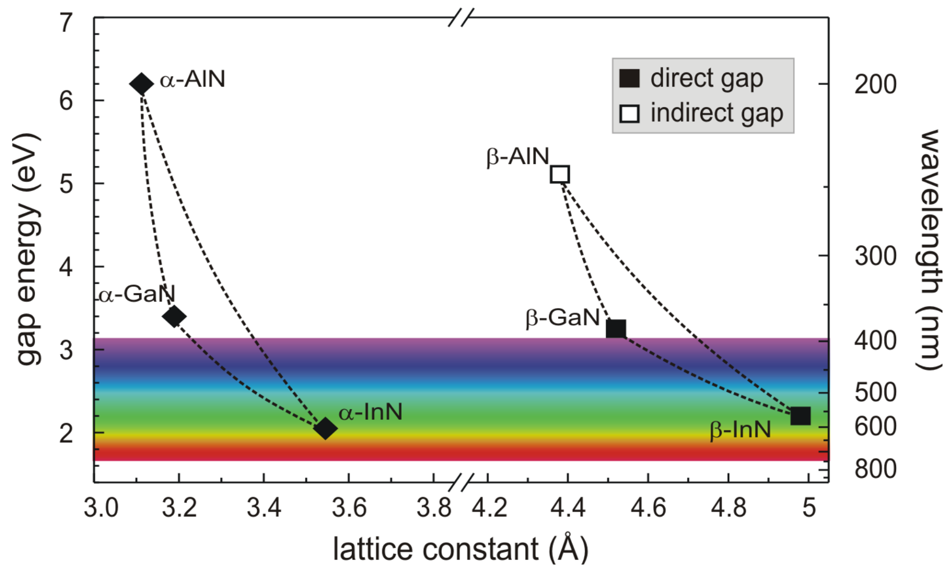

FIGURE 1.11: band gap as function of the lattice parameter, depending on the III-V Nitride semiconductor composition in Wurtzite and Zincblende crystal structures.

provide Wurtzite and Zincblende crystal structure are Al and In, making possible to obtain mixed III-V nitrides as alloys of various III elements: the band gap and lattice parameters can be tuned with the composition as shown in figure 1.11.

GaN can be grown on a substrate of sapphire Al_2O_3 or SiC, despite the difference in lattice constants, and on Si(111) and other unconventional substrates by means of strain-engineered layers to absorb the lattice mismatches.[32, 34, 37] This allows integration of GaN and derivatives in several types of circuits, as discussed in section 1.4.1. GaN can be doped with Silicon to obtain n-type and with Magnesium to obtain p-type. Unfortunately, doping interferes with the growth process so that the GaN becomes fragile, making difficult to produce a stable layer on top of a substrate: the deposition techniques will be further discussed (page 18). In general, defects in GaN crystals lead to good electron conductivity, with electrons having higher mobility than holes.[32, 34, 38] GaN show an electron mobility similar to Si, but much larger band gap and electric breakdown field extended the research on GaN to non-optoelectronic devices, for example to MOSFETs for power electronics applications; the AlGaN/GaN interface shows a higher electron mobility than pure epitaxial GaN thanks to the development of a 2D-electron gas (2DEG) at the interface: this is exploited in heterojunction field effect transistors (HFETs), better known as high electron mobility transistors (HEMTs). RF and microwave integrated circuits also benefit from the high bandgap and high mobility of the III-V nitrides for applications in power electronics.[34, 39–41] Application are better investigated in the following section.
An important feature of Wurtzite GaN is the **piezoelectricity** of the crystal, since Wurtzite cell lacks an inversion centre: this generates a dipole moment and therefore an electric response to the application of strain, base of the mechanism of the formation of the 2DEG exploited in HEMTs. Wurtzite Ga-face and N-face cells are shown in figure 1.12 with the respective dipole moments, direction of which depends on the surface-exposed ionic plane.[42] A summary of GaN electronic properties is reported in table 1.1.

GaN monocrystal is grown by molecular beam epitaxy (MBE) on top of a foreign

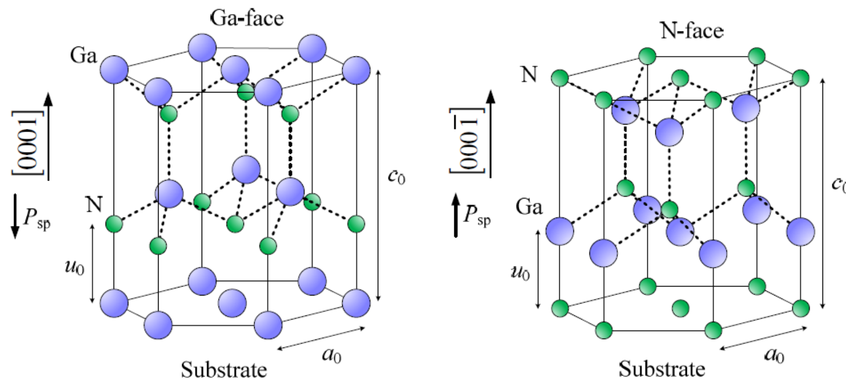

FIGURE 1.12: GaN Wurtzite cell and dipole moments generated by the lack of inversion symmetry. The direction of the dipole moment depends on the nature of the surface atomic layer.

wafer that act as structural support: pure GaN wafer growth attempts have been reportedly declared unsuccessful due to high melting temperature and decomposition pressures at melting.[43] They also tend to form dislocations and grow in pinholes from dislocations.

Applications of III-V Nitrides

Summing up the properties of GaN, AlGaN and InGaN, it is possible to list the III-V nitrides main applications according to the following features:

- semiconducting nature with a large direct bandgap;
- high electron mobility;
- high breakdown strength;
- piezoelectricity;
- hard radiation resistance;
- tunability of band gap with composition.

The consideration of III-V Nitrides nanostructures such as quantum wells, quantum wires and quantum dots, and their relative properties and applications, are

Electronic Property	Si	GaN
Band Gap [eV]	1.1 (ind.)	3.4 (dir.)
Electric breakdown field [MV/cm]	0.3	2.0
Electron mobility [cm^2/Vs]	1350	1150 (2000)
Saturation velocity [10^7]	1.0	3.0
Max estimated operation T [°C]	200	700
Baliga Figure of Merit (BFM)	1	190

TABLE 1.1: electronic properties of GaN compared to Si; the Baliga Figure of Merit evaluates the resistive losses of the semiconductor devices. Values after [34].

excluded from this work but find considerable relevance in the field of materials for electronics research, and constitute a step of further development for optoelectronic devices based on both inter-band (UV-Vis) and inter-sub-band (IR) transitions. Extensive studies in matter are found elsewhere.[34, 44–46]
As mentioned in this section at page 16, the direct band gap of III-V Nitrides makes them good emitters and absorbers of visible and UV photons because, unlike Silicon, no phonon scattering is needed to obtain the electronic transition; therefore the probability of radiative excitation and relaxation is higher because of the limitation to a single-body or two-body process and the quantum yield improves. This outstanding feature makes the III-V nitride semiconductors suitable for uses as **UV, blue or white light emitters for LEDs and laser diodes** according to the optical band gap shown in picture 1.11. The reverse process of UV-Vis light absorption can be exploited in GaN-based photovoltaic cells and photodiodes; however, III-V Nitride-based solar cells have higher costs and lower efficiency with respect to Si single crystal, while doping increases the nitrides brittleness. Nonetheless, the high band gap of III-V nitrides and the possibility to produce third generation very-high-efficiency solar cells (VHESC), exploiting tunnelling junctions and stacking different bandgap semiconductors, confirms the III-V nitrides as ground-breaking materials for the efficiency improvement of photovoltaics. The exceptional resistance to hard radiation makes III-V nitrides the key semiconductors for **solar cells** and in general **electronic devices for space environment applications**.[34, 40, 47–49]

III-V nitrides electron mobility, heat dissipation coefficient and make them a better performing replacement of Silicon in **MOSFETs**: since GaN does not develop a stable native oxide when in contact with atmospheric oxygen, high-κ dielectrics are exploited. The hexagonal structure of Wurtzite and the aforementioned wide variety of lattice structures of ternary rare earth oxides make the **metal/high-κ/III-V nitride gate stack** a possible structure to downscale the node feature size and reduce the power consumption of the integrated circuit.[50, 51]
The piezoelectricity, high mobility (2000 cm^2/Vs for Wurtzite GaN at the interface with AlGaN) and high breakdown strength of III-V nitrides is base for the choice of AlGaN/GaN stacks as channel material of **high electron mobility transistors (HEMTs)**, that find particular relevance in low resistance switches.
The high breakdown strength is an advantage for **high voltage power devices** such as RF and microwave integrated circuits: high frequency switches, and amplifiers are produced from III-V Nitrides deposited on insulating layers, such as Sapphire or SiC, the latter providing also a high heat dissipation.[41, 52]

Finally, III-V nitrides piezoelectric nature can be exploited for the actuation mechanisms in **RF-MEMS**, leading to new possibilities for GaN-based semiconductor devices integration.[53, 54]

1.5 Electrical properties of the Metal Oxide Semiconductor Capacitor

According to what exposed in the previous sections, a wide variety of electronic and optoelectronic devices exist thanks to the possibility of exploiting the ground-breaking properties and interactions of ever-developing semiconducting materials. To achieve such a variety and optimisation of devices, studies on both architectures

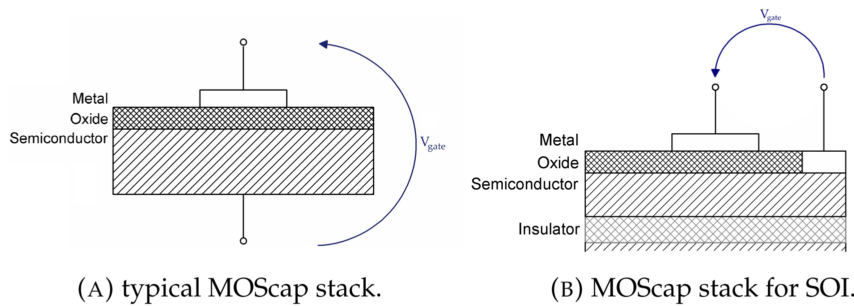

(A) typical MOScap stack. (B) MOScap stack for SOI.

FIGURE 1.13: MOS capacitors structures.

and materials have been carried out in the last decades. A very important role in the research is played by the MOS capacitor, a macroscopic MOS system that simulates the gate region behaviour in MOSFETs and other planar electronic devices.[3] Screening on gate dielectrics, gate metals, channel materials, compatibility of each interface, the effects of the materials and growth choices on electrical behaviour of the gate and some of the technological aspects of the process flow of CMOS fabrication is carried on MOS capacitors.
The MOS capacitor is schematically depicted in figure 1.13a: it consists in a conducting electrode made of metal or heavily doped polycrystalline silicon, deposited on top of a dielectric layer (historically SiO_2), thermally grown or deposited on a doped semiconductor layer (historically Si). The metal and semiconductor work as electrodes between which there is the oxide dielectric; the ideal overall system is a parallel plate capacitor where the area of the plates is determined by the size and shape of the metallic contact deposited on top of the dielectric layer grown (or deposited) on the semiconductor. The voltage to the capacitor is applied between the back contact and the metallic electrode and it is called gate voltage V_{gate}, which is one of the fundamental variables for the MOS devices operation.[1–3, 55]
An alternative configuration is the silicon on insulator (SOI) system, of which the advantages have been exposed at page 15, that can't exploit a back contact due to the presence of another insulating layer interposed in between. Therefore, the substrate (body) contact needs to be placed on top of the MOScap, making sure there is direct contact with the semiconductor (figure 1.13b).

In this way, it is possible to test the material properties and the phoenomenology of the gate region in the device without the process, time, equipment and cost of the micro- or nanodevice fabrication, as well as releasing the stack behaviour to the size or architecture related effects. Extensive studies on Si/SiO_2/poly-Si MOS capacitors were carried out along the years [1, 3, 55], and the following derivations are all taken from the latter mentioned sources, mainly Taur-Ning, *Fundamentals of Modern VLSI devices* and Nicollian-Brews, *MOS (metal oxide semiconductor) physics and technology*.

The response of a generic MOS gate region to an applied gate bias is crucial to understand the correlation of structural, electronic and electrical properties.
Every system that does not show quantum confinement of electrons is characterised by densely discrete energy levels, that are considered continuous bands: the distinction between metals, semiconductors and insulators depends on the magnitude of the energy gap present between valence and conduction band of the material.[56]

All the free-standing crystalline or amorphous materials have aligned vacuum levels, physical depiction of the fact that electrons need to possess a given energy to be expelled from any lattice they belong to. The average energy that electrons need to acquire from their state is different from system to system, and it is represented by the *work function* of the general *i* material $q\phi_i$: the workfunction is defined as the difference between vacuum level, representing the energy of the free electron, and Fermi level, representing the electron average energy in the material. For the doped semiconductor in the MOS gate stack, for example:

$$q\phi_s = q\chi + \frac{E_g}{2} + q\psi_b \tag{1.1}$$

where $q\phi_s$ is the semiconductor's work function, $q\chi$ is the electron affinity of the material (the difference between vacuum level and conduction band), $E_g/2$ is the Fermi level position in an intrinsic semiconductor and $q\psi_b$ is the deviation of E_f from the intrinsic Fermi level produced by doping with electron donors or acceptors. $q\psi_b$ is function of the doping level through the expressions:

$$q\psi_b = E_f - E_i = k_b T \ln\left(\frac{N_d}{n_i}\right) \qquad < 0 \tag{1.2}$$

$$q\psi_b = E_f - E_i = k_b T \ln\left(\frac{N_a}{n_i}\right) \qquad > 0 \tag{1.3}$$

where 1.2 stands for p-doped materials, being N_d the density of donors, and 1.3 stands for n-doped materials, being N_a the density of acceptors; E_i and n_i are the Fermi level and the density of carriers in the intrinsic semiconductor.
When different materials are put in contact, their Fermi levels are aligned and the vacuum levels are be continuous at the interfaces. The alignment of Fermi levels generates a built-in electric field at the semiconductor interface and through the oxide, that develop respectively a surface potential ψ_s, that causes a band bending at the interface with the dielectric, and a potential drop across the latter. A graphic representation of the effects of the built-in electric field is shown in figure 1.14.

When the gate voltage V_{gate} is introduced, the flatband situation associated to $V_{gate} = V_{fb}$ is just a particular case of the general behaviour of the stack, and it depends to the type and level of doping in the semiconductor, as well as oxide charges and interface traps that are not evaluated in this work.
Three conditions of charge distribution can be verified in the MOS capacitor, according to the applied gate voltage:

- accumulation;
- depletion;
- inversion.

The gate voltage application effect on band alignment and charge distribution for p-doped and n-doped semiconductor is shown in figure 1.15.

Considering n-type doping situation:
Accumulation: for $V_g - V_{fb} > 0$, the bands are bent downwards and electrons in

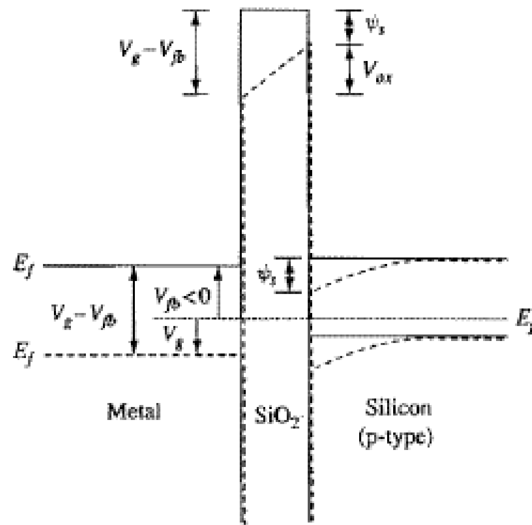

FIGURE 1.14: band diagram of a MOS system with p-doped Si under conditions of flatband voltage (continuous line) and zero gate voltage applied (dashed line), where semiconductor band bending and the effect of the electric filed in the oxide is visible.[3]

the conduction band, which are the majority carriers, accumulate at the interface with oxide. The resulting high charge density at the surface is the channel region in MOSFETs. An equal amount of positive charges are accumulated at the metal-oxide interface to maintain charge neutrality, developing a capacitance through the dielectric layer.

Depletion: for $V_g - V_{fb} \lesssim 0$, the electrons in the conduction band are depleted from the interface due to the negative potential at the oxide interface, resulting from the positive electric field that points the interface that induces electrons to be dragged towards bulk Si. The lower amount of interface charges translates in a lower capacitance across the dielectric layer.

Inversion: for $V_g - V_{fb} <$ or $<< 0$, the bands are strongly bent upwards: electrons are dragged towards the bulk crystal, and the valence band edge at the oxide interface is close to E_f. Therefore, a positive charged layer is actually created in the n-type semiconductor due to the application of a gate voltage, which is called inversion layer, hence the inversion regime of operation. Two different levels of inversion can be reached: in the beginning, a hole-rich layer is found at the SI-SiO_2 interface but their concentration is still lower than the electrons concentration in bulk that comes from doping and the condition is called of *weak inversion*. When the holes accumulated at the interface have a concentration higher than the majority carriers in the bulk, the condition is called *strong inversion*. Both can be used for channel regions and they shield the semiconductor from the electric field penetration in the semiconductor, avoiding to reach a too thick depletion layer.

Steady state electrical characteristics of the MOS capacitor are therefore derived by testing the capacitance of the system with the application of a bias. With steady state is intended the regime in which the system's macroscopic parameters are time independent or varying sinusoidally in time, while their amplitudes are strictly constant in time.[55] Two possible definitions of capacitance can be applied:

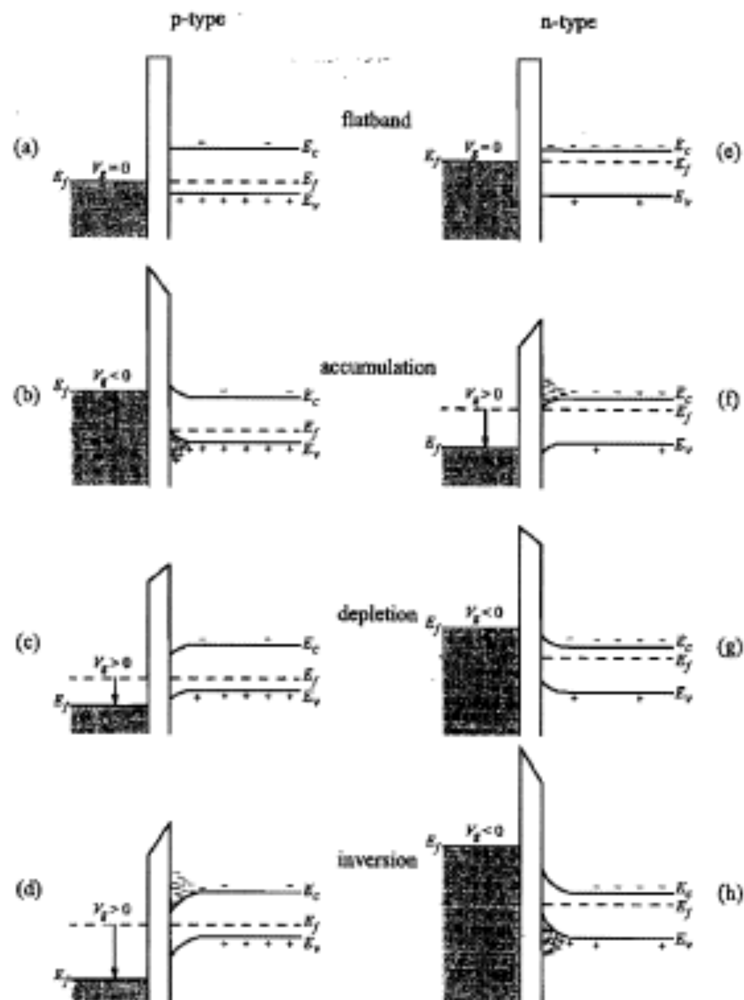

FIGURE 1.15: energy band diagrams for ideal p-type ((a) to (d)) and n-type ((e) to (h)) MOS capacitors with flatband voltage equal to zero. (a)-(e): flatband condition; (b)-(f): accumulation; (c)-(g) depletion; (d)-(h): inversion.[1]

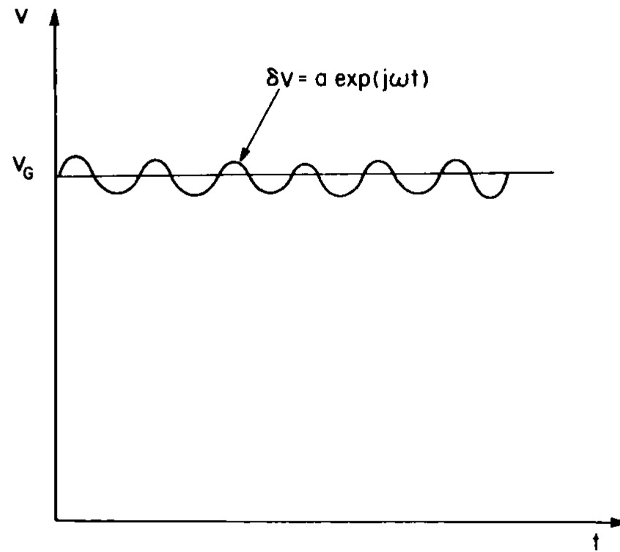

FIGURE 1.16: form of the probe applied for C-V testing; AC contribution falls in the range of small signal.

the first is called static capacitance and it corresponds to the total charge at the capacitor's plate with respect to the overall voltage applied between the plates; the second is called differential capacitance and it is defined as the incremental charge on the plate corresponding to an increment of voltage between the plates.

$$C_{stat} \equiv \frac{Q_{tot}}{V_{gate}} \qquad C \equiv \frac{dQ_{tot}}{dV_{gate}}$$

These two definitions are interchangeable when the system behaves linearly with the applied voltage, but it is not the case for MOS systems; therefore, differential capacitance is generally intended when capacitance is mentioned without any further specification.

The alternate voltage applied to the capacitor must be:

1. a **small signal**, where for small signal is intended the alternate voltage amplitude falling in a range that induces a linear response of alternate current. In this way, alterations from linearity can be evaluated and attributed to interface traps and charge non-uniformities on the dielectric surfaces;[55]
2. in **steady state** regime to avoid evaluation errors because of transients.

Indeed, to test electrical properties and simulate the operative conditions, it is required to produce charge separation in the MOScap; therefore, the applied signal is a base of constant DC voltage with a superimposed small AC voltage signal, as shown in figure 1.16.

The applied voltage has a form:

$$V_G(t) = V_G + \delta V_G(t) \tag{1.4}$$

this causes a small-signal variation in the semiconductor's band bending ψ and in the charge Q accumulated in the capacitor; in the small signal approximation, it's possible to express the time-varying total charge as function of the band bending, which is time-varying and depending to the gate bias, approximating to a Taylor expansion stopped at the first term:

$$\psi_s(t) = \psi_s + \delta\psi_s(t)$$
$$Q_s(t) = Q_s[\psi_s + \delta\psi_s(t)]$$

$$Q_s(t) = Q_s(\psi_s) + \left(\frac{\delta Q_s}{\delta\psi_s}\right)\delta\psi_s(t) \tag{1.5}$$

where the subscript *s* stands for semiconductor. Therefore, by definition of differential capacitance:

$$\begin{aligned}\delta Q_s(t) &= \left(\frac{\delta Q_s}{\delta\psi_s}\right)\delta\psi_s(t)\\ &= -C_s(\psi_s)\delta\psi_s(t)\end{aligned} \tag{1.6}$$

This expression can be related to the measured capacitance as function of the applied gate bias:

$$C = -\frac{\delta Q_s}{\delta V_G} = -\frac{\delta Q_s}{\delta\psi_s}\frac{\delta\psi_s}{\delta V_G} \tag{1.7}$$

where the band bending can be related to the electric field in the dielectric layer through Gauss law. In fact, imposing charge balancing at the dielectric-semiconductor interface, it is possible to derive the relation:

$$\begin{aligned}C_{ox}(\delta V_G - \delta\psi_s) &= C_s(\psi_s)\delta\psi_s\\ \delta\psi_s &= C_{ox}[C_{ox} + C_s(\psi_s)]^{-1}\delta V_G\end{aligned} \tag{1.8}$$

and therefore the expression of the measured capacitance as function of gate bias, substituting 1.8 and 1.6 in 1.7, giving the final contribution to the total capacitance.

$$C = -\frac{\delta Q_s}{\delta\psi_s}\frac{\delta\psi_s}{\delta V_G} = C_s(\psi_s)C_{ox}[C_{ox} + C_s(\psi_s)]^{-1} \tag{1.9}$$

The latter can be rearranged in:

$$C = \frac{1}{C_s(\psi_s)} + \frac{1}{C_{ox}} \tag{1.10}$$

that shows the total capacitance given by the contribution of the semiconductor surface and the oxide elements in series. The capacitance given by the surface

charge in the semiconductor is thus subjected to follow the voltage alternation through the response time of the charge carriers, that depends on the carrier and on the temperature; in Silicon it also depends on the light incident to the semiconductor surface, but this contribution is negligible for high band gap semiconductors like III-V nitrides. The minority carriers response time is much longer than the majority carriers response time: therefore inversion is visible in a C-V curve only at frequency lower than the inverse of the response time of the minority carriers. Figure 1.17c shows the frequency dependence of the inversion condition.

A relevant material property that can be derived from the C-V curves is the relative permittivity of the oxide, evaluated from the oxide capacitance. Several approaches are present to extract the oxide capacitance from the C-V plot, depending on the equivalent circuit considered (the easiest form of which consists of the approximation to a single capacitor $C_{accumulation} \approx C_{oxide}$), two of which are described in section 2.3.2 on page 55.
Deviations from ideality of the MOS capacitor behaviour are represented by trapping of charges by defects and vacancies in the oxide and semiconductor, each trapping mechanism characterised by a response time that therefore shows effects according to the frequency of the measure. Trapping mechanisms are strongly related to the materials and interfaces, but they are not investigated along this work.
Nonetheless, a relevant component of the equivalent circuit to discuss is the series resistance, that is related to the intrinsic resistivity of the materials that constitute the MOS capacitor: oxide thickness and resistivity, area of the MOS capacitor and resistance provided by the semiconductor and its defects between the interface and the substrate contact all increase the series resistance. The series resistance of the oxide and semiconductor modifies the equivalent circuit of the MOS capacitor as depicted in figure 1.18: this influences the admittance in C-V measurements (experimental details in chapter 2). Series resistance can be measured or derived from the admittance in strong accumulation via the following relation:

$$R_s = \frac{G_a}{G^2{}_a + \omega^2 C^2{}_a} \tag{1.11}$$

where G_a is the admittance, C_a the capacitance and ω is the frequency of measure; therefore the capacitance measured by the instrument can be corrected according to the relation:

$$C_c = \frac{(G^2 + \omega^2 C^2)C}{a^2 + \omega^2 C^2} \qquad a = G - (G^2 + \omega^2 C^2)R_s \tag{1.12}$$

where C_c is the capacitance corrected by the series resistance measured or derived from 1.11.

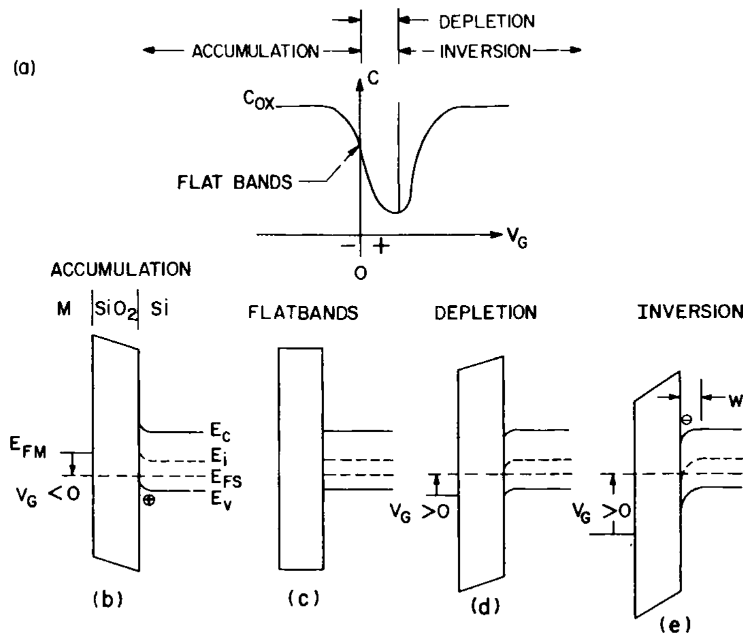

(A) capacitance measured in ideal p-type MOS capacitor as function of the applied voltage.

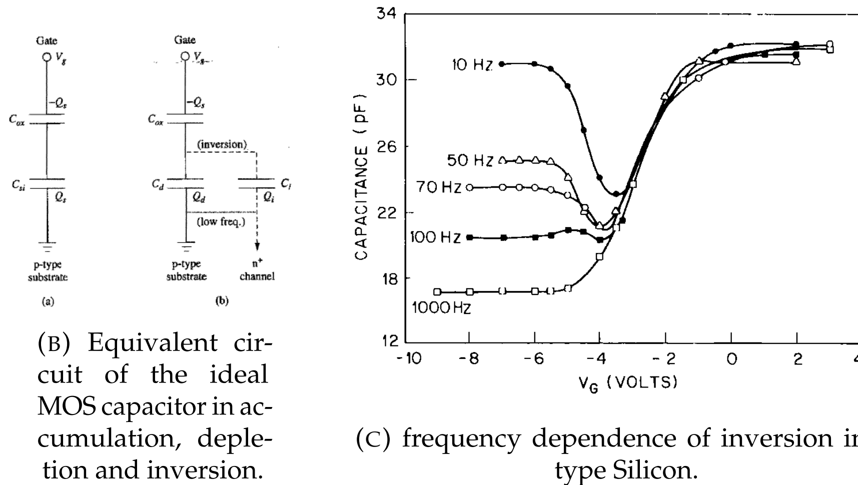

(B) Equivalent circuit of the ideal MOS capacitor in accumulation, depletion and inversion.

(C) frequency dependence of inversion in n-type Silicon.

FIGURE 1.17: capacitance response of a MOS capacitor under accumulation, depletion and inversion.

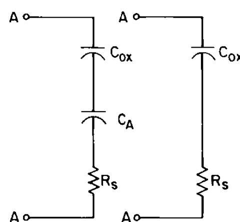

FIGURE 1.18: series resistance contribution to the MOS capacitor equivalent circuit in accumulation. On the right, the simplification of the circuit in strong accumulation where $C_a \approx C_{ox}$.

Goal of the research

This work treats the **correlation between crystallographic structure and electronic properties with the electrical behaviour of Metal/Rare Earth Oxide/III-V Nitride MOS capacitors**, in order to study new possible MOSFETs alternatives that benefit of the use of GaN as channel material and of a metal/high-κ gate. In particular this work focuses on the following aspects:

- investigation on the crystalline structure of Gadolinium Scandium Oxide $GdScO_3$ (GSO) grown on Wurtzite GaN deposited on a Si(111) substrate to check the possibility of rare earth oxide epitaxial growth, an advantage to achieve higher κ;
- investigation on the band alignment of GSO-GaN to understand the conduction band offset of the oxide-semiconductor interface;
- investigation on the quality of the semiconductor to understand how defective is the growth on a foreign substrate and how it affects the electrical behaviour of the gate stack;
- derivation of the relative permittivity of the high-κ dielectric;
- correlation of the electrical behaviour of the stack with the aforementioned band alignment and crystallographic structure;
- correlation of the differences between structure, band alignment and electrical behaviour of the gate stack when changing the materials with respect to the crystalline GSO-GaN/Si(111):
  - amorphous GSO instead of crystalline GSO;
  - crystalline Lutetium Lantanium Oxide $LaLuO_3$ (LLO) instead of GSO;
  - Wurtzite $Al_{0.5}Ga_{0.5}N$ instead of stoichiometric GaN;
  - GaN deposited on a Sapphire wafer instead of a Si(111) wafer.

Chapter 2

Experimental techniques

This chapter covers the analytical techniques used by the author to characterise the Rare Earth Oxide/III-V Nitride semiconductor systems. Fundamentals of X-ray diffractography are exposed, focusing on the investigation of the crystalline structure of epitaxial layers. Later in the chapter, interpretation of X-ray photoelectron spectroscopy spectra is discussed with an insight on the derivation of electronic features of materials; in order to ease the discussion, the experimental technique is recalled as well. At the end, an overview of setup and main features of electrical measurements are explained, focusing on the use of current-voltage and capacitance-voltage characterisation of semiconductor capacitors.

2.1 X-ray Diffractography (XRD)

2.1.1 Theory of diffraction

A crystal is a material with atomic structure characterised by translational symmetry, that consists of a periodic arrangement of atoms in space. This structure is energetically stable; the atomic arrangement follows specific rules of tessellation in order to completely occupy the space with identical cells, without leaving voids or overlaps in the structure. Seven possible mathematical objects, called Bravais lattices, satisfy these requirements: each cell of the lattice is then filled by atoms according to the chemical nature of the elements. The disposition of atoms in the fundamental cell is called base; the crystal is defined as the ensemble of lattice and base. The seven elementary Bravais lattices are summarised in figure 2.1 and their cell parameters and angles are defined in table 2.1.

Each atom in the crystal has radius of the order of magnitude of fractions of nm, therefore it acts as point scatterer for incident photons of wavelength of similar dimensions, producing spherical waves that propagate in the medium; the ordered array of scatterers induces constructive and destructive interference

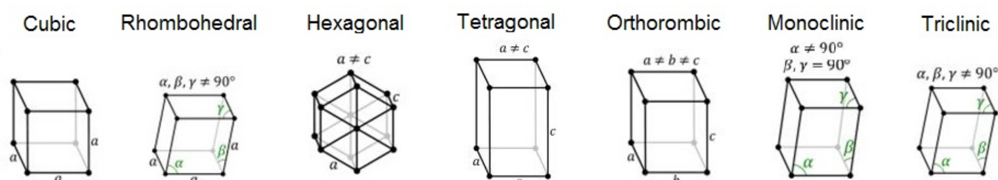

FIGURE 2.1: Bravais lattices in three dimensional space.

Lattice	Lattice constants	Angles
cubic	$a = b = c$	$\alpha = \beta = \gamma$ =90°
rhombohedral	$a = b = c$	$\alpha = \beta = \gamma \neq$90°
hexagonal	$a = b \neq c$	$\alpha = \beta = \gamma$ =120°
tetragonal	$a = b \neq c$	$\alpha = \beta = \gamma$ =90°
orthorombic	$a \neq b \neq c$	$\alpha = \beta = \gamma$ =90°
monoclinic	$a \neq b \neq c$	$\alpha = \beta$ =90°, $\gamma \neq$90°
triclinic	$a \neq b \neq c$	$\alpha \neq \beta \neq \gamma \neq$ 90°

TABLE 2.1: Bravais lattice groups and their features for the tessellation of space.

of the spherical waves, causing the phoenomenon of diffraction of the incident beam in the long range approximation as described first by Von Laue experiment for single crystals.[56] The principle of X-ray diffractography is to exploit the detection of the diffraction pattern of an X-ray beam (λ $\approx 10^{-1}$ Å) to reconstruct the crystallographic features of a crystal. The constructive interference of the scattered waves follows the Bragg's law in long range approximation:

$$n\lambda = 2d \sin\theta \tag{2.1}$$

where n is the diffraction order (usually just $n = 1$ is considered), λ is the incident beam and scattered beam wavelength assuming elastic scattering, d is the interplanar spacing between atomic layers, and 2θ is the angle of the scattered beam with respect to the incident beam direction. Therefore, measuring 2θ of the first order diffracted beam knowing λ of the probe, enables to derive the interplanar spacing d and thus, the atomic spacing in a given direction, which is or is associated to a specific cell parameter.
The direction of the scattered wave with respect to the incident wave is defined as *transfer wavevector* $\vec{Q}$:

$$\vec{Q} = \vec{k_s} - \vec{k_i} \qquad ; \qquad |\vec{Q}| = 2|\vec{k_i}| \sin\left(\frac{\theta}{2}\right) \tag{2.2}$$

where k_i is the incident wavevector and k_s is the scattered wavevector. The transfer wavevector is a reciprocal lattice vector $\vec{Q} = g_{\vec{hkl}}$.
According to the reciprocal space notation, crystallographic planes in the real space are denominated with Miller indexes (hkl) so that $d = d_{hkl}$, with indexes:

$$h \equiv 2\pi \frac{b \wedge c}{V_{cell}}; \qquad k \equiv 2\pi \frac{c \wedge a}{V_{cell}}; \qquad l \equiv 2\pi \frac{a \wedge b}{V_{cell}} \tag{2.3}$$

and $V_{cell} = a \cdot b \wedge c$.[57] Figure 2.2 shows some examples of the relation between Miller indexes and crystallographic planes in the real space primitive cell. A particular notation is usually adopted for hexagonal crystals, with four Miller indexes instead of three where the fourth index is redundant: *(hkil)*, with $i = -h+k$. In the current work, the three-indexes notation is kept for hexagonal lattices too, referring to one of the three primitive cells that compose the hexagonal one.

Different crystallographic planes can be detected as function of the relative position of the incident beam wavevector, the crystalline surface orientation and

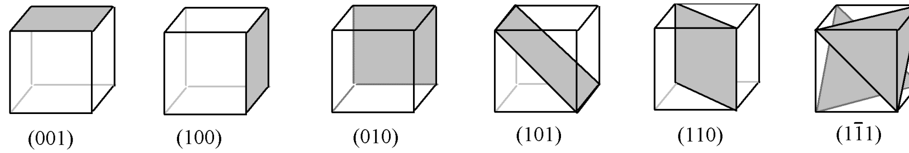

FIGURE 2.2: Miller indexes in relation to the crystallographic planes they define.

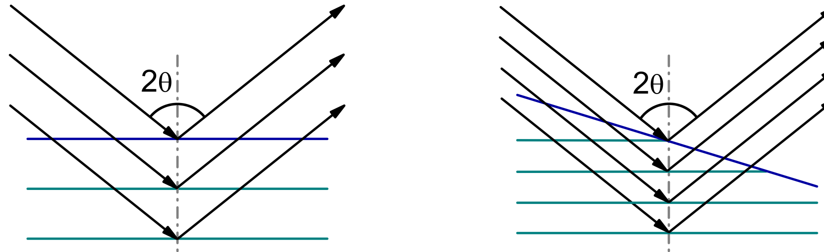

FIGURE 2.3: the d-spacing measured from the scattering angle is dependent on the sample orientation with respect to the incident beam, in single crystals and grains. On the left, a crystal with surface parallel to the ground with relative crystallographic planes; on the right, the crystalline domain is tilted and the scattering wavevector is no longer surface normal, therefore different planes are measured.

the detected scattered beam wavevector. Since translational symmetry can span up to macroscopic dimensions in single crystalline solids, the orientation of the sample surface with respect to the incident and detected wave is also relevant in the determination of the d-spacing detected during the analysis; for polycrystalline materials, instead, each crystalline domain is called grain and the random orientation of grains statistically ensures the detection of a designated (hkl) plane without any rotation of the sample from its reference position, usually kept with the surface parallel to the ground (figure 2.3).

2.1.2 XRD experimental apparatus

An X-Ray diffractometer consists of an apparatus of which the main components are a **source (S)**, that can send an X-ray beam on the surface of the sample through incidence optics, a **stage** able to change the sample orientation by rotation around its axes, and a **detector (D)** of the same wavelength X-ray radiation. Given the crucial role of the incident and scattering angle, both incidence and receiving optics are mounted on a precision **goniometer**. The general configuration of an XRD with the most important geometrical parameters is shown in figure 2.4. Figure 2.5 instead shows the possible rotations of the sample on the stage; the rotational angles are extremely important for the construction of pole figures of a single crystal of unknown structure, which will be explained later in the chapter (page 38).

The general scheme of the components of an XRD is shown in figure 2.6.
The X-ray sources belong to two different families:

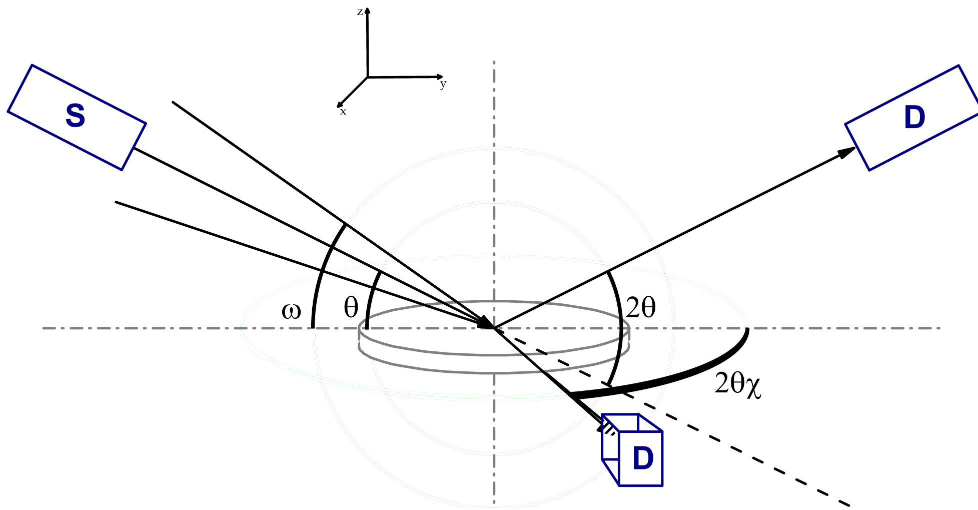

FIGURE 2.4: schematic of the angles involved in XRD measurements, where S stands for source-incidence optics and D stands for receiving optics-detector. Symmetric scattering is evaluated with θ-2θ configuration and $\vec{Q}$ is surface normal; asymmetric scattering is given by ω-2θ with $\omega \neq \theta$. Crystallographic planes with surface parallel $\vec{Q}$ produce scattered beam on the *xy* plane (more details in 2.1.3), therefore θ-2θχ angle is scanned.

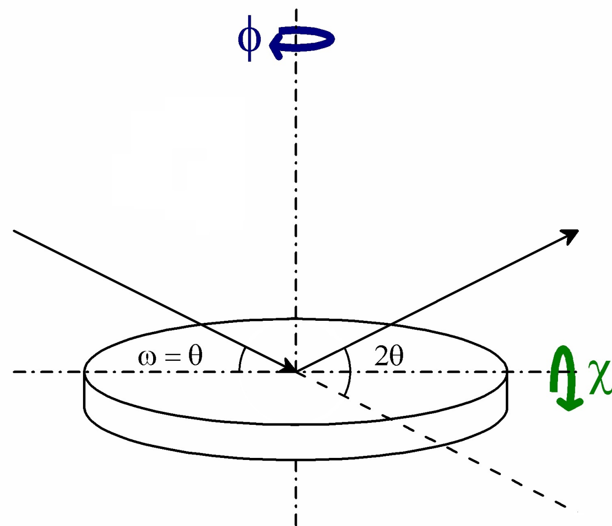

FIGURE 2.5: scheme of the sample rotation around its axes.

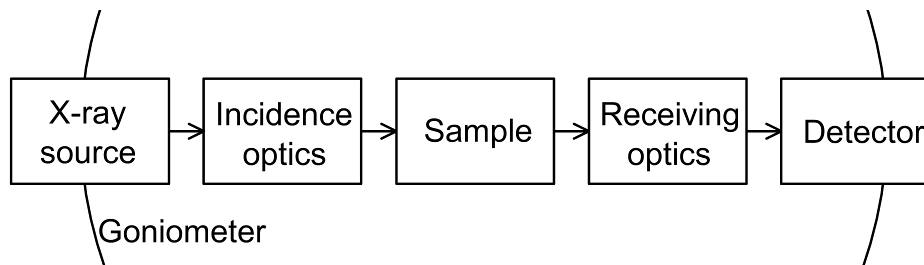

FIGURE 2.6: XRD block scheme of experimental apparatus.

- **vacuum tubes:** electrons emitted in vacuum from a Tungsten filament by thermionic effect impinge on an anodic metallic target, causing the electrons excitation and subsequent relaxation with a photon emission corresponding to the electronic transition;
- **synchrotrons:** charged particles that travel in a circular accelerator emit an electromagnetic wave with wavelength depending on the particle mass, energy and trajectory.

The lab-scale size and lower cost of vacuum tubes with respect to synchrotron facilities make the first largely the most used X-ray sources for diffractography. A vacuum tube for X-ray emission is shown in figure 2.7. The radiation produced is intrinsically polychromatic, usually made by a few lines from transitions of excited electrons to core levels and some Bremssrtahlung radiation. Using the X-rays notation for the electronic transitions, the most produced radiations are $K\alpha_1$, $K\alpha_2$, usually averaged in $K\bar{\alpha}$, and $K\beta_1$ radiation is produced, but it can be screened by an external window of material that absorbs its wavelength to keep just $K\overline{\alpha}$ which has higher intensity. The most important metal for anodes is Cu (λ: $K\alpha_1$ = 0.154059 nm, $K\alpha_2$ = 0.154441 nm, $K\beta_1$ = 0.139225 nm); other target metals are Cr, Fe, Co, Ni, Mo, Ag. According to the anode, different $K\alpha$ and $K\beta$ are produced and different $K\beta$ screening materials are used.

A system to improve the emission rates of X-rays from the vacuum tube is to make use of a rotating anode system: the anode rotation allows a better heat dissipation because the electron do not impinge always on the same spot of the material, therefore higher currents can be applied with no thermal degradation. This system generates X-ray emission rates 3-5 times higher than the stationary anode vacuum tube. For even higher emission rates required by the analysis, the use of a synchrotron is necessary.

Optics elements are mostly shadow casting (apertures and slits), since lenses and mirrors exist for X-ray radiation but it is hard to find non transparent materials to very energetic radiations. Incidence optics have the role of collimate, limit the divergence of the incident radiation, tune the spot size of the beam onto the sample and choose its geometry of focusing: parallel beam (PB) can be achieved from Bragg-Brentano (BB) geometry by the application of a capillary X-ray lens, where PB does not require very precise alignment of the sample and a strictly equal source-sample and sample-detector distance, but it provides a lower beam intensity due to the additional optics. Divergence slits on the incidence optics can be fixed or can vary with the incidence angle and sample size, in order always have sample bigger than the spot size; Soller slits are a series of equally spaced metallic platelets parallel to the beam direction that limit the vertical divergence

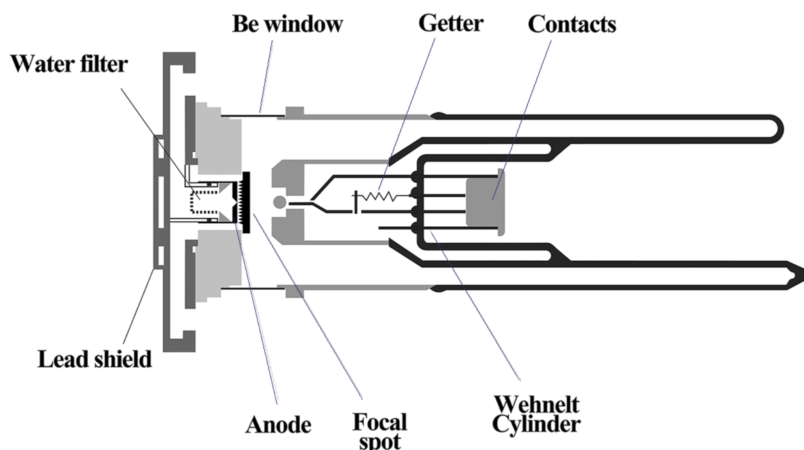

FIGURE 2.7: vacuum tube for X-ray generation.

of the radiation, especially for PB geometry. Monochromators make use of the diffraction polychromatic beam by single crystals, exploiting a scattering plane of a specific crystal that gives a very high intensity of the scattered beam. Ge(220), Si(111), LiCl and graphite flat crystals can be installed before the sample (incidence optics).[58] For high resolution XRD, the beam from the source bounces between two or four crystalline flat surfaces in order to have more scattering events to sort the emission wavelengths on the base of optical path of the light between the crystals. Curved crystal monochromators, used in Bragg Brentano geometry, are instead placed in the receiving optics side of the instrument.

The receiving optics before the detector include divergence slits, soller slits and apertures like the incidence optics, because the sample acts as a point source for the scattered radiation; an attenuator is also necessary to avoid damages to the detector in case of a too intense diffracted beam. In absence of a monochromator, a Kβ filter can be placed in the receiving optics branch of the apparatus.

Finally, there are several families of detectors for X-ray radiation:

- **X-ray photographic film:** X-ray scattered beams impress a film on a curved surface from which projection the angles can be calculated. It is an obsolete technique;
- **Gas ionization chambers:** X-rays from a scattered beam ionize gas molecules in a chamber, which are conveyed by a potential difference towards an electrode giving raise to a signal;
- **Scintillating crystals:** X-rays from a scattered beam impinge on a crystal that emits light by fluorescence, which is conveyed to a photomultiplier after which an electrical signal is detected;
- **Semiconductor detectors:** X-rays from a scattered beam induce an electron-hole separation in an intrinsic or Li-doped semiconductor, that registers a current flowing due to holes and electrons (or Li^+) drifting when a voltage is applied.

Semiconductor detectors and gas chambers allow the positional determination of the signal because arrays can be obtained, while scintillators and photographic film count signal from any point of the spot size without distinction.

Finally, the goniometer and movement system of source, stage and detector determine the angular resolution of the measurement and the degrees of freedom that can be achieved (ref. figure 2.4).

Different geometries of signal acquisition provide different information about the system under analysis. The present experimental works treats single crystalline samples and epitaxial thin films, therefore the focus of the following sections will be on diffractographic techniques for single crystals, while powder diffractions are henceforth disregarded.

2.1.3 X-ray diffractometry for the characterisation of crystalline films

Symmetric scattering: XRD θ-2θ

A θ-2θ measure is the evaluation of symmetric scattering, achieved when $\omega = \theta$ and 2θ is the detection angle, with surface normal transfer wavevector; therefore, surface-parallel planes are detected.

It is possible to detect different crystallographic planes by maintaining the symmetric scattering condition and tilting the sample when this is single crystalline. In this way, an analogous effect of asymmetric scattering is achieved, and non surface-parallel planes are detected. The achievement of signal from a specific non surface-parallel plane when tilting the single crystalline sample is subordinate to the in-plane orientation of the crystal with respect to the incident and detected beam direction. Therefore, a ϕ scan with fixed θ-2θ (of a designed plane to investigate) after tilting χ is necessary to align the sample; in order to do this, the lattice of the sample (or part of it, in case of layered structures) must be known in order to choose the correct θ-2θ.

Once the spectrum is obtained, it is possible to use databases to interpret the lattice plane where the reflection comes from, or Bragg's law to evaluate the d-spacing from the 2θ of scattering and therefore geometrical considerations to compute the lattice parameter. The latter is the only option in case of phases not recorded in literature.

Knowing that GaN is hexagonal, for example, the (101) d-spacings are related to the in-plane lattice parameter a_{hex} through the equation:

$$a_{hex} = \frac{d_{101}}{\sin(\frac{\pi}{3})\sin(\arccos(\frac{d_{101}}{c_{hex}}))} \tag{2.4}$$

with d_{101} interplanar distance obtained from Bragg's law and scattering angle 2θ, c_{hex} out of plane lattice parameter derived from θ-2θ measurement, and $\pi/3$ is α of the hexagonal cell. The same formula applies in case the GSO layer turns out to be actually epitaxial, therefore hexagonal, on top of GaN. Other cases can be evaluated by geometrical considerations or consulting of pre-derived formulas from literature.[59]

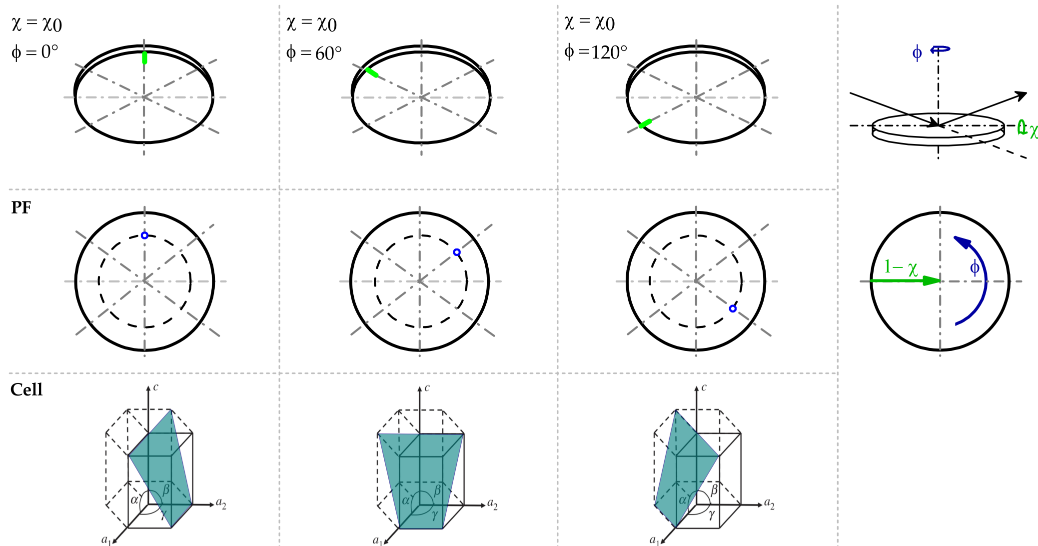

FIGURE 2.8: construction of a circular crown of pole figure, for an example of hexagonal (001) surface-oriented crystal. θ-2θ iincident and scattered beam are neglected in figure. The ϕ rotation shown is of 120° only, with fixed χ. The sample tilting of χ allows to detect interference of (101) planes of the hexagonal cell, that show six-fold point symmetry around the vertical axis, producing constructive interference every 60°.

Asymmetric scattering: XRD ω-2θ

Asymmetric scattering is described when $\omega \neq \theta$, and non surface-parallel planes diffraction maxima are detected. It is an extremely relevant method for powder diffraction as the sample is composed by grains randomly oriented in space; for experiments where the sample is single crystalline, the effect is the same of tilting the sample in θ-2θ geometry as explained in 2.1.3.

In-plane XRD

The in-plane measurement is a symmetric scan of the crystallographic planes orthogonal to the surface of the crystal. It can be seen as a θ-2θ scan lying on the xy plane instead of the yz plane, still according to the reference system shown in 2.4. This geometry is achieved by means of a second goniometer orthogonal to the ω-2θ goniometer used for all the other analyses. The angle along the plane is defined as 2θχ according to angular projections of the instrument. A minimal value of θ-2θ is kept in order to produce an X-ray evanescent field in the crystal, that propagates with wavevector parallel to the surface along all the sample instead of hitting directly a very low cross section of the sample with θ-2θ = 0°, especially in the case of thin films.[60]

Pole Figures

A pole figure is the construction of a spectrum by fixing θ-2θ in a value where a reflection is present and rotating the single crystal along χ and ϕ to achieve information on in-plane symmetry of the crystal, which in principle can be unknown;

on its orientation in plane, which is of particular interest in the case of epitaxial layers grown on top of a substrate to understand the relative orientation between the two; finally some information on the crystal quality and mismatch between a substrate and its epitaxial layer can be derived, even though other analyses can give the same information in a better reliable way (2.1.3, 2.1.3). The acquisition is performed as follows: first, a θ-2θ pre-scan is performed to detect surface-parallel planes contributions. Then, θ-2θ is fixed on the position of a centre peak of interest, outcome of θ-2θ analysis; once fixed the angle, therefore the d-spacing that can be detected during the analysis, χ tilting angle must be scanned to obtain non surface-parallel planes contributions: since the orientation of the crystal in plane is in principle unknown, χ is scanned in fixed steps where for each a 360° ϕ scan is performed by rotating the sample along its normal. The complete PF is obtained by scanning ϕ continuously for each χ step between 0° (sample parallel to xy plane) and 90° (sample perpendicular to xy plane). The PF representation is the depiction of the acquired spectrum in ϕ-(1-χ) polar coordinates, where latitude is associated to (1-χ) and longitude is ϕ.[61] Representing (1-χ), the pole is equivalent to no tilting: therefore, the θ-2θ contribution is always visible at the pole in agreement to the fact that θ-2θ for the pole figure was chosen according to a surface-parallel plane reflection. Usually, the PF is acquired with non monochromated radiation in order to maximise the signal acquisition; therefore also θ-2θ pre-analysis should be performed without monochromator.

The number of reflections along one or more circular crowns are an indication of the symmetry and orientation of the crystal under analysis: for example, three-fold symmetry can be associated to a cubic (111) face, or a six-fold symmetry can be associated to an hexagonal (001) face (or multiplicities). The reflections need to be fitted to detect the centre peaks on the PF; subsequently, d-spacings can be processed to obtain cell parameters of the lattice group evidenced by the symmetry along ϕ according to the methods already mentioned for θ-2θ measurements.[59]

Rocking Curves

Rocking curves are a method of evaluation of the quality of a crystal. θ-2θ scans give signal from specific (hkl) surface parallel planes: the more ideal is the crystal, the less the planes orientation deviate from the parallel to the surface. Scanning ω around θ while keeping 2θ fixed in the position of a given (hkl) surface parallel peak, an asymmetric scattering geometry is achieved. If the crystal is perfect, no signal should come from the asymmetric scattering geometry until another non surface-parallel plane is detected, and the intensity as function of ω should be very sharp and centered in ω = θ. Signal will be instead provided if the crystallinity is imperfect. Therefore, the FWHM of the latter peak is an indication of the crystal quality, especially for comparison among epitaxial layers, of which the crystalline quality is an important parameter to evaluate the growth and compatibility on the substrate.

X-ray Reflectivity (XRR)

X-ray reflectivity is the analysis of a reflected X-ray beam at very low θ-2θ angles by a thin film. The interference between the surface of the sample and the film-substrate interface acts as scatterer instead of the crystallographic planes at very

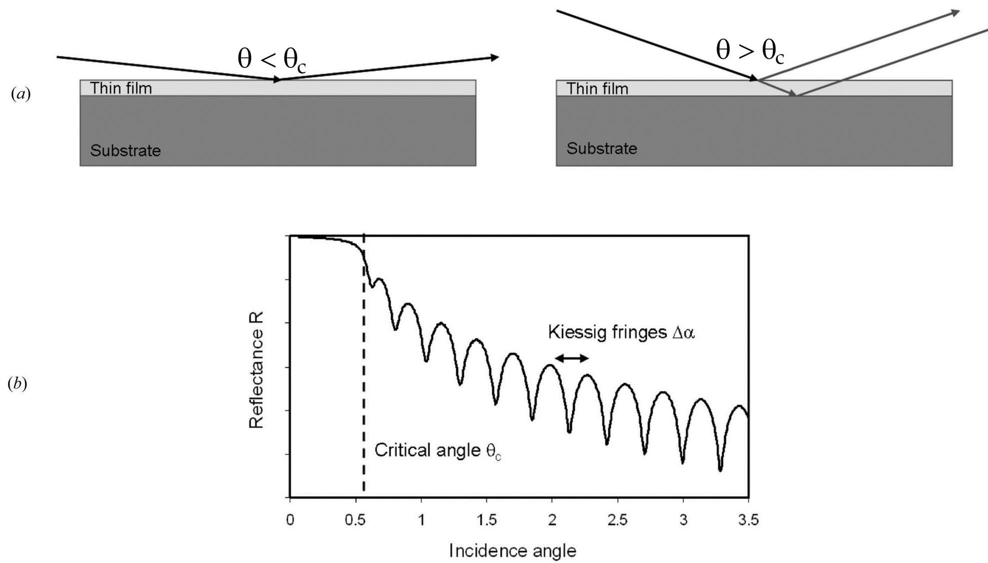

FIGURE 2.9: XRR (a) phoenomenon and (b) spectrum with the information provided by the technique.[64]

low angles, according to Bragg's law where the interlayer distance is much larger than the crystallographic planes spacing. The (relatively) large thickness of the layer produces interference fringes, called Kiessig fringes, of which interspacing is an indication of the film thickness.[62, 63] Therefore, fitting the XRR spectrum acquired at low angles (between $\approx 0°$ and $\approx 10°$) it is possible to evaluate:

- the film thickness by the fringes spacing (figure 2.9);
- the film density by the critical reflectance angle θ_c, proportional to $\sqrt{\rho}$[62], indication of the wave propagation in the medium;
- the interface and film roughness, evaluated through the slope of the reflectance curve, because rough surfaces give raise to diffuse scattering that results in a lower intensity of the reflected beam detected at 2θ.

Reflectivity features can be visible also in θ-2θ high resolution measurements, in the form of fringes around a peak coming from the thin film called Pendellösung (thickness) fringes. They are an indication of the thickness of the thin film that produces the signal , which can be evaluated by:

$$t = \frac{\lambda_{source}}{2\Delta\omega_f \cos(90 - 2\theta)} \tag{2.5}$$

where λ_{source} is the source wavelength, $\Delta\omega_f$ is the spacing between the fringes in radians, and 2θ is the scattering angle of the centre of GSO(002) peak in degrees.[65]

2.2 X-ray photoelectron spectroscopy (XPS)

X-ray photoelectron spectroscopy (XPS) is an electron spectroscopy technique that provides information on electronic levels of sample surface atoms. The basic

principle of the technique is the detection of the kinetic energy of electrons emitted by photoelectric effect, using monochromatic X-ray radiation for probe.

2.2.1 Theory of photoelectric emission for XPS analysis

When a sufficiently energetic photon is absorbed by an atom, one electron is ejected from the atomic orbitals to the vacuum level, where it becomes a free electron travelling in vacuum with a residual energy provided by the radiation. The kinetic energy (KE) of the photoemitted electron is given by the energy balance expressed by Einstein equation:

$$h\nu = BE^{vac} + KE \qquad \Rightarrow \qquad BE^{vac} = h\nu - KE \tag{2.6}$$

where $h\nu$ is the X-ray incident radiation, KE is the kinetic energy of free electron travelling in vacuum, BE^{vac} is the binding energy of the electron to the atom with the vacuum level as a reference. The Binding energy is defined as the difference between the electron final state and initial state:

$$BE^{vac} = E_f(n-1) - E_i(n) \approx -\epsilon_k \tag{2.7}$$

according to Hartree-Fock calculation, where $-\epsilon_k$ is the orbital energy for the emitted photoelectron.
Hartree-Fock takes into account neutral atoms only. Initial state effects and final state effects influence $E_i(n)$ and $E_f(n-1)$ respectively, leading to shifts in the BE and therefore in the KE detected by the instrument. In particular:

- **Initial state effects** are factors that determine the initial state of charge of the atom before the radiation interaction:
  - orbital hybridisation;
  - oxidation state;
  - polarity of bonds with the chemical environment;
  - charging effects in non conducting samples caused by previous photoemissions;
- **Final state effects** are factors that influence the state of charge during the photoemission or after it:
  - relaxation of the levels around the core hole;
  - secondary transitions following the generation of the core hole;
  - formation of multiplets.

It is possible to define the binding energy as the difference between electronic orbital and Fermi level, instead of taking the vacuum level as a reference, by using the definition of workfunction of a system:

$$\phi_i = E_{vacuum\,i} - E_{F\,i} \tag{2.8}$$

Therefore the Einstein equation (2.6) becomes:

$$BE^{vac} = BE^{F} + \phi_{analyte} \tag{2.9}$$

$$h\nu = KE + (BE^{F} + \phi_{analyte}) \tag{2.10}$$

where BE^F is the binding energy relative to the Fermi level and $\phi_{analyte}$ is the element workfunction, in principle unknown.
Sample and instrument are in contact, therefore their Fermi levels are aligned instead of the vacuum levels, and the kinetic energy detected by the instrument suffers an evaluation error if equation 2.10 is the only considered. The levels alignment is depicted in figure 2.10.
Considering the energy balance for the whole process of photoemission and detection, the proper BE^F can be computed from the KE of the electron as detected by the instrument. For grounded samples:

$$\begin{cases} KE_{analyte} = h\nu - (BE^{F} + \phi_{analyte}) \\ KE_{instr} = KE_{analyte} + (\phi_{analyte} - \phi_{instr}) \end{cases} \tag{2.11}$$

$$\Rightarrow \qquad BE^{F} = h\nu - KE_{instr} - \phi_{inst} \tag{2.12}$$

where BE^F is the Binding energy relative to the Fermi level, KE_{instr} is the kinetic energy detected by the spectrometer, and ϕ_{inst} is the workfunction of the spectrometer. It is very important to notice the release of the BE^F dependance from the unknown sample workfunction.

For insulating samples, neither the Fermi levels nor the vacuum levels are aligned because of the impossibility of the electrons to freely migrate in the material under the driving force of ΔE_F. Vacuum levels are misaligned by the electrostatic energy induced by non-compensated photoemission:

$$BE^{F} = h\nu - KE_{instr} - \phi_{instr} + E_{ch} \tag{2.13}$$

analogous of equation 2.12 with an addition of E_{ch} term, the lowering of the electronic levels caused by charging. The sample charging is taken into account in the spectrum by using a reference peak that does not shift with charging, for example depositing a strip of a conductor grounded with the instrument to make it a reference; otherwise, charge compensation methods are used in order to limit the effect (ref. 2.2.3).
BE^F is shortened in BE or B.E. without any superscript along the present work.

Escape depth of electrons

X-rays are highly penetrating into matter: as seen for XRD (in 2.1), light can be scattered by the sample bulk. Electrons show significant reduced capacity to travel in solids instead. When an electron is photoemitted from the bulk it needs to cross

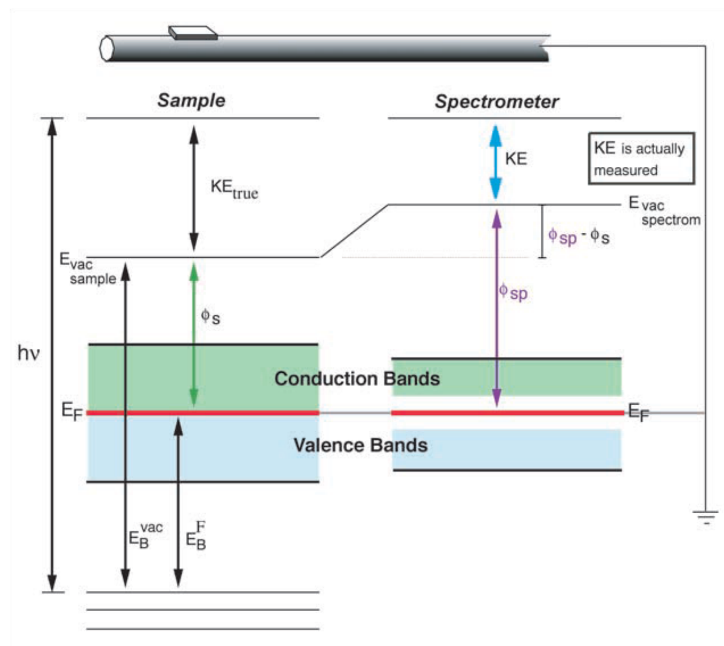

FIGURE 2.10: electronic energy levels alignment of sample and instrument in contact.

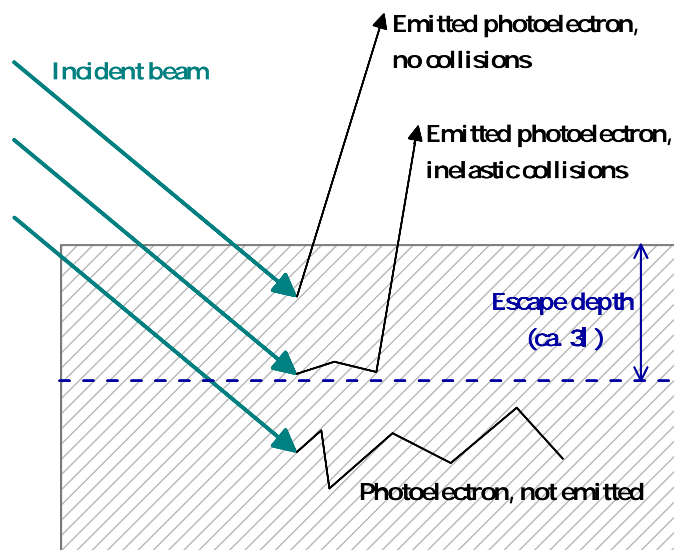

FIGURE 2.11: escape depth of electrons from the surface. For larger depth, inelastic collisions dissipate the energy absorbed by the X-ray radiation until the vacuum level is no longer reached.

several atoms that are present in the overlayer: doing so, it loses energy due to inelastic collisions. The electron can still be emitted from the sample surface if its energy exceeds the vacuum level, otherwise it is bound to the material with an exceeding energy that will be released in a relaxation process. Electrons that travel without any energy loss will carry information on their actual BE, expressed in term of their KE of collision on the detector; electrons that escape from the surface after inelastic collisions will be characterised by a lower KE, therefore the BE calculated from equation 2.12 will result higher than the actual BE of the original electronic level, and the electron will contribute to the background signal at higher BE (lower KE). The average depth, normal to the surface, from which the photoelectrons are able to escape is defined *mean escape depth* (ED), and it includes electrons emitted elastically and inelastically as shown in figure 2.11. The average distance that an electron with a given energy travels between inelastic collisions is named *inelastic mean free path* λ, function of the incident wavelength. In the hypothesis of uniformity of the energy absorbed by a unitary thickness overlayer, which implies that the energy absorbed from the photoelectron by an atom is constant disregarding where the atom is located in the overlayer, Beer law for absorption is valid:

$$I_k = I_0 exp\left(\frac{-d}{\lambda cos\theta}\right) \tag{2.14}$$

where I_k is the exiting intensity of photoemitted electrons, I_0 is the intensity of the incident radiation, d is the optical path which is, in this case, the overlayer, λ is the inelastic mean free path expressed in atomic monolayers, θ is the angle of emission of the electron with respect to the surface normal (*take off* angle). When $d = \lambda$, $I_k = I_0 \cdot 1/e$ that means around 63% of the electrons will be subjected to energy loss.
This implies that:

$$d = 3\lambda \qquad \Rightarrow \qquad \approx 95\% \text{ of the signal comes from } d \tag{2.15}$$

Therefore, the sampling depth of the technique is usually considered $\approx 3\lambda$.
The inelastic mean free path of electrons in a solid falls in the range of 1÷4 nm, which means a maximal sampling depth of roughly 10 nm. This is the reason why XPS is a very surface sensitive technique, and not suitable for bulk analysis despite the X-rays penetrate through the sample.

2.2.2 Experimental apparatus

A generic XPS apparatus is shown in figure 2.12. It is possible to distinguish several fundamental elements:

- **X-ray source:** as seen in section 2.1.2 for X-ray diffractography, X-rays can be produced from a vacuum tube or from a synchrotron;
- **Sample stage:** the stage needs a manipulator that allows movement in xy plane and along z, in order to focus on specific spots and to move the sample vertically to accomodate samples of different thickness without moving the incidence optics;

- **Electron flood gun:** charge compensation system for insulating samples;
- **Collection lens:** collects electrons from the chamber, conveys them into a parallel beam to the energy analyser, and selectively reduces their energy to the pass energy range of the analyser;
- **Energy analyser:** electron hemisperical lenses that deflect electrons according to their energy by means of an electrostatic field;
- **Detector:** counter of the electrons characterised by a specific kinetic energy, allowed to exit the hemispherical analiser, that converts the number of impinged electrons into electric signal;
- **Ultra high vacuum (UHV) system:** the experimental apparatus is placed in a vacuum chamber for the following reasons:
  - photoelectrons must travel from the surface to the detector without collisions with atoms, that cause measurement errors because of electron energy loss and deviation from the original trajectory;
  - the sample surface must be kept free of adsorbates along the analysis, therefore the monolayer formation time must be longer than the average time of analysis.

The vacuum tube is the most used X-ray source of radiation for XPS. Usually, vacuum tubes for XPS analysis mount more than one anode, in order to choose the emission wavelength among a few options in agreement to the requirements of Auger photoelectron spectroscopy or core level analysis of light elements. The radiation emitted from the vacuum tube needs to be monochromated, in order to screen the Bremsstrahlung radiation that contributes to the background and different spectral lines that will produce shifted peaks, reducing the readability of the spectrum. The most widely used spectral lines in XPS are Al Kα and Mg Kα. The monochromator, like in XRD, exploits the diffraction of the desired wavelength by a family of planes in a single crystal. The monochromatisation process also allows to focus the X-ray incident beam in a smaller spot size on the sample, making the technique more laterally resolved. A variation of the technique is the UV-photoelectron spectroscopy (UPS), that uses hard UV light for probe instead of X-rays. Less energetic radiation make the technique more sensitive to valence band characterisation and the probe is more easily focused in small spot sizes on the sample thanks to the availability of optics elements for UV radiation. The discussion of the technique goes beyond the scope of this work.

The electrons are emitted from the surface with random take-off angles; the role of the collection lens is to collect electrons with different trajectory and convey them into a parallel beam that reaches the analyser. The higher the acceptance angle, the higher the number of collected electrons normalised to the X-ray intensity, the higher the signal. Very high collection angles allow less intense beams to impinge on the sample surface, with consequent lower risk of degradation.

The hemispherical energy analyser receives electrons from a collection lens and demarcates them according to their kinetic energy, by inducing a spatial separation proportional to the kinetic energy.[66] The analyser is composed by two concentric hemispheres of radius R_1 and R_2 across which a potential is applied.

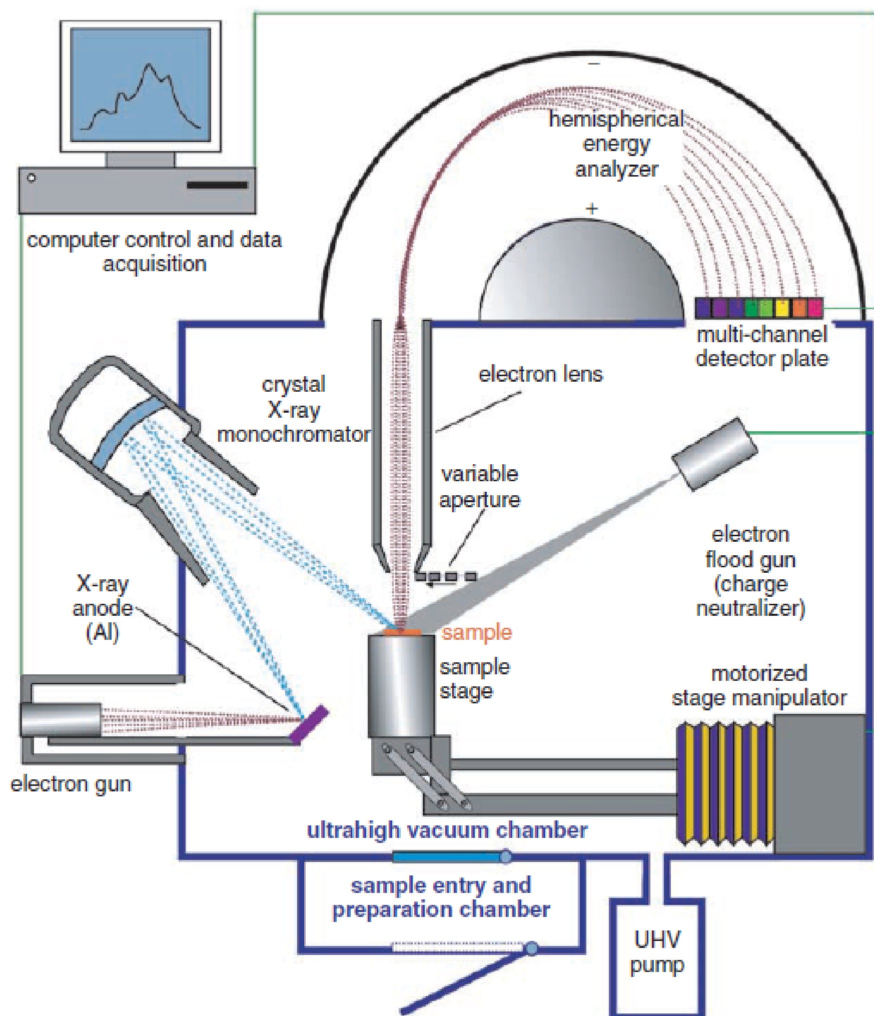

FIGURE 2.12: basic XPS lab-scale exparimental apparatus.

The electrostatic field between the hemispheres is therefore proportional to $1/R^2$, with $R_1 \leq R \leq R_2$; the potential in the centre radius $R_0 = (R_1 + R_2)/2$ is named V_0 and the potential energy associated to it is called pass energy of the analyser.

$$R_0 = \frac{R_1 + R_2}{2}; \qquad V(R_0) = V_0 \qquad E_0 = eV_0 \qquad \text{analyser pass energy.}$$

An electron characterised by a KE equal to the pass energy will describe a perfect circular trajectory and exit the analyser without deviation. Slower electrons will tend to be dragged towards the more positive potential $V(R_1)$, viceversa faster electrons will have higher inertia and will be less repelled by the more negative potential $V(R_2)$, resulting in a deviation towards the outer hemisphere. The interval of possible energy around E_0 that allow the electrons to pass the analyser depends on instrumental parameters, and it spans around ±5% of the pass energy in modern spectrometers.
Kinetic energy scanning can be achieved by changing the voltage across the hemispheric electrodes to tune the pass energy of the electrons without accelerating or decelerating them, or by keeping constant the pass energy and slowing the electrons quantitatively before they enter the analyser. The energy resolution ΔE is function of the fixed resolution of the analyser $\Delta E/E$, where E is the electron energy exiting from the hemispherical electrostatic lens; therefore, a constant pass energy is preferred to keep the same resolution along the spectrum. The higher the pass energy, the lower the ΔE therefore the better the energy resolution, with the drawback that the signal decreases. Typically, pass energies are of the order of 100÷200 eV for survey scans and down to 5÷25 eV for high resolution spectra.[67]
The aforementioned collecting lens system is therefore responsible for the binding energy scanning: the deceleration potential sweeps to achieve KE matching with the pass energy of the analyser. XPS spectra span from 0 eV to B.E of the order of magnitude of 1000 eV - 1400 eV depending on the anode, or even higher for synchrotron radiation.

The detector is placed after the aperture of the analyser, where electrons pass with a range of energies proportional to the underwent deflection. A rough solution is to allow a very small range and use a single-channel electron multiplier, with resolution equal to the energy range allowed to exit the analyser; the typical XPS detector is a multi-channel electron multiplier, which is sensitive to the coordinate of the impinging electron and therefore to the energy interval within the pass energy range.
Spatial imaging can be achieved by a combination of low acceptance angle lenses and 2D-arrays of electron detectors.

2.2.3 XPS spectral interpretation

The general information that can be achieved by the technique are:

- elemental identification (atomic concentration > 0.1%);
- chemical environment of the elements: oxidation state, covalent bonds...;
- unsaturation, conjugation or paramagnetism of chemical species;
- quantitative determination of the elemental surface composition;

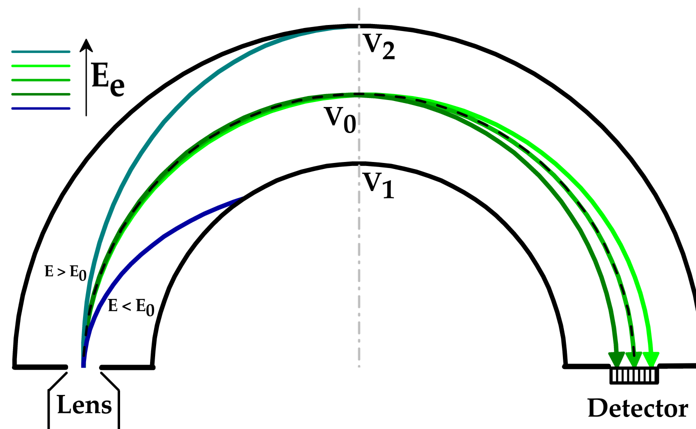

FIGURE 2.13: principle of working of the hemispheric electron analyser. In green, the electrons with $KE = E_0 = eV_0$ are not deviated by the electric field in the analyser; in darker and brighter green, electrons with $KE \approx E_0$ are deflected within the range of detection; in blue, an electron with $KE < E_0$ is dragged towards R_1 that is characterised by a more positive potential than the centre radius $V_1 > V_0$; in cyan, an electron with $KE > E_0$ is not deflected enough by the electric field and impinges on the more negative R_2 ($V_2 < V_0$).

- band gap of insulators;
- band alignment of thin films 2.2.4;
- composition depth profile;
- composition mapping.

The information can be derived by the peaks position, intensity, shape and special features like satellite peaks. Composition depth profile is obtained destructively by alternating XPS spectral acquisition and sputtering of the surface to reveal buried atomic layers.; non-destructive depth profiling is instead performed by angle resolved photelectron spectroscopy (ARPES): tilting the X-ray source from very low angles to larger one, the escape depth of the electrons changes. Composition mapping is obtained with surface sensitive detectors and movement of the sample stage; the lateral resolution required by the technique implies to have a collimated X-ray beam.

The XPS spectrum shows peak intensity in the form of count per second (cps) as function of binding energy referred to Fermi level (B.E.), plotted increasing from right to left to maintain the aspect of the detected spectrum, which is function of the kinetic energy of electrons. An example of XPS peak is shown in figure 2.14. The **position** of a peak along the spectrum is the indication of the transition to which it is associated. Qualitative elemental analysis is based on the assignment of spectral lines to specific element and transition; standard databases collect peaks positions of elements in the most common oxidation states.[68] Spin orbit interaction in atomic orbitals causes doublet splitting, that is reflected in a peak splitting for every transition of orbitals different from s. The entity of the peak splitting is also characteristic for element and transition.
Initial state effects strongly influence the peak position, therefore the peak is expected to show some shifting according to the initial overall charge of the

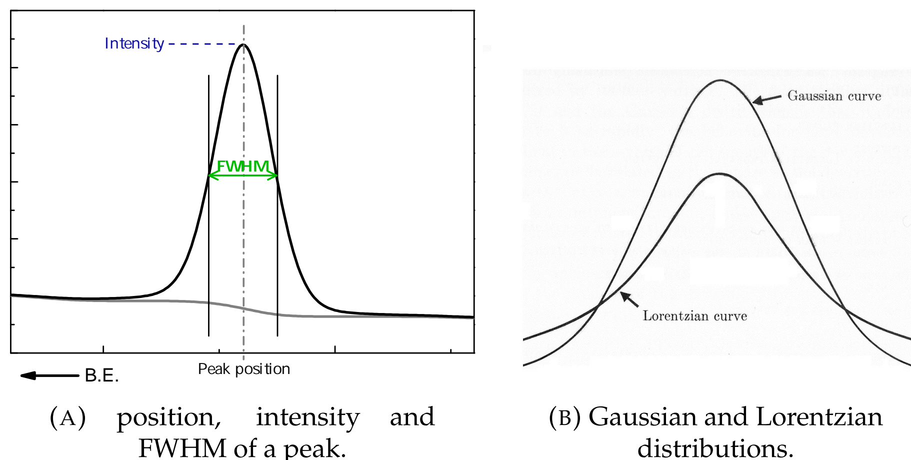

(A) position, intensity and FWHM of a peak.

(B) Gaussian and Lorentzian distributions.

FIGURE 2.14: peak parameters for qualitative and quantitative spectral interpretation.

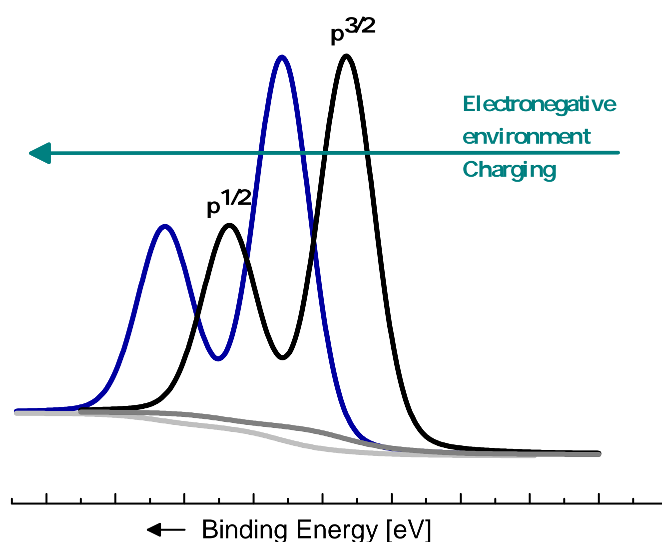

FIGURE 2.15: blueshift of a peak caused by an electronegative chemical environment, a positive oxidation state or positive electrostatic charging. The *p* orbital peak shows doublet splitting.

sample, the oxidation state of the element that produces the peak and the chemical environment of the latter. Covalent bonds with more electronegative atoms and positive oxidation states result in depletion of electrons around the atom or in direct positive charging, therefore a tighter binding of the electrons to the central positive potential and a lowering in energy of the electronic levels. Blueshift of the B.E. with respect to the pure element indicates an electronegative chemical surrounding and a positive oxidation state, as shown in figure 2.15.

Charging of the sample is usually present in semiconducting and insulating samples. Along the kinetic energy scanning, the photoelectrons emission leaves the sample progressively charged positively. Charge compensation can make an initial electrostatic charging stable during the analysis, instead of increasing; with the charging effect constant, the B.E. blueshift of the detected peaks is uniform along the spectrum and it can be evaluated by alignment of a peak position to a reference value known from literature.

The peak **intensity** is proportional to the probability of transition, which is proportional to the collisional cross-section, characteristic for element and orbital. Considering the total angular momentum quantum number $j = |l \pm s|$, the cross-section is always lower for $l - s$ than for $l + s$ therefore the peak at lower B.E. will always be more intense than the other; the theoretical intensity ratio of the peaks is fixed, since the transition probabilities differ just for the collisional cross-section. The **FWHM** of the peak is an indication of the energy dispersion of the transition; aside an intrinsic transition contribution related to the lifetime of the core holes, the peak broadening is related to the heterogeneity of chemical surrounding and of sample composition and to the instrumental contributions to the photoemission detection. The intrinsic peak shape is a Lorentzian curve while the instrumental contribution is a Gaussian. Final state effects are also influential in the FWHM broadening through secondary processes like electrons promotion to unoccupied levels, for example in Auger process or in paramagnetic/conjugated structures, that generate shake up satellite peaks and shake off tails (described elsewhere [67]). Non monochromatic sources are also a cause of appearance of satellite peaks, at equal distance from the main peak throughout the spectrum. The overall FWHM is the geometric average of the single contributions to the photoelectron emission and detection:

$$FWHM_{tot} = (FWHM^2_{intrinsic} + FWHM^2_{instrument} + FWHM_{charging} + ...)^{1/2} \tag{2.16}$$

Overlap of peaks significantly reduces the quality of spectral interpretation.

The **area** underneath the peak is calculated from the peak intensity, the FWHM and the Lorentian to Gaussian ratio of the curve. The area is proportional to the emitted photoelectrons associated to electronic transitions from various elements present in the system, through an intensity factor that depends on chemical nature of the analyte and on instrumental parameters. Assuming to know the proportionality factor between area and photoemitted electrons, the percentage of each element detected along the specrtum can be determined.

$$I_{ij} = KT(KE)L_{ij}(\gamma)\sigma_{ij} \int n_i(z) e^{\frac{-z}{\lambda(KE) cos\theta dz}}, \qquad \text{solved for } n_i \tag{2.17}$$

where I_{ij} is the area of the peak of $i \rightarrow j$ transition, K an instrumental constant, $T(KE)$ the transmission function of the analiser, L_{ij} is the angular asymmetry of the orbital involved in the atom of element i, $n_i(z)$ is the concentration of element i at distance z from the surface, and the exponential term is the absorption according to Beer's law, as exposed previously in this section (42). Solving $n_i(z)$ for each element visible in the spectrum, the abundance of the element in the sampling depth referring to the spot size of the sample is:

$$\%n_i = \left(\frac{n_i}{\sum n_i}\right) \cdot 100 \tag{2.18}$$

expressed in atomic percentage. The dependance of n_i to the sampling depth can be neglected under the assumption of homogeneous composition of the sample

through its cross-section.
The inelastic scattering of electrons contributes to the **background** of the spectrum at higher B.E. with respect to the peak, because electrons lose kinetic energy from inelastic collisions and the B.E. results fictitiously higher. Shirley background is modelled on the presence of a tail that develops in higher B.E., with onset at the centre peak. In materials characterised by a band gap, the minimum of energy the photoemitted electron can give to another electron in an inelastic collision is equal to the band gap, for lower energies would promote the electron from the valence band to the forbidden energy interval. Therefore, the onset of the tail is no longer at the B.E. corresponding to the peak maximum but blueshifted from it of an energy range equal to the band gap. The latter spectral feature can be exploited to determine the band gap of semiconductors and dielectrics, according to the method described in section 2.2.4. It is called electron energy loss spectroscopy (EELS), not to be confused with the electron microscopy analysis that bears the same acronym.

2.2.4 Determination of Band Alignment

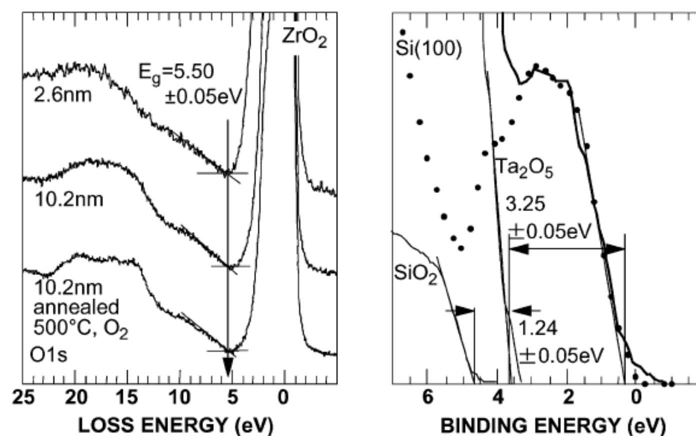

FIGURE 2.16: Band alignment determination by Miyazaki method. On the left, the energy gap by interpolation of the electron energy loss peak at higher B.E. with respect to the peak centre; on the right, the evaluation of VBO from the onset difference in valence band region of the thin film sample. It is to notice the presence of two onsets because the interface between the material lies within the electrons escape depth.[69]

Let consider two materials that share an interface for which it is important to evaluate the electronic band diagram, namely an oxide layer grown or deposited on a semiconductor.
The band alignment of the two materials can be described knowing:

- the band gap of the oxide;
- the band gap of the semiconductor;
- the misalignment between the two valence bands (valence band offset, VBO) or conduction bands (conduction band offset, CBO).

All the information can be derived by XPS analysis according to the study carried by Miyazaki.[69]
In the study, the band gap of the materials is evaluated from the shifted onset of the electron loss peak at higher B.E. from the peak, as mentioned in the previous paragraph. A generic peak of the oxides is fitted, choosing a high intensity factor to minimise the errors caused by noise or low intensity of the peak; the electron loss peak is present at higher B.E. and it is interpolated by linear regression; the average background intensity at the base of the peak on the high energy side is considered the background before any the EELS onset; the intercept of the two sets the actual onset of energy dispersion by inelastic collisions. The energy gap is therefore:

$$E_{gap} = E_{EELSonset} - E_{peakmax} \tag{2.19}$$

The valence band offset is instead measured when a sample contains the interface within the escape depth of the electrons, in order to obtain a relevant signal from both the phases. The valence band contribution at the rightmost of the spectrum (very low B.E.) will show two onsets for the presence of two different energy minima of electron excitation. The onset of each valence band (VB) is again the intersection between the background and the linear interpolation of the peak, with background ≈ 0 with good approximation since any inelastic scattering forbids the electron photoemission from the surface. The valence band offset is given by the difference of the two valence band onsets:

$$E_{VBO} = E_{VB_{highenergy}} - E_{VB_{lowenergy}} \tag{2.20}$$

Examples of band gap and VBO determination is shown in figure 2.16.

2.3 Two-point probe method for the electrical characterisation of semiconductors, dielectrics and devices

Electrical behaviour characterisation of semiconductor devices is a field of extreme importance in research and industry. Techniques established with the first appearance of devices are nowadays under constant development and refining. Several methods have been developed in function of the parameters and devices to test.[70]
Two-point probe method working principle is to contact, permanently or temporarily, two small areas of the material and impress an electric probe across the points; current or voltage, continuous or alternated are used as probe. The response of the dual electrical observable is measured and elaborated to obtain the parameter of interest knowing the equivalent circuit of the experimental apparatus, which depends on the instrument and the sample.

MOS capacitors are a representative for the electrical behaviour of devices that show an electrode/dielectric/semiconductor interface across which a voltage is applied, as exposed in chapter 2 (section 1.5).

The electrical features that can be measured in a MOS capacitor by the application of a gate voltage with a two-point probe method are:

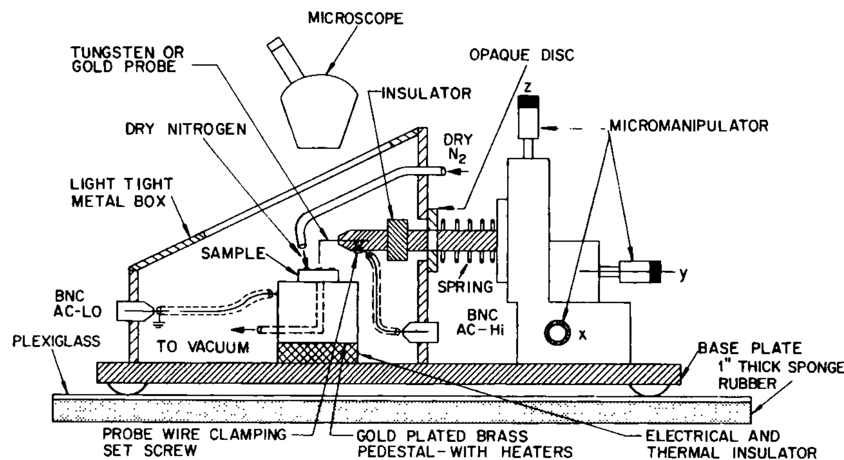

FIGURE 2.17: example of a probe station for current-voltage, capacitance-voltage and conductance-voltage measurements of SiO_2/Si MOS capacitors arrays.

- **current** through the dielectric, measuring it in response of a continuous voltage (I-V);
- **differential capacitance** of the MOS capacitor, measuring the capacitive part of the admittance in response of a mixed continuous-alternated voltage at different frequencies of alternation in small signal range (C-V);
- **admittance (conductance)** in response to the mixed AC-DC voltage at different frequencies of alternation in small signal range (G-V).[55]

In the present work, particular attention is focused on the reply of the staggered band alignment on breakdown strength of the MOS capacitors; another important feature of the dielectric characterisation performed in this work is the evaluation of the relative permittivity (dielectric constant) κ. Doping concentration and profiling, trapping mechanisms at the interface and in the bulk dielectric, trap densities and type, work functions, carrier mobility and free carrier lifetime and the effect of internal photoemission can be evaluated with the same analytical techniques: their investigation was not mastered in electrical measurements on high-κ Rare Earth Oxide/III-V Nitride systems, but they constitute an interesting outline for future work (**??** on page ?? *Note: in the conclusions*.) The experimental apparatus varies according to the measurement requirements.

2.3.1 Current-Voltage (IV) measurements of MOS capacitors

The basic experimental setup for I-V measurements is:

- a **probe station** equipped with a microscope to connect the MOS capacitors, where the **sample** is connected and protected from the environment if necessary;
- a **linear voltage ramp generator** that constitutes the source of DC voltage;
- an **amperometer** for I-V measures;

An example of probe station is shown in figure 2.17.[55]

Breakdown happening is visible on I-V plots by the sudden increase of the current flowing through the oxide, that implies the opening of a channel of conduction of larger entity with respect to minor leakages that are be recorded in the measure before breakdown, where the current can be approximated to ≈ 0 A/cm^2. Breakdown is a stochastic process related to defects and local field magnitude, therefore multiple measures are required to obtain accurate results.

To normalise the breakdown strength to the oxide thickness, the current density is plotted as function of the electric field in the oxide:

$$\mathcal{E}_{ox} = \frac{V_{gate}}{t_{ox}} \tag{2.21}$$

and therefore $V_{gate}^{BD} \Rightarrow \mathcal{E}_{ox}^{BD}$.

2.3.2 Capacitance-Voltage (CV) measurements of MOS capacitors

Differential capacitance is necessary to evaluate the oxide's capacitance C_{ox}. As defined in 1.5 on page 24, differential capacitance is C $\equiv$ $^{dQ_{tot}}/_{dV_{gate}}$; to evaluate capacitance variations, it's necessary to have an alternate voltage contribution to the electric probe.
The alternate voltage applied to the capacitor must be in the small signal range, for the response of the alternate current must be linear with the alternate voltage (page 24); and the frequency must be low ($f \leq$ 1MHz), because at high frequencies the minority carriers don't respond fast enough to the voltage variation to maintain equilibrium in the capacitor, therefore the steady state assumption fails.

The main components of the experimental apparatus are:

- a **probe station**, equipped with a microscope to connect the MOS capacitors, where the sample is connected and protected from the environment if necessary;
- a **linear voltage ramp generator** that features the possibility to superimpose an alternated voltage with tunable frequency to the DC voltage sweeping value, in order to perform admittance measurements: the signal provided to the sample must be similar to the one shown in figure 1.16 on page 24;
- a **lock-in amplifier** that measures simultaneously capacitance and conductance contributions to the admittance. Alternatively an admittance bridge can be used, more accurate but slower.

The lock-in amplifier measures the capacitance and the conductance part of the admittance simultaneously by separation of the real component (in phase with the probe) from the imaginary component (quarter phase with the probe):

$$i_{90} = \omega \eta v_R C_m; \qquad i_0 = \eta v_R G_m \tag{2.22}$$

where i_0 and i_{90} are the in phase and quarter phase admittance components, C_m is the admittance capacitance, G_m is the parallel conductance, ω is the frequency of the superimposed AC voltage and v_R is the average mean square root voltage

applied to the system (constituted mainly by the DC voltage for the small signal hypothesis). Therefore the measured quantities are:

$$C_m = \frac{v_1 S}{\omega \eta v_R}; \qquad G_m = \frac{v_2 S}{\eta v_R} \tag{2.23}$$

where v_1 is the 90° component of the input voltage, v_2 is the 0° component of the input voltage, and S/η is a parameter related to the instrument.

Oxide relative permittivity evaluation

The relative permittivity, also called dielectric constant, of the high-κ oxide is important to determine if it is suitable for replacement of SiO_2 for the gate dielectric.

The capacitance equivalent thickness (CET) is the thickness that SiO_2 would equal in order to achieve the capacitance measured in the MOS capacitor with the high-κ oxide:

$$CET = \frac{\epsilon_0 \kappa_{SiO_2} A}{C_a} \tag{2.24}$$

where ϵ_0 is the permittivity in vacuum, κ_{SiO_2} is the relative permittivity of SiO_2 and C_a is the capacitance in accumulation of the high-κ oxide measured on the MOS capacitor of area A, approximately the capacitnce of the oxide $C_o x$ (section 1.5).
The CET can be expressed as a linear equation [55][3]:

$$CET = \frac{\kappa_{SiO_2}}{\kappa_{high-\kappa}} \cdot d_{high-\kappa} + CET_{InterLayer} \tag{2.25}$$

where κ_{SiO_2} and $\kappa_{high-\kappa}$ are the relative permittivities of silica and high-κ oxide, $d_{high-\kappa}$ is the high-κ oxide thickness and $CET_{InterLayer}$ is the additional equivalent thickness provided by an interfacial layer of different oxide, if present (which is often the case for Si wafers with high-κ oxides deposited). With a κ_{SiO_2} of $\approx$ 3.9, the silica equivalent thickness would reach sub-nanometric values for very high-κ modern dielectrics: too low to show an acceptable level of leakages if installed in the system in place of the high-κ dielectric, as mentioned in chapter 1.3. Considering that the high barrier felt by the semiconductor carriers close to the dielectric interface induce the lowering of the wavefunction intensity of the carriers to almost negligible values, the CET of silicon is lowered by a fixed quantum mechanical contribution of 4Å to take into account the effect. The resulting quantity is called equivalent oxide thickness (EOT):

$$EOT = CET - 4\text{Å} \tag{2.26}$$

Therefore the dielectric constant of the high-κ oxide can be evaluated from the accumulation capacitance in C-V measurements through equations 2.24 and 2.25, knowing the accumulation capacitance, the area of the MOS capacitor, the thickness of the oxide, and the dielectric constant of SiO_2. Measuring samples of progressive oxide thickness it is possible to derive the angular coefficient of the

linear interpolation of $CET(d_{ox})$ and therefore $\kappa_{high-\kappa}$ without knowing the CET of interlayers if present.

An alternative method for ultra-thin gate oxide was developed by Kar, S. in order to decorrelate the measure from the thickness variation and the quantum effects.[71] The assumptions made in deriving the plots for the κ extraction are that both the space charge and the interface trap capacitances are exponential functions of the surface potential, in accumulation regime, with an exponential coefficient β.
The capacitance of the MOS capacitor at a frequency that allows a steady state (cfr. 2.3.2 on page 54) is defined as C, and it is the contribution of the dielectric capacitance in series with the contribution of interface capacitances, that depend on the surface potential through a known exponential expression.

$$\frac{1}{C} = \frac{1}{C_{ox}} + \frac{1}{C_{interface}}, \qquad C_{interface} \propto e^{\beta\phi_s} \tag{2.27}$$

where ϕ_s is the surface potential, β an exponential factor and $C_{interface}$ the contribution that causes deviation from the CET evaluation in ultrathin dielectrics. Deriving C as function of the surface potential and differentiating, the result is a linear equation where the intercept with the y axis yields the actual gate dielectric capacitance, without assuming $C_a \approx C_{ox}$:

$$\frac{1}{C}\left(\frac{dC}{dV}\right)^{1/2} = \frac{\beta^{1/2}}{C_{ox}} \cdot (C_{ox} - C) \tag{2.28}$$

therefore plotting $\frac{1}{C}\left(\frac{dC}{dV}\right)^(1/2)$ as function of C, a linear trend is obtained with $-\frac{\beta^{1/2}}{C_{ox}}$ as slope and $\beta^{1/2}$ intercept with the y axis; therefore, C_{ox} is given by:

$$C_{ox} = -\frac{intercept}{slope} \qquad \text{of the Kar plot.} \tag{2.29}$$

From the value of C_ox, it is possible to compute the relative permittivity of the oxide by the relation:

$$\kappa_{high-\kappa} = \frac{C_{ox} t_{ox}}{\epsilon_0 A} \tag{2.30}$$

definition of κ, from which also the definition of CET derives.

Chapter 3

Materials and Methods

This chapter covers the procedures to characterise the rare earth oxide/III-V nitride systems, according to the experimental techniques described in chapter 2. The structure is characterised making use of diffractographic techniques; electronic band alignment by x-ray photoelectron spectroscopy; electrical behaviour, testing current and capacitance response to the application of a bias. The oxide-semiconductor interface stack and quality are investigated by means of transmission electron microscopy. All the characterisations were carried out at the Technion, Israel Institute of Technology.

3.1 Metal/Oxide/Semiconductor systems: sample stacks

The main system analysed in this work is the oxide-semiconductor stack:

crystalline GSO/GaN/Si(111)

where GSO is $GdScO_3$ oxide dielectric, GaN is the semiconductor, and Si(111) is the structural support wafer, because bulk III-V nitrides wafers cannot be successfully achieved as reported in section 1.4.1.
The samples were produced externally in Forschungzentrum Jülich. GaN is grown by molecular beam epitaxy (MBE) onto the substrate wafer, up to a thickness of 1000 nm. Once the semiconductor is grown, the surface is cleaned and GSO is deposited on the surface by means of pulsed laser deposition (PLD). This allows the growth of either a crystalline (epitaxial) or an amorphous oxide, and different thickness can be reached according to the time of deposition: in particular, $\approx$ 4 nm and $\approx$ 30 nm are grown, respectively called "thin film" and "thick film" sample, according to the requirements that different analytical techniques demand.
A strain engineered buffer layer between the support wafer and the semiconductor is necessary to absorb the lattice mismatches, so to limit the dislocation density in GaN. More details on the sample design and preparation are explained in Appendix A, while the final stack of crystalline GSO-GaN/Si(111) is shown in figure 3.1, presenting the cases of thick and thin film oxide.

In order to evaluate the influence of each component in the MOS gate behaviour, different materials were substituted in the stack with respect to the original crystalline GSO-GaN/Si(111) system. System variations are produced as follows:

- oxide crystallinity: amorphous GSO deposited in place of crystalline GSO;
- oxide type: $LuLaO_3$ (LLO) was deposited in place of GSO;

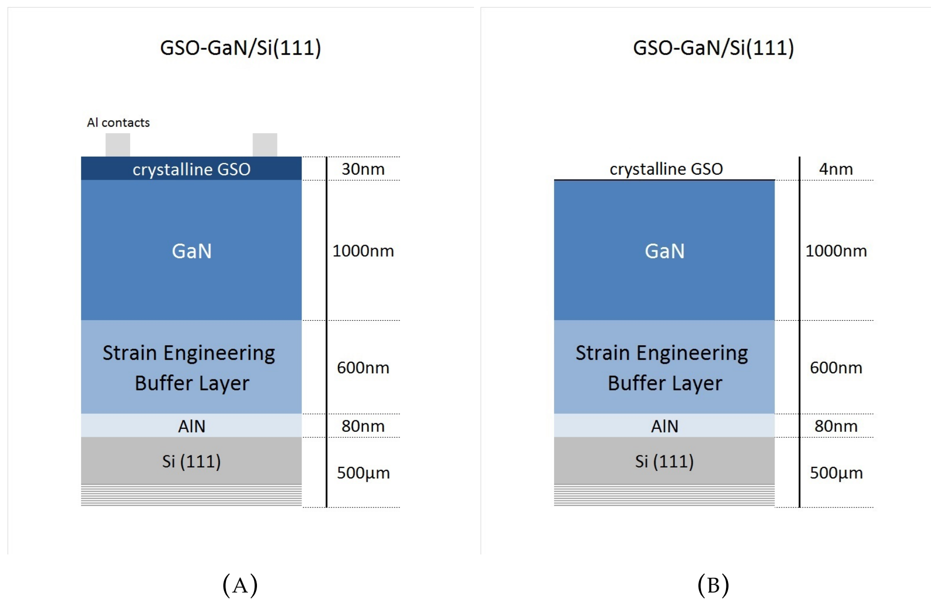

(A) (B)

FIGURE 3.1: stack of crystalline GSO-GaN/Si(111): (a) shows the thick film oxide and (b) the thin film oxide, which are the same system used for different analytical techniques.

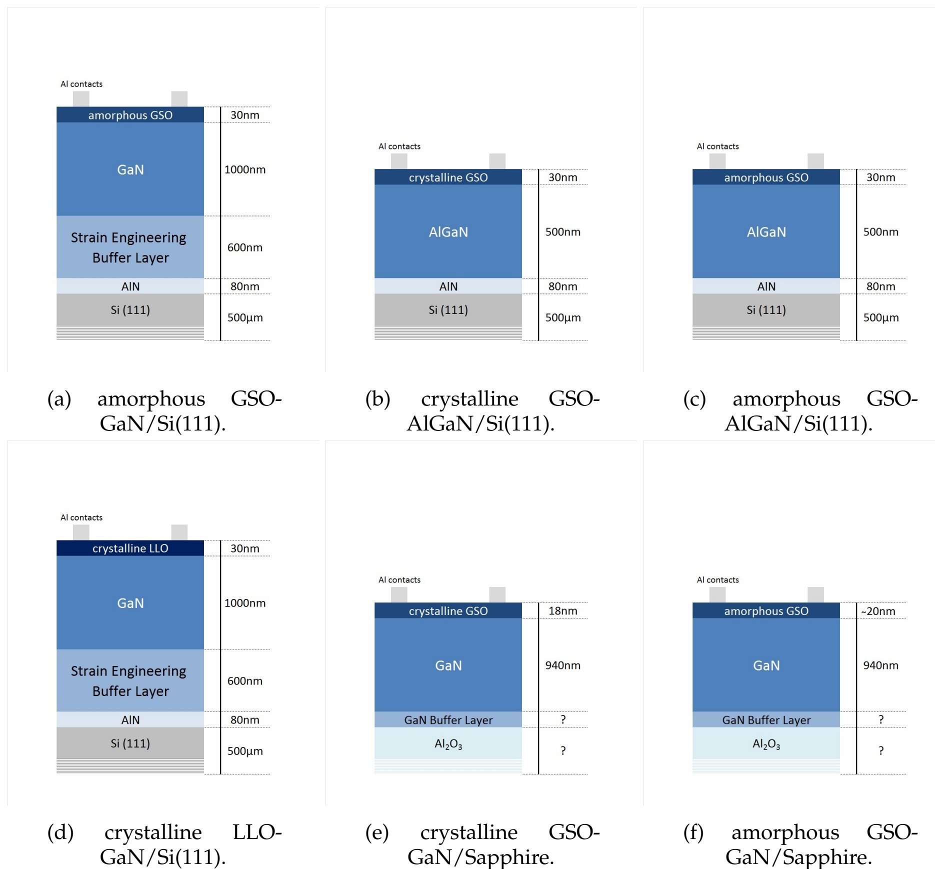

(a) amorphous GSO-GaN/Si(111).
(b) crystalline GSO-AlGaN/Si(111).
(c) amorphous GSO-AlGaN/Si(111).
(d) crystalline LLO-GaN/Si(111).
(e) crystalline GSO-GaN/Sapphire.
(f) amorphous GSO-GaN/Sapphire.

FIGURE 3.2: thick film oxide stacks of the systems under analysis, which differ from crystalline GSO-GaN/Si(111).

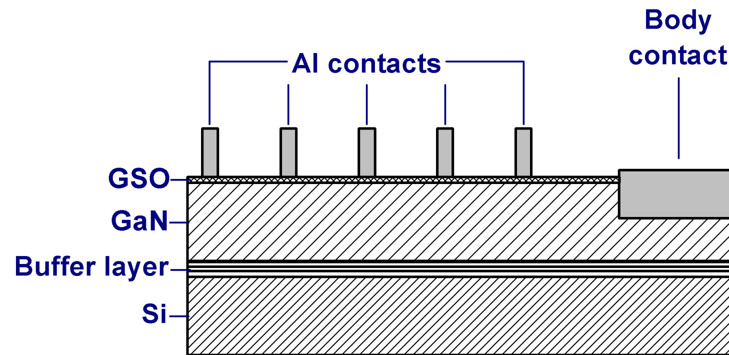

FIGURE 3.3: cross section of thick film samples. Example: GSO-GaN/Si(111)

- III-V nitride composition: $Al_{0.5}Ga_{0.5}N$ was used as semiconductor (from here on simply referred to AlGaN) instead of stoichiometric GaN;
- support wafer type: Sapphire wafers were used as base for GaN MBE deposition instead of Si(111) wafers.

For each case, both the $\approx$ 4 nm and $\approx$ 30 nm are produced: the thick film samples are shown in figure 3.2. Al contacts and substrate (body) contact are deposited thermally on top of the thick oxide film samples with a thickness of $\approx$ 100 nm, giving a typical sample cross section as shown in figure 3.3.

3.2 Structural characterisation of the systems

3.2.1 X-ray diffractography characterisation of semiconductors and epitaxial oxides

The PLD deposited oxide can be grown epitaxially on the semiconductor, which is a wurtzite structure in both the cases of GaN and AlGaN. Therefore, XRD investigations are performed in order to characterise the GSO and LLO cell parameters as explained in section 2.1.
The X-Ray diffractometer used for the characterisation is a Rigaku Smartlab, using the following experimental setup:

Source Cu K$\bar{\alpha}$ (λ = 0.15418 nm) and Kβ_1 (λ = 1.39225 nm) wavelengths, rotating anode, 90÷100 mA output current;

Monochromators absence of monochromator or Ge((220)x2) monocrystal, plus divergence slits for parallel beam (PB) radiation (open or 5.0°);

Stage eulerian cradle with three rotational degrees of freedom (azimuthal rotation ϕ and tilting χ);

Detector Scintillation counter NaI plus preamplifier and photomultiplier, after scattering slits and Ge((220)x2) receiving optics; mobility of the holder

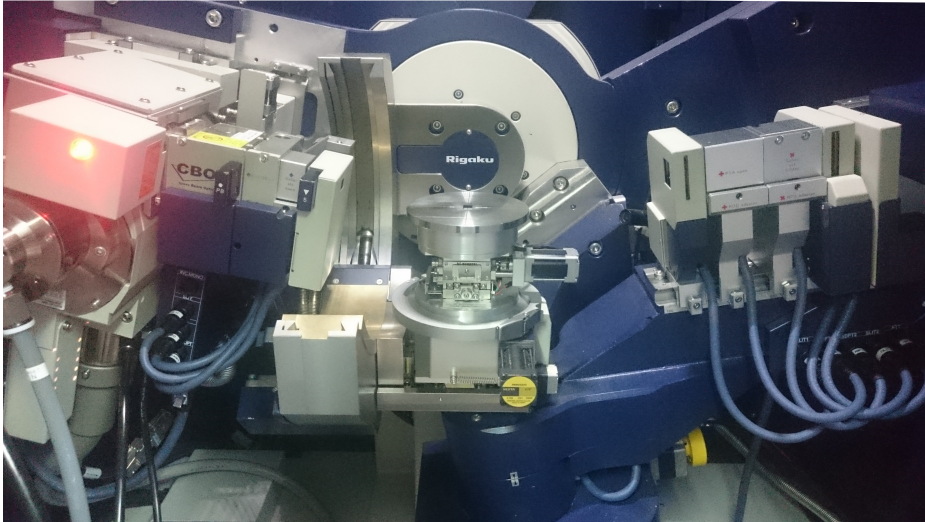

FIGURE 3.4: picture of the working XRD during a θ-2θ analysis from behind the protective screen. In the centre of the picture, the stage is visible with the sample on top; for this analysis, the stage is not tilted. On the left side, the source of the radiation, the monochromator and the 5.0deg slit; on the right side, the receiving optics and detector components.

allows the detection signal from angles lying on the *xz* and *xy* planes (figure 2.4 on page 34).

The XRD components are shown in picture 3.4.
All the XRD investigations are conducted on the thick film samples (≈30 nm oxide). θ-2θ scans between 25° and 45° on the crystalline oxide samples provide the out of plane cell parameters of both the semiconductor and the oxide; the blank θ-2θ spectrum is acquired from bare nitride/support samples. A θ-2θ analysis of amorphous GSO-GaN/Si(111) is performed in order to check if the oxide underwent some crystallisation. All the θ-2θ scans are executed with an angle step of 0.01°. The Bravais lattice of the oxide is in principle unknown, though it's expected to be hexagonal because of epitaxial growth: pole figures investigations (described in 2.1.3 on page 39) at the θ-2θ outcoming reflections are done to verify the crystallographic group of the oxide. A complete pole figure (PF) is obtained tilting the sample of χ between 0° and 90° with steps of 1°, scanning ϕ between 0° and 360° for each tilting angle with fixed θ-2θ. The scanning ϕ speed spanned between 45°/min and 90°/min. PF of crystalline GSO-GaN/Si(111) and crystalline LLO-GaN/Si(111) are acquired at 31°, 35° and 29°, 35° respectively.
The in-plane lattice parameter of the oxide is investigated first via XRD in-plane measurements scanning 2θχ between 25° and 40°, moving the detector branch and rotating the stage by ϕ along with 2θχ to maintain the symmetric in-plane scan, all imposing a 2θ of 0.2°; then via tilted sample θ-2θ scan to detect the d-spacing of the hexagonal lattice (101) planes and, subsequently, calculate the in-plane cell parameter knowing the out-of-plane from θ-2θ spectra. An initial χ tilting angle hypothesis was necessary as no hexagonal GSO and LLO were reported as bulk stable phases in literature, hence the lack of backdata. χ for the oxides was in principle estimated by assuming that a/c is the same in the oxide and in the semiconductor, being the latter known, and then corrected with the first *a* detected value. GaN and GSO crystal quality were evaluated for crystalline GSO-GaN/Si(111) and crystalline GSO-GaN/Sapphire by means of rocking curve

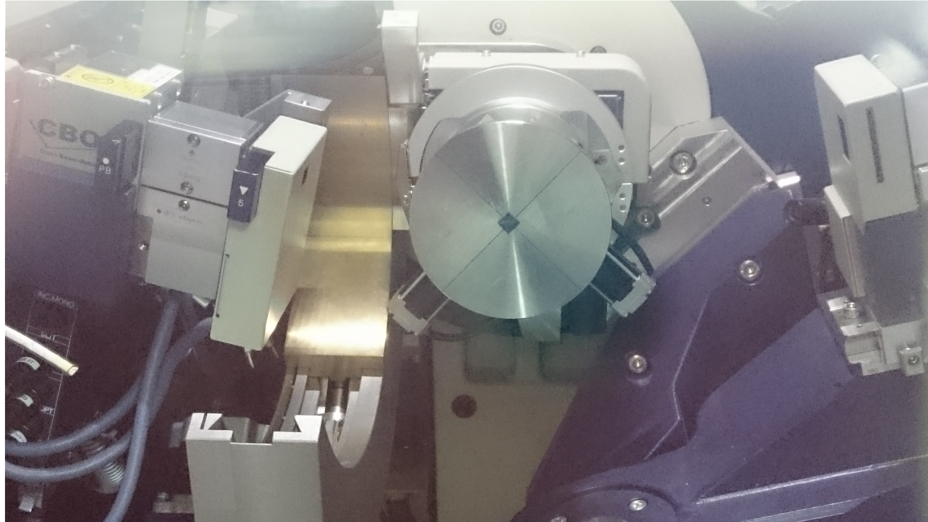

FIGURE 3.5: tilted stage in a pole figure analysis.

measurements, both moving ω around the (002) peaks centre of GaN and GSO, whose positions were picked from θ-2θ measures in order to design the experiment. The aim of rocking curve measurements is to understand the quality of GaN grown on the respective support wafers, because defects and dislocations can propagate from GaN to the epitaxial oxide grown on it affecting the electrical performances. Finally, X-ray reflectivity measurements were performed on all the thick film samples (including the amorphous) to evaluate the effective oxide thickness. The reflection signal was acquired between 0.2° and 6.0°; thickness can be evaluated by spectral fitting or Fourier transform (FT) of the spectrum, as explained in 2.1.3. In the case of crystalline films, thickness was evaluated by spectral fitting generally executed between 1° and 4°; FT of the spectrum was used in the case of amorphous samples because of the poor quality of the fitting.
All the analyses here discussed are performed in high resolution making use of Ge(220) two-bounce monochromator, except the pole figures which are non-monochromated in order to achieve the signal maximisation from the oxide layer.

3.2.2 Transmission electron microscopy imaging of oxide-semiconductor interface

Transmission electron microscopy Bright Field images were acquired with Tecnai G^2 20 S-Twin TEM instrument, with the following experimental apparatus:

Source W filament, tension 20 kV÷200kV;

Magnification 25x÷1030kx;

Point Resolution 0.24 nm;

Detector CCD camera.

The cross sectional samples were produced externally by ion milling from the thick film samples of crystalline GSO-GaN/Si(111), crystalline GSO-AlGaN/Si(111) and crystalline GSO-GaN/Sapphire at sub-lattice parameter lateral resolution.

3.3 X-ray photoelectron spectroscopy and band alignment on thin oxide film samples

X-ray photoelectron spectroscopy (XPS) is a very superficial technique because the escape depth of the photoelectrons in the material is very small, as discussed in 2.2.1. Therefore, the thin film samples are analysed with this technique: $\approx$4 nm of oxide thickness allow to obtain signal from the III-V nitride underneath. The instrument used is a Thermo VG Scientific Sigma Probe with the following experimental setup:

Source monochromated Al Kα, $h\nu$ = 1486.6 eV;

Chamber magnetic shielded (μ-metal), kept in UHV regime for the entire analysis;

Collector high angular acceptance electrostatic lens (20° $\div$ 80° relative to the sample normal), imposed pass energy 50eV;

Detector energy and angular multi-channel 180° spherical analyser.

For each sample, a survey scan from 1300.00 eV to 0.00 eV of binding energy was acquired, in steps of 1.00 eV. Subsequently, a high resolution scan, reducing the step to 0.05 eV, was run for the following peaks: Ga*3p*, N*1s*, O*1s*, Gd*4s*, Sc$3p^{3/2}$; the latter two not present in LLO-GaN/Si(111). The choice of each element's peak was influenced by the relative intensity of the signal, derived from literature, and avoiding the overlap of other elements' contributions in order to have a better readability. The valence band spectrum and the O*1s* electron energy loss, for band alignment calculation purposes, were evaluated with the same resolution.
Spectral fitting was done exclusively on the high resolution peaks by means of the software XPSpeak4.1, imposing a Lorentzian to Gaussian ratio of 15% and Shirley background; the valence bands and EELS of O*1s* onsets are interpolated by linear regression.
The absence of an electron flood gun, that balances the positive charging effect of the photoelectrons emission, results in a blueshift of the entire spectrum of around 5-6 eV for the Si(111) supported samples, constant along the whole spectrum. This allows a charge removal from the plotted spectrum, consisting of aligning Ga*3p* peak to 105.1 eV, value found in literature for Ga*3p* in GaN[72][73]. The insulating nature of Al_2O_3 required the samples grown on sapphire wafer to be grounded to the stage, making use of silver paste on the sides, in order to achieve a limited charging.

3.4 Electrical measurements

3.4.1 Current-Voltage measurements

All the electrical measurements were conducted on the thick film samples to minimise the fluctuations in breakdown and capacitance related to defective paths across the oxide, which produce leakages. The experimental setup consists of a voltammeter, namely Agilent 4155C Semiconductor Parameter Analyser, connected to the sample with a 2 points probe. The stage is mounted on a *xy*

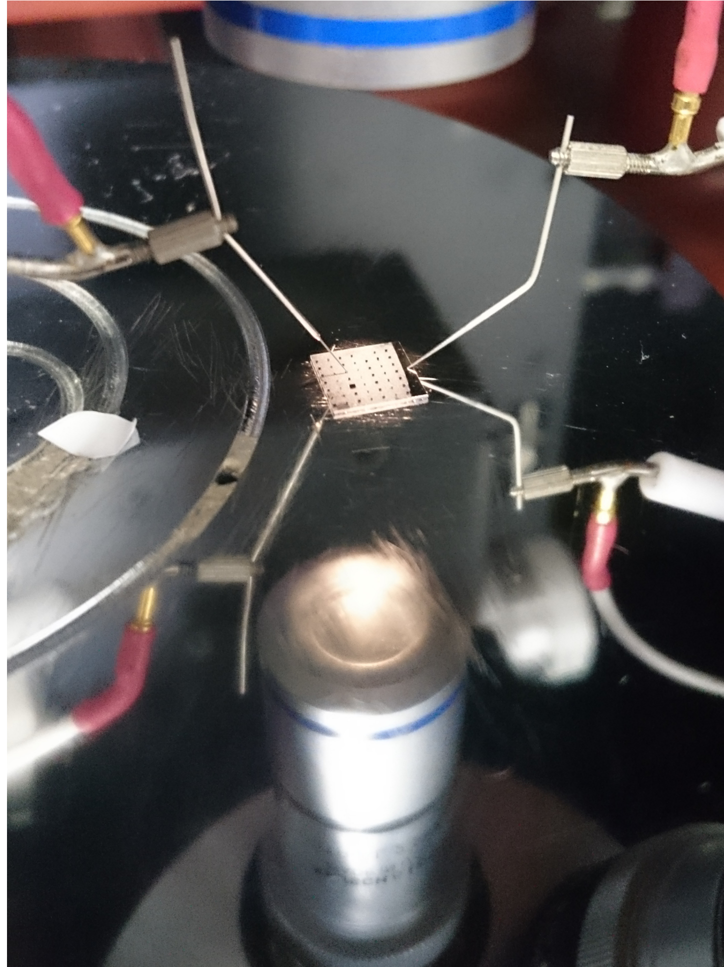

FIGURE 3.6: picture of the two-contact probe for I-V and C-V measurements on crystalline GSO-GaN/Sapphire. The optical microscope, that allows the achievement of a proper contact, is reflected on the chuck.

manipulator and an optical microscope (5x to 50x) allows the controlled positioning of the probe on a determined Al contact (that consists of a MOScap with the oxide-semiconductor underneath, as described in 1.5 on page 19). A photo of the contacts is shown in figure 3.6.

The base contact is grounded; a DC linear sweep voltage is applied to the MOScap from 0 to +30V, within which limit the breakdown (BD) statistically occurred, or -40V, representing the instrumental limit. The same MOScap is never used for both forward and reverse bias application. The voltage steps that determine the measure resolution were limited by the maximum number of attainable data in a single measure; therefore, the step was set for 30mV in forward and 40mV in reverse bias application. The current limit was set to 10mA, value that can therefore be detected along with the occurrence of breakdown, to preserve the integrity of system and instrument.

3.4.2 Capacitance-Voltage measurements

The same experimental apparatus described for I-V measurements is used to perform C-V measurements. The voltammeter was changed to Agilent 4824A,

that allows low amplitude AC superposition to DC voltage. The bias on a single capacitor was typically swept between -3.5 V and +3.5 V, with range fluctuations optimised on the system's response, and multi-frequency testing between 1 kHz and 1 MHz with 3 measures per frequency decade. 50mV of step was a condition imposed to all C-V measurements.
Hysteresis curves were also acquired on the same voltage interval of the C-V single measurement, performing only one loop per frequency between 1 kHz and 1 MHz, 2 measures per frequency decade, 50mV step for the measurement resolution.

Chapter 4

Results and Discussion

This chapter shows and discusses the results of the rare earth oxide/III-V nitride characterisation, performed according to the procedures discussed in chapter 3. The crystalline oxides grown on hexagonal III-V nitrides are epitaxial relaxed, with in-plane cell parameter larger than the one found for the nitride. The oxide-semiconductor band alignment derived from XPS measurements results staggered, with high valence band offset and no potential barrier in the conduction band for electrons flowing from semiconductor to oxide. This condition finds correspondence in an asymmetrical electrical behaviour, with breakdown occurring at much lower voltages in forward bias than in reverse bias. TEM imaging shows the presence of an interface, two atoms thick layer between oxide and semiconductor in GSO-GaN systems. The overall influence of the interface layer and of defects on the performances is finally discussed.

4.1 Crystal structure of the oxides on III-V nitrides studied by XRD

4.1.1 Crystalline structure of epitaxial rare earth oxides

GaN is known to be a wurtzite structure, an hexagonal crystal composed by two HCP sublattices of anions and cations. Free-standing GSO and LLO are monoclinic crystals, but epitaxy on wurtzite induces the growth in a hexagonal lattice, unless crystalline rearrangement takes place. Pole figures (PF) are acquired for GSO-GaN/Si(111) and LLO-GaN/Si(111) at the angles provided by the first θ-2θ survey scan, as mentioned in chapter 3, to investigate the crystal structure of the oxide. A ϕ scan is acquired for the sample tilted of an angle χ, for every χ varying between 0° (surface parallel to the ground) and 90° (surface perpendicular to the ground); for χ = 0°, which corresponds to the pole of the PF and the center of the circle in the PF projection, the high intensity peak of the θ-2θ reflection of GaN(002) or GSO(002)/LLO(002) is visible, depending on the 2θ angle of detection. The other reflections visible along the pole provide information on the point symmetry group of the layer, depending on how many times the reflection is repeated along one circular crown, and on the ratio between the out of plane and other lattice parameters according to the Bravais lattice the crystal belongs to.
In the PF of GSO-GaN/Si(111) and LLO-GaN/Si(111), the reflections seen at LLO(002) 2θ detection angle are compared to the ones acquired at GaN(002) 2θ in figure 4.1. Analogous results are obtained for GSO-GaN/Si(111).

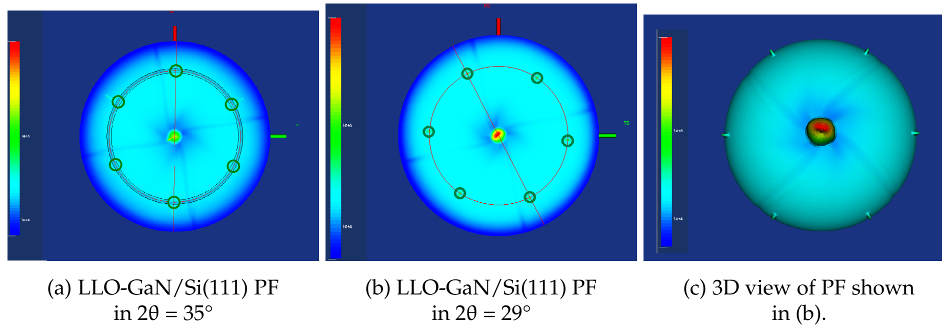

(a) LLO-GaN/Si(111) PF in 2θ = 35°

(b) LLO-GaN/Si(111) PF in 2θ = 29°

(c) 3D view of PF shown in (b).

FIGURE 4.1: (a),(b) pole figures projections of the measurements on LLO(002) and GaN(002) reflection angles, with highlight at tilting angle χ=62°. (c) 3D construction of PF in (b).

The film shows six-fold symmetry typical of hexagonal systems; the oxide and GaN peaks are placed at the same azimuthal angle ϕ, that means that they are characterised by the same in-plane orientation of (00l) crystallographic planes. Therefore, we can deduce that both GSO and LLO films are epitaxial on GaN; nonetheless, the tilting angle χ is slightly different, meaning the $^{a}/_{c}$ of the two phases is not exactly the same. Depending on the oxide c value, the epitaxial layer may be strained or relaxed. The in-plane cell parameter is hence investigated (section 4.1.2 on page 69) to understand this aspect of the epitaxial growth.

4.1.2 Hexagonal cell parameters

Given that both oxide and semiconductor are hexagonal crystals, reflections in θ-2θ spectra come from the (00l) plane reflections for GSO, LLO, GaN and AlGaN; the substrate wafers can contribute with peaks from Si(111) and Al_2O_3(222). Figure 4.2 shows θ-2θ spectrum of crystalline and amorphous GSO-GaN/Si(111) in relation to the bare GaN/Si(111) substrate.

A comparison between GaN and crystalline GSO-GaN/Si(111) spectra shows that the peak at 2θ=30.62° is a contribution of GSO, while the peak present at 2θ=34.60° is coming from GaN, for it is present in both GaN substrate and GSO-GaN. It can be noticed that at higher angles with respect to the intense GaN(002) peak, two shoulders are present: the strain engineering buffer layer is known to be a GaN superlattice despite the unknown exact conformation (section A), hence the multi-peak position and shape. Si(111) contribution is visible at ≈28.4°. Satellite subpeaks are present around GSO(002) diffraction peak: these are called Pendellösung (thickness) fringes, and they are a product of reflectance features caused by the low thickness of the oxide epitaxial layer. The spacing between the fringes can be used to calculate the oxide layer thickness, according to what explained in section 2.1.3 on page 40, which results in t_{ox} = 25.7 nm. This has the same order of magnitude of the thickness measured via X-ray reflectivity (XRR) but the value in the latter case results of 28.0 nm.
GSO(002) peak in the amorphous GSO-GaN/Si(111) spectrum is almost completely absent, which confirms that not relevant recrystallisation takes place in the layer. As it will be explained further in this work (section 4.4), it comes possibly from a crystalline interface layer.
d-spacings are calculated from diffraction angles, and hence the corresponding vertical cell parameters c_{GaN}=5.2 Å and c_{GSO}=5.8 Å are derived (section 2.1.3).

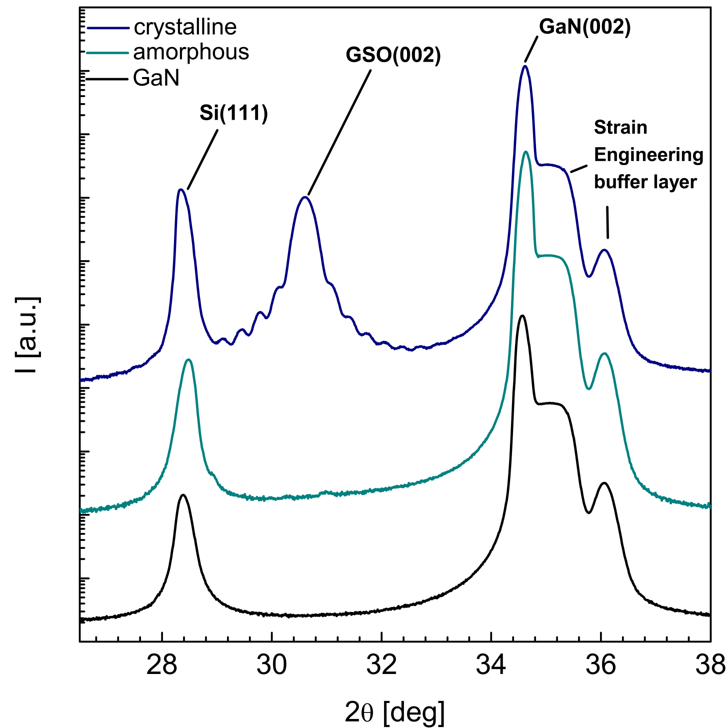

FIGURE 4.2: θ-2θ spectrum of GSO-GaN/Si(111).

Figure 4.3 shows θ-2θ spectrum of LLO-GaN/Si(111) compared to the former GSO-GaN/Si(111): the lower angle of the LLO(002) reflection shows that it has larger c lattice parameter than GSO, with c_{LLO}=6.0 Å; GaN has the same lattice parameter found in GSO-GaN/Si(111). For LLO peak, it is possible to notice the the Pendellösung fringes as well; the thickness computed from their spacing is 26.7 nm, in the same order of the thickness measured by XRR, which results 27.8 nm.

GSO-AlGaN/Si(111) clearly shows a different diffraction angle for (002) planes with respect to GaN, as shown in spectrum reported in figure 4.4; the GSO reflection instead shows the same value of GSO on GaN (shift within the error of 0.1°). AlGaN peak does not show the plateau at ≈35° because there is no strain engineering buffer layer, but only an AlN buffer between AlGaN and Si (fig. 3.2b). The c lattice parameters result to be c_{GSO}=5.9 Å and c_{AlGaN}=5.1 Å, slightly smaller than GaN, coherently to the lower ionic radius of Al^{3+}. The absence of satellite peaks of the GSO peak in GSO-AlGaN/Si(111) can be tracked back to a difference in 2θ scanning speed, merely chosen for timing reasons, that lowers the acquired spectrum resolution.

In the end, GSO-GaN/Sapphire is analysed and the result is shown in figure 4.5 compared once again to GSO-GaN/Si(111). No Si(111) and strain engineering buffer layer contributions are visible, as expected because of their absence in the sample stack; GaN(002) peak is in coherent position with the previous samples analysed, but a slight asymmetry towards higher angles suggests that the GaN buffer layer underneath the dislocations-free GaN (according to the stack presented in figure 3.2e) has a slightly different lattice parameter than the GaN layer considered part of the MOS gate stack. The GSO peak position is also shifted towards lower angles, but the effective difference is relative to lengths with order

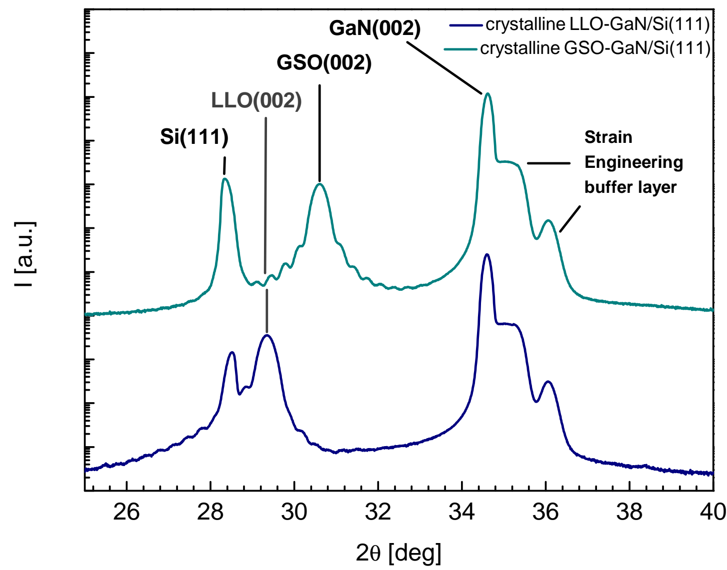

FIGURE 4.3: θ-2θ spectrum of LLO-GaN/Si(111) compared to GSO-GaN/Si(111). The shift of LLO(002) peak to lower angle with respect to GSO(002) peak can be noticed.

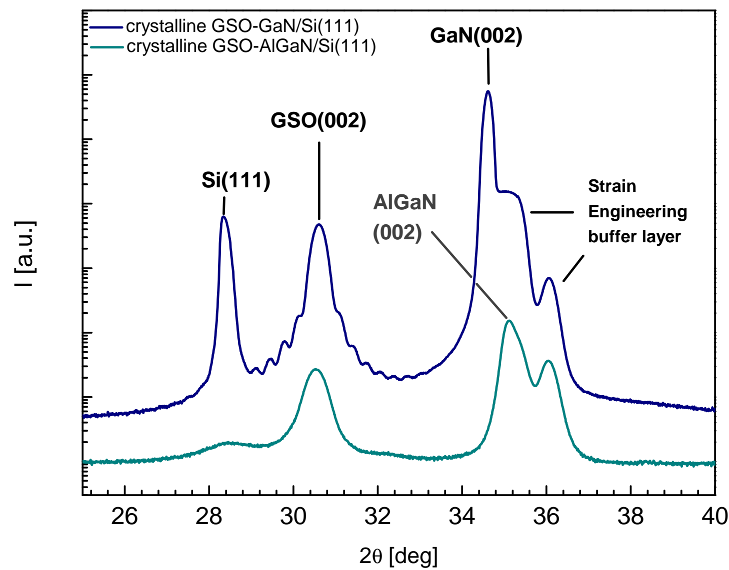

FIGURE 4.4: θ-2θ spectrum of GSO-AlGaN/Si(111) compared to GSO-GaN/Si(111). The same GSO peak can be noticed while the nitride's (002) shifts to higher angles because of the smaller lattice parameter.

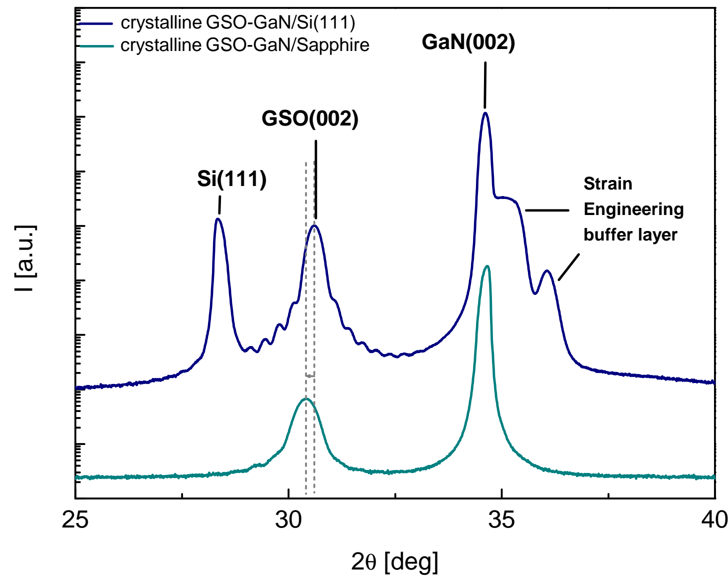

FIGURE 4.5: θ-2θ spectrum of GSO-GaN/Sapphire compared to GSO-GaN/Si(111). Similar GSO(002) and GaN(002) peaks can be noticed, with a slight shift of GSO(002) towards lower angles.

of magnitude of 10^{-2} Å therefore the lattice parameter is also c_{GSO}=5.9 Å. The GaN shows c_{GaN}=5.2 Å similarly to the previous GaN-based samples.

The in-plane lattice parameter a was first analysed by in-plane measurements, configuration of which is described in 2.1.3 on page 38: the measurement detects directly the hexagonal lattice (100) plane. GSO-GaN/Si(111) produced the spectrum shown in figure 4.6, in which a peak with very low signal to background ratio is visible at lower angles than the GaN(100) peak. The peak is too low to provide concrete evidence of being produced by GSO(100) but, in the hypothesis that the smeared peak is a GSO(100) contribution, it's possible to compute the a_{GSO} considering the center of the peak to be positioned in 2θ = 28.12° and therefore have a starting value to compute $^a/_c$ and plan the tilted θ-2θ experiment, along with the hypothesis of similar $^a/_c$. If so, the in-plane lattice parameter so deduced is a_{GSO}= 3.67 Å ≈ 3.7 Å. In reason of lower oxide thickness or higher defectiveness of the layers, any attempt to analyse GSO-AlGaN/Si(111) and GSO-GaN/Sapphire has instead been unsuccessful.

Another way to calculate the in-plane lattice parameter a_{GSO} is to perform a θ-2θ experiment with tilted sample, in order to get the reflections of (101) plane from oxide and semiconductor that provide $^a/_c$, where c is known from θ-2θ measurements. The tilting angle of acquisition is calculated as expressed in 3.2.1: 61,9° for GSO-GaN/Si(111) and 62.9° for LLO-GaN/Si(111) are used. Spectra of GSO-GaN/Si(111) and LLO-GaN/Si(111) are shown in figure 4.7: GaN provides peaks at ≈36.8° in both the measurements. GSO provides a well distinct peak at 32.4°, while LLO shows a peak at 31.0°. This measure is noisier than the latter, which is to be imputed to a no backdata-assisted choice of tilting angle, therefore the optimal χ was not reached with the first measure; since LLO peak had a satisfactory signal to noise ratio, no more measures at different χ have been run.

The d-spacings computed from these angles are of 2.77 Å for GSO and 2.45 Å for GaN, and the cell parameters derived from formula 2.4 are 3.6 Å and 3.2 Å

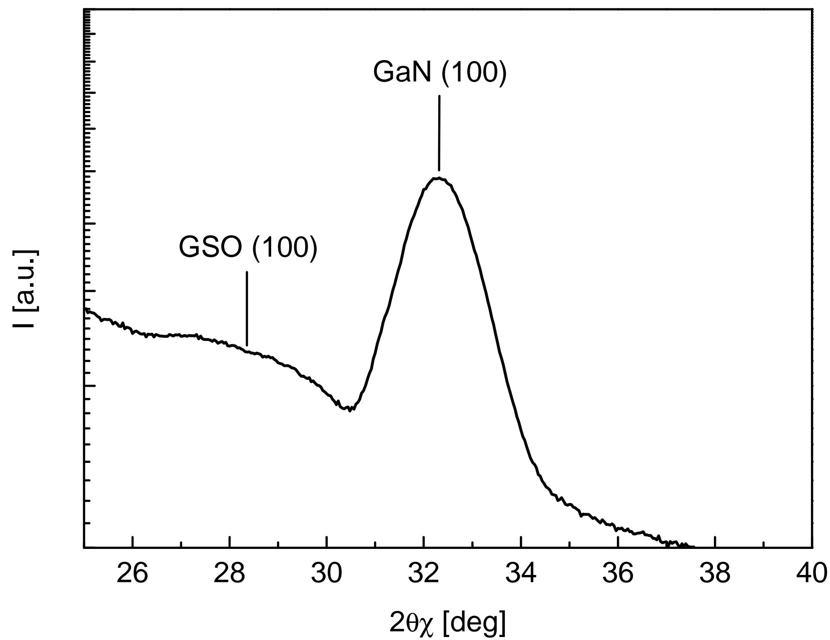

FIGURE 4.6: in-plane spectrum of GSO-GaN/Si(111).

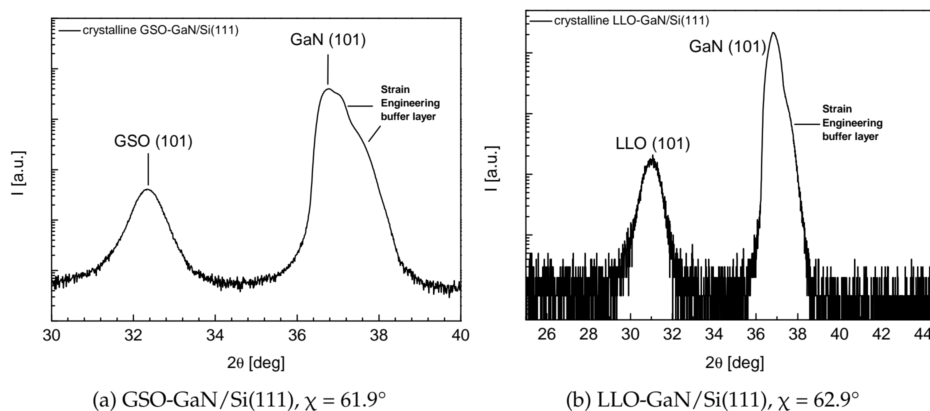

(a) GSO-GaN/Si(111), $\chi = 61.9°$

(b) LLO-GaN/Si(111), $\chi = 62.9°$

FIGURE 4.7: tilted sample spectra of GSO-GaN/Si(111) and LLO-GaN/Si(111).

System	Semiconductor			Oxide		
	c [Å]	a [Å]	c/a	c [Å]	a [Å]	c/a
GSO-GaN/Si(111)	5.2	3.2	1.607	5.8	3.6	1.586
LLO-GaN/Si(111)	5.2	3.2	1.621	6.0	3.8	1.610
GSO-AlGaN/Si(111)	5.1	3.2	1.607	5.9	3.6	1.610
GSO-GaN/Sapphire	5.2	3.2	1.621	5.9	3.6	1.629

TABLE 4.1: hexagonal cell parameters and their ratio for the crystalline oxide-(III-V) nitride/support systems.

respectively.
An analogous tilted θ-2θ experiment is performed also for GSO-AlGaN/Si(111) and GSO-GaN/Sapphire, with similar spectra obtained. The cell parameters deduced from the peaks position are 3.2 Å and 3.6 Å for both the samples, as detected in GSO-GaN/Si(111). It should be noticed that AlGaN has a slightly lower lattice parameter than GaN, but the 10^{-1} Å approximation makes the difference negligible to the final value of $a_{nitride}$. The overall picture of the hexagonal cells parameters of the crystalline oxide systems are recapped in table 4.1.

It is possible to state that LLO has larger cell parameters than GSO, that is coherent to the larger ionic radius of Lu^{3+} with respect to Sc^{3+}, given that La^{3+} and Gd^{3+} have more or less the same radius. More important is to notice that the in-plane cell parameters of GSO and LLO are larger than the same cell parameters of GaN and AlGaN, that implies the oxide layer to be relaxed on the semiconductor. Knowing if these values correspond to a fully relaxed layer is not possible, due to the lack of free-standing GSO and LLO hexagonal phases existence, but dislocations in the oxide are expected to be present and to influence the electrical behaviour of the system because of at least some lattice relaxation. The interface is better investigated by transmission electron microscopy in section 4.4.

4.1.3 Quality of the substrates

Rocking curve measurements are produced by making the source oscillate with respect to the detector, which is fixed at the 2θ angle of a (002) peak, in order to acquire signal from an asymmetric scattering condition. A perfect single crystal would not provide any signal when moving from the θ-2θ condition to the asymmetric ω-2θ condition by the relative movement of the source with respect to the detector; this measurement was performed to evaluate the GaN and GSO deviations from perfect crystallinity, aimed to the comparison between deposition of GaN on Si(111) and sapphire and its influence on the oxide grown on top of it. RC spectra around GaN(002) and GSO(002) peaks are shown in 4.8. Si(111)-supported system shows peaks at slightly higher ω angle than the sapphire-supported one because of the centre 2θ selected by the experiment design, as discussed in 3.2.1 on page 60. The FWHMs are visibly higher for Si(111)-supported GSO-GaN, with values of 0.626° compared to 0.085° and 0.357° compared to 0.139° for GaN(002) and GSO(002) peaks respectively. This translates in worse crystal quality of Si(111)-supported GaN with respect to the sapphire-supported, that partly affects the oxide quality.

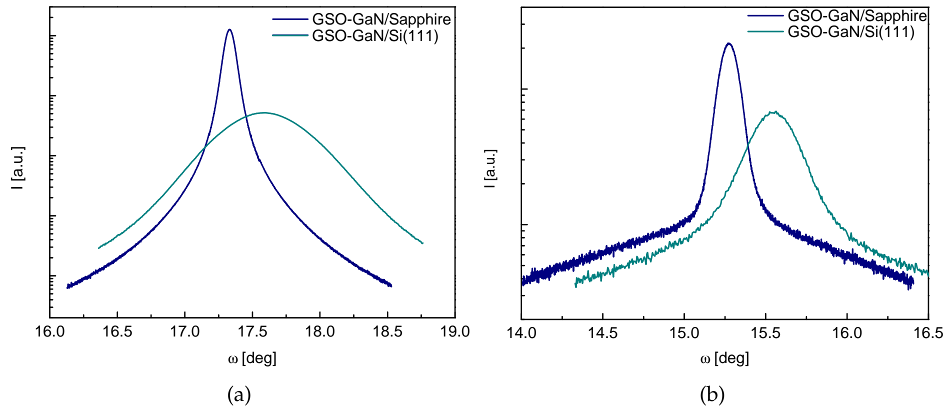

FIGURE 4.8: Rocking curves of (a) GaN(002) and (b) GSO(002) peaks for GSO-GaN/Si(111) and GSO-GaN/Sapphire.

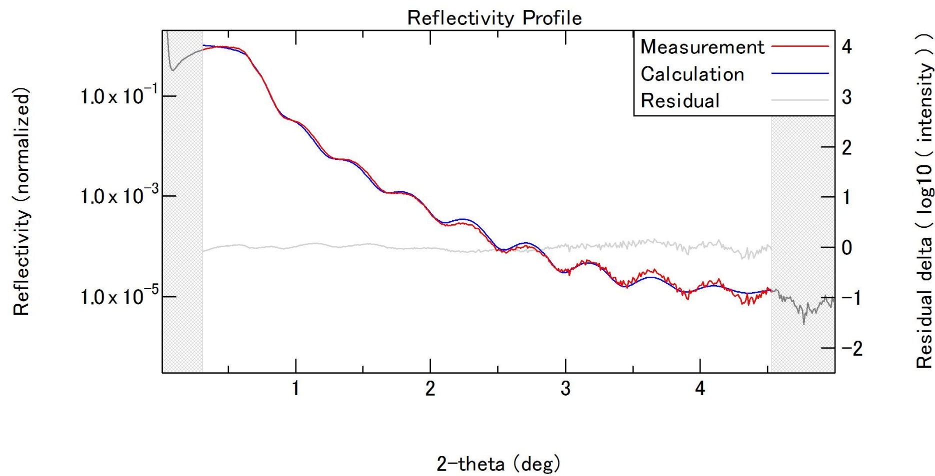

FIGURE 4.9: XRR spectrum and fitting of crystalline GSO-GaN/Sapphire system.

4.1.4 Oxide layer thickness

XRR analysis is used to measure the oxide layer thickness in all the amorphous and crystalline oxide systems, for the reason of using the actual thickness instead of the nominal thickness to evaluate the electric field in the oxide $E_{ox} = V_{gate}/t_{ox}$. A sample of the XRR spectrum is reported in figure 4.9 and a summary of the measured thickness values, deduced via spectral fitting or FT analysis as mentioned in 3.2.1 on page 61, is reported in table 4.2.
Spectral fitting provides also the density of semiconductor and oxide layer. Density of GSO referred to the spectrum shown in 4.9 is 7.07 g/cm^3, while GaN density is 6.15 g/cm^3 as reported in literature. GSO density derived from spectral fitting of GSO-GaN/Si(111) is 6.64 g/cm^3, with fluctuations of ± 0.2 g/cm^3 according to the angle interval considered; LLO density in LLO-GaN/Si(111) derived in the same way is 7.07 g/cm^3, higher with respect to GSO in GSO-GaN/Si(111) but equal to the density in GSO-GaN/Sapphire. The role of pinholes and defects in the discrepancy of density values for the same GSO hexagonal crystal is not investigated in this work, but it may represent a point of interesting further experiments.

System	Crystalline d [nm]	Amorphous d [nm]
GSO-GaN/Si(111)	28.0	29.3
LLO-GaN/Si(111)	27.8	-
GSO-AlGaN/Si(111)	28.7 27.9	28.0
GSO-GaN/Sapphire	18.8	22.25

TABLE 4.2: layer thicknesses of all the thick oxide film samples.

4.2 Bonds and Band Alignment of the oxide/III-V nitride systems from XPS investigation

XPS is a surface sensitive technique able to determine the composition of the sample within the escape depth of the electrons, as explained in chapter 2. A film of oxide thinner than the escape depth (4 nm) was used to acquire signal from photoelectrons of both the oxide and the semiconductor; additional analysis on the bare nitride samples were performed in order to obtain the band alignment of each Rare Earth Oxide/III-V Nitride system, and accordingly interpret the electrical behaviour.
A survey scan of all the spectrum using a monochromated X-ray beam (Al Kα) was followed by a high resolution investigation on the peaks of Ga*3p*, N*1s*, Gd*4s*, Sc$3p^{3/2}$, Al*2p*, O*1s* and valence band (VB), with charge removal executed by aligning Ga$3p^{3/2}$ to the standard value of 105.1 eV for Ga*3p* in GaN, using the alignment of N1s peak to 397.0 eV to check the constant value of charging along the spectrum.[68] The peaks considered for the determination of band alignment were O*1s* with the inelastic scattering tail and VB according to the method described in 2.2.4.

4.2.1 Elemental and bond analysis

Ga*3p* peak of crystalline GSO-GaN/Si(111) is plotted against the same peak in bare GaN/Si(111) in figure 4.10.

It is possible to see two contributions to the peak in both GSO-GaN/Si(111) and bare GaN/Si(111): the defined position of the two contributions to the peak suggests the presence of a second type of covalent bond of different nature from Ga-N, rather than a charging effect. All the Ga-O interactions that lead to the formation of a bond with Ga are excluded, because GaN is stable in the environment and a native Ga_2O_3 is not commonly formed on GaN wafers[74]; moreover, Ga-O is blueshifted with respect to Ga-N therefore Ga-O in the spectra would be associated to a bigger area than Ga-N, which is inconsistent with the expectation of Ga-O contaminations in a substantially Ga-N matrix, especially for the spectrum of bare GaN where the signal comes from GaN through the entire escape depth of the electrons. Knowing that both Si(111) and Sapphire wafers are cleaned with HCl after the III-V nitride MBE deposition, whether the cleaning procedure was followed by a PLD deposition of the oxide or not, Ga-Cl could be a redshifted contribution from the main Ga-N peak. The Ga-Cl peak features are coherent to the same peak appearance described in literature for halides contamination in GaN cleaned with HCl and HF mixtures.[75] Chlorine contamination was confirmed

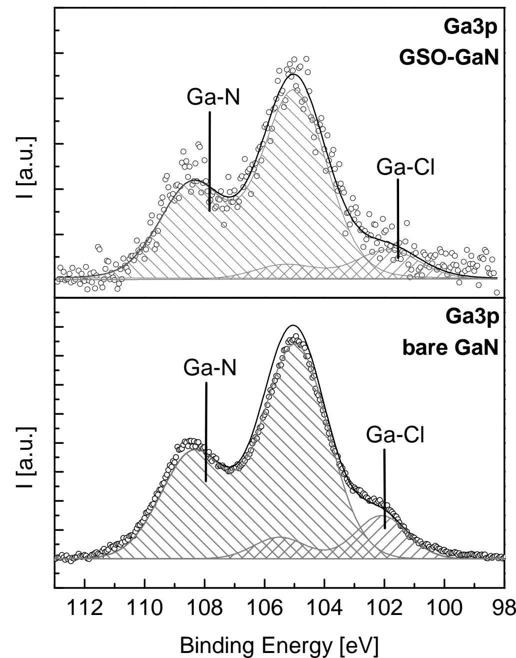

FIGURE 4.10: Ga*3p* peak in crystalline GSO-GaN/Si(111) and bare GaN/Si(111). Ga-Cl produces the redshifted contribution with respect to the main Ga*3p* peak, associated to Ga-N.

by the Cl*3s* peak presence at 16÷17 eV as reported in literature.[68] Cl contamination is not expected to have any relevant impact on the electrical properties of the MOS capacitor, because Cl accumulation at the surface was not visible in the TEM imaging of oxide-GaN interface (and in an EDX analysis produced in Forschungzentrum Jülich[1]). Testing a sample cleaned with different species can be a cue for further work.
Comparison between Ga*3p* peaks of crystalline GSO-GaN/Si(111), amorphous GSO-GaN/Si(111), crystalline GSO-AlGaN/Si(111) and amorphous GSO-AlGaN /Si(111) are shown in figure 4.11. No relevant difference between peaks of amorphous and crystalline oxides is visible for each kind of nitride; Ga*3p* peaks are less intense in GSO-AlGaN/Si(111) than in GSO-GaN/Si(111), but the reason for the lower intensity is not investigated in this work. The reason may be a higher GSO thickness, that limits the signal coming from the semiconductor; alternatively, considering the density of pinholes seen in the case of AlGaN at the optical microscope for electrical measurements and at the TEM, it is also possible that the escape depth of the electrons is sensibly reduced and a larger portion of photoemitted electrons from AlGaN undergo inelastic scattering before being expelled from the sample, with a further reduction of the intensity of the peak.

Binding energy around the expected value for N*1s* shows several distinctive features:

- N*1s* peak;
- Gd*4s* and Sc$2p^{3/2}$ from GSO;
- LMM Auger lines of Gallium related to the Al Kα source.[74]

[1]not availble for this work.

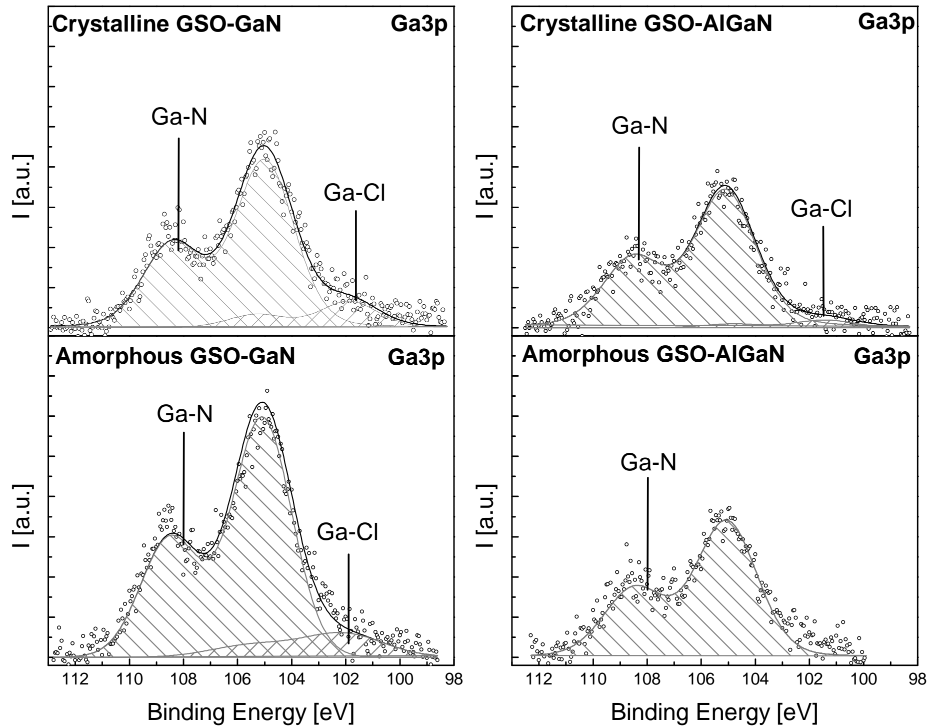

FIGURE 4.11: Ga*3p* peak in crystalline and amorphous GSO deposited on GaN and AlGaN.

Auger LMM peaks are overlapped and redshifted of 1-2 eV with respect to N*1s*; the distinction between Gd*4s*, Sc$2p^{3/2}$ and N*1s* is evident considering the standard values of the peaks (in Gd_2O_3 and Sc_2O_3 for the no-backdata-assisted GSO [68]) and the comparison of GSO-GaN and bare GaN spectra: in particular, the peaks from GSO are blueshifted with respect to N*1s*. In figure 4.12a, N*1s* spectrum of crystalline GSO-GaN is plotted against bare GaN. Gd and Sc are not present in LLO-GaN, consistently with the absence of Gd*4s* and Sc$2p^{3/2}$ peaks in N*1s* region, as visible in figure 4.12b.

A comparison between N*1s* peaks of crystalline GSO-GaN/Si(111), amorphous GSO-GaN/Si(111), crystalline GSO-AlGaN/Si(111) and amorphous GSO-AlGaN /Si(111) are shown in figure 4.13. No relevant difference between the peaks of amorphous and crystalline oxides for each kind of nitride are visible, therefore the same considerations on the influence of the III-V Nitride chemical nature on the electronic band alignment and electrical properties made for Ga*3p* comparison apply.

O*1s* peaks for crystalline and amorphous GSO deposited on GaN and AlGaN are shown in figure 4.14. In all the spectra, two contributions of bonds with oxygen are visible: this is coherent with the fact that rare earth oxides are highly hygroscopic, therefore O-H bonds are present with the oxygen atoms in the crystal, without considering absorbed water H_2O. The ratio between O-Gd/Sc and O-H peaks is a qualitative indication of the quality of the film, because higher defectiveness translates in a larger amount of chemisorbed humidity, therefore a higher relative intensity of O-H peak with respect to O-Gd/Sc. With this information, it is possible to state that the amorphous oxide is less defective than the crystalline oxide on both the substrates, in line with the fact that an amorphous oxide is less sensitive to its substrate defects with respect to a layer grown epitaxially, such as the crystalline

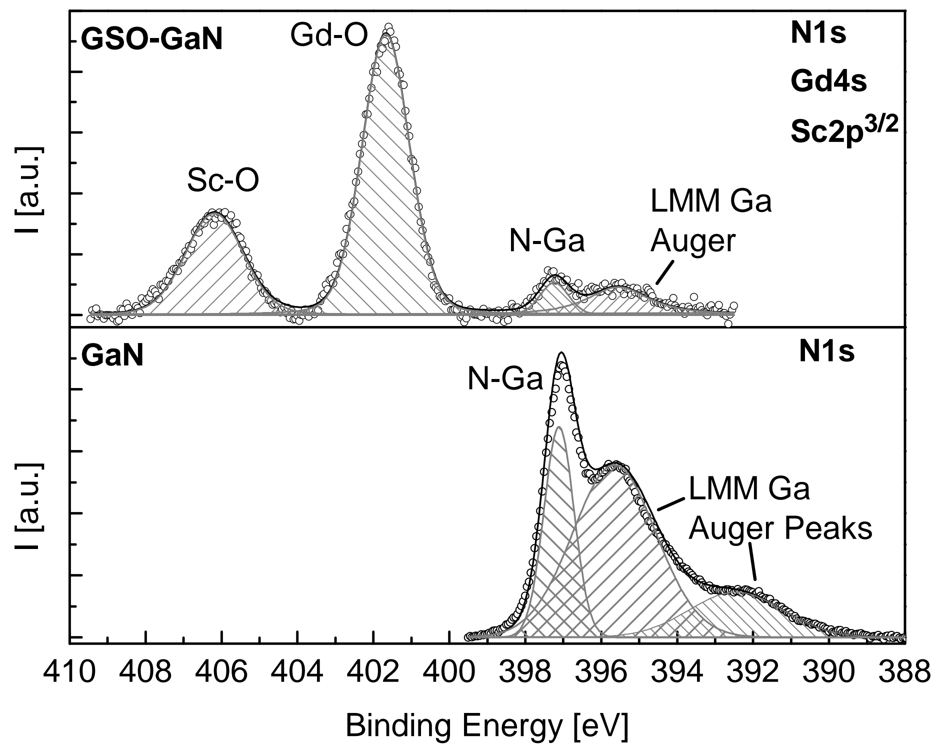

(a)

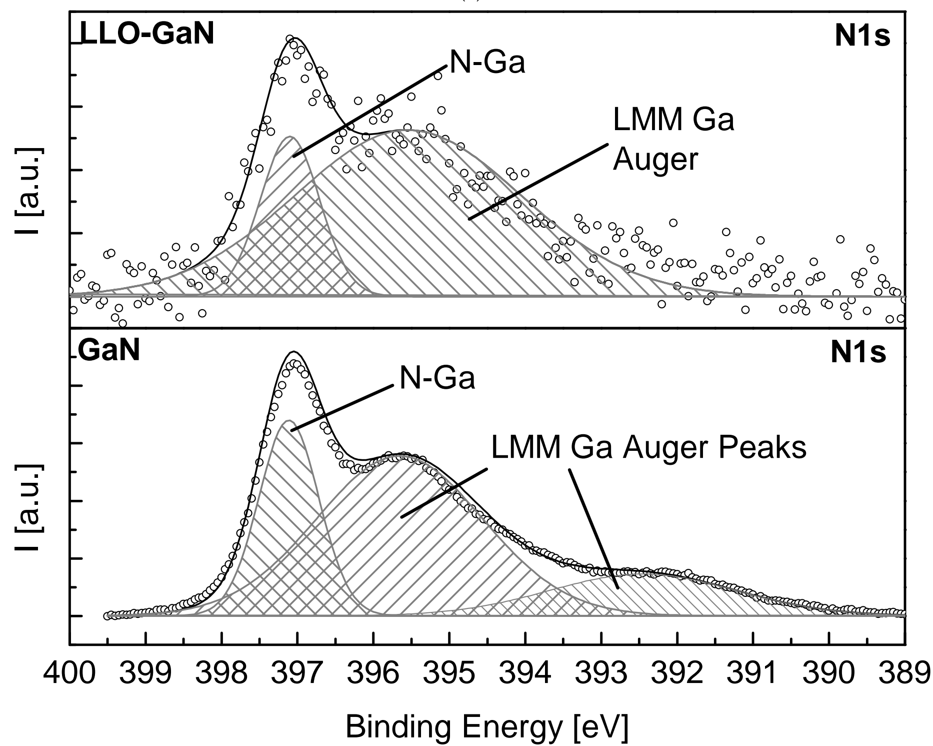

(b)

FIGURE 4.12: N*1s* spectra of GSO-GaN and LLO-GaN compared to bare GaN substrate. Gd*4s* and Sc*2p*$^{3/2}$ contributions are visible in GSO-GaN and absent in LLO-GaN.

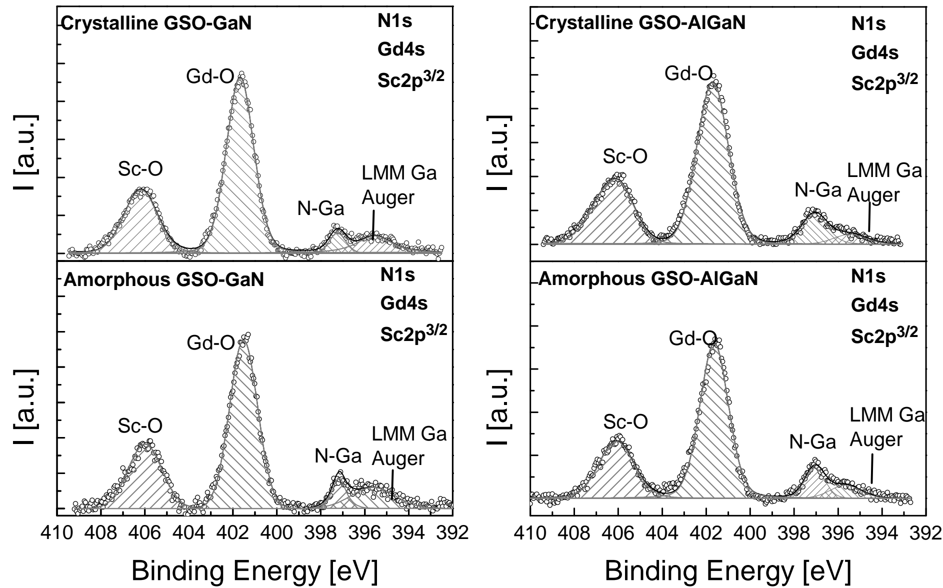

FIGURE 4.13: N*1s* spectra of crystalline and amorphous GSO deposited on GaN and AlGaN.

oxide on the semiconductor, that replicates the defects on which it is grown. With this relation between amorphous and crystalline layers, it is possible to see that GSO deposited on AlGaN shows much more consistent O-H peaks than GSO-GaN; this is an indication of worse quality of AlGaN/Si(111) that is mirrored in a higher defectiveness of GSO: confirmation of this assumption is evident in electrical measurements and TEM imaging of the interface (section 4.3 and 4.4).

O*1s* peak of LLO-GaN/Si(111) also shows a very intense O-H contribution, as shown in figure 4.15. Both the peaks are redshifted of ≈ 0.7 eV with respect to GSO-GaN/Si(111), because of a non constant charging along the spectrum rather than a different electronic affinity of the cations as the only reason, since Lu, La, Gd and Sc are characterised by an electronegativity that differs of $0.1 \div 0.2$; the high absorption of humidity can be attributed to the higher density of dislocations expected from a relaxed film with larger lattice mismatch with the GaN underneath than GSO.

GaN grown on Sapphire showed a very high surface charging (≈ 72 eV) non constant along the spectrum, coherently with the insulating nature of Al_2O_3, when analysed without any grounding solution; the analysis was run again making use of silver paste to ground the semiconductor to the metallic stage bypassing the sapphire layer, producing the spectra shown in figure 4.16. Charging along the spectrum results constant in this case, but Gd*4s* and Sc$2p^{3/2}$ show tailing towards higher binding energies as an effect of surface charging.[67] In general, the spectral features for Ga*3p* and N*1s* are not different from the same system deposited on Si(111); O*1s* shows a very intense and broad O-H contribution, despite the high quality of the interface seen at the TEM and the good electrical measurements, unlike the case of GSO-AlGaN. A possible explanation lies in the cell parameters exposed in table 4.1, where it is visible that GSO deposited on GaN/Sapphire has relatively higher c/a ratio, therefore the higher strain of the crystal enhances the humidity chemisorption without meaning large defectiveness in GSO crystal and in GaN underneath.

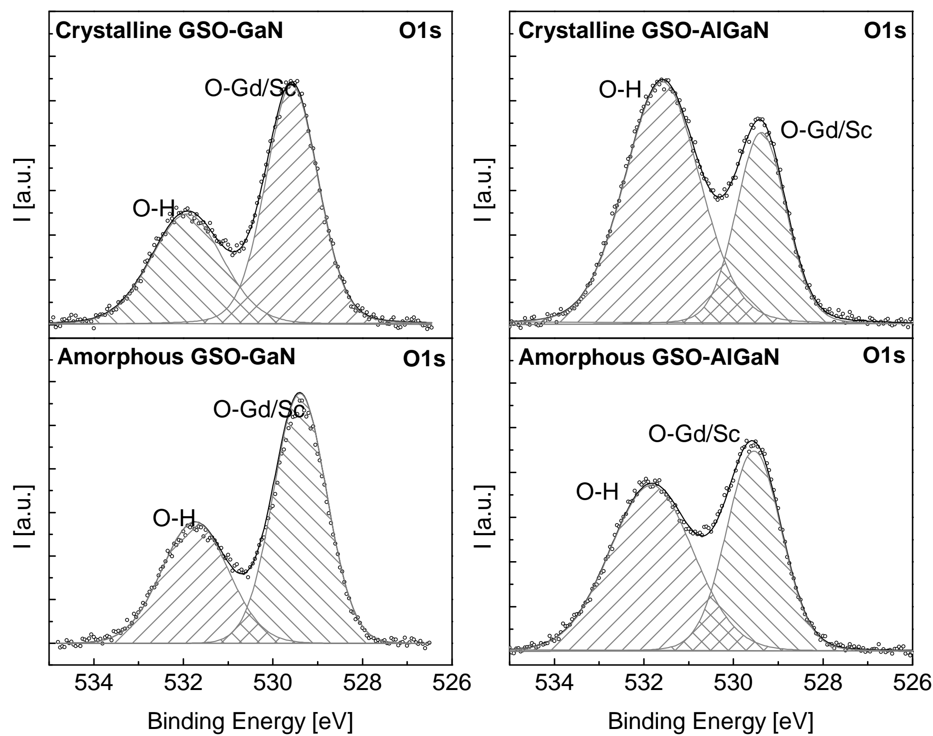

FIGURE 4.14: O*1s* peak in crystalline and amorphous GSO-GaN/Si(111) and GSO-AlGaN/Si(111). The O-H contribution of the hygroscopic oxide is visible in the blueshifted peak.

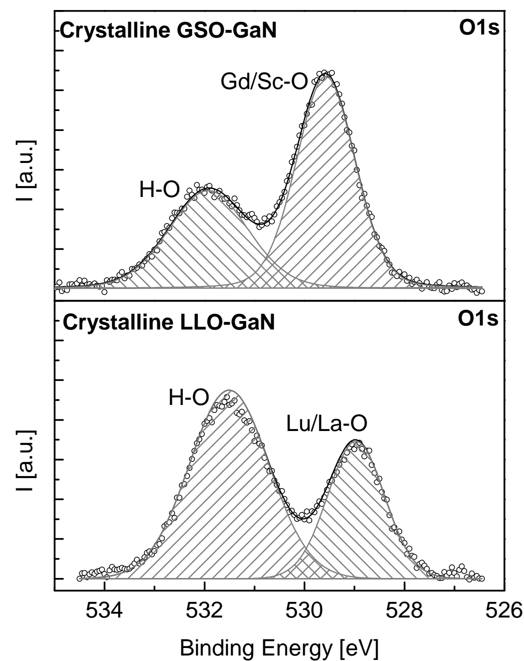

FIGURE 4.15: O*1s* peak of LLO-GaN/Si(111) compared to GSO-GaN/Si(111). The O-H contribution in LLO is higher than the equivalent in GSO because of the higher dislocation density induced by the relaxation of the epitaxial layer with larger lattice parameters.

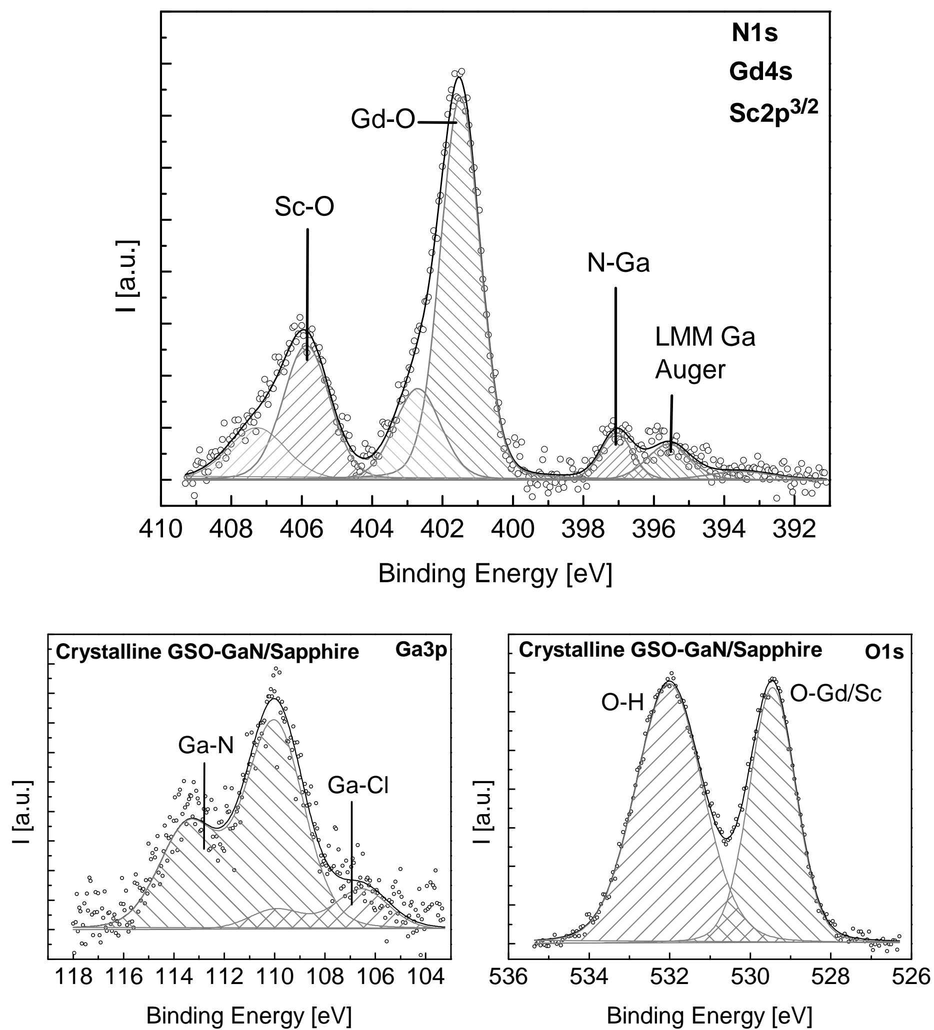

FIGURE 4.16: N*1s* spectra of crystalline GSO-GaN grown on sapphire wafer. Tailing of Gd and Sc peaks is visible in N*1s* spectrum.

4.2.2 Oxide energy gap measurement

O*1s* fitted peak and the related electron energy loss (EEL) onset were used to determine the band gap of the rare earth oxide, according to the method described in 2.2.4 relative to the evaluation of the inelastic scattering tail described in 2.2.1. The spectrum of amorphous and crystalline oxide with the inelastic scattering tail and the evaluation of the onset by linear regression is shown in figure 4.17. Recalling the derivation of the band gap:

$$E_{gap} = E_{onset} - E_{O1s(max)} \tag{4.1}$$

where E_{onset} is the energy of the lowest electron energy loss contribution, and $E_{O1s(max)}$ is the position of the O*1s* peak associated to the inelastic scattering tail evaluated.

The procedure is repeated for all the samples, leading to similar results for GSO deposited on AlGaN/Si(111) and GaN/Sapphire, while LLO showed a wider band gap with respect to GSO. The band gaps are summarised in table 4.3.

4.2.3 Valence band offset

The offset between the valence band of GaN and GSO/LLO is evaluated from the difference of onset of the valence band contributions produced by the oxide and the semiconductor. Each onset is identified with the intercept of the linear interpolation of the VB peak with the average background, taken equal to 0 eV since no electrons are emitted from the sample at any energy lower than $E = E_{gap}$. Details on the valence band offset (VBO) evaluation are exposed in 2.2.4 and 3.3. VBO evaluation for crystalline and amorphous GSO-GaN/Si(111) is shown in figure 4.18; the bare GaN sample is essential to assign each VB contribution to the correct phase of the system. Recalling the derivation of VBO:

$$VBO = E_{VB}^{semiconductor} - E_{VB}^{oxide} \tag{4.2}$$

where valence band of GaN/AlGaN is at higher energy than valence band of GSO/LLO.
VBO of the different Rare Earth Oxide/III-V Nitride systems are summarised in table 4.4.

4.2.4 Staggered Band Alignment

The band alignment between oxide and semiconductor is crucial to interpret electrical measurements and forecast the behaviour of the MOS gate stack, with a view to the exploitation of the systems in power electronics and optoelectronic devices. The band alignment is derived knowing:

1. the **oxide band gap**, derived from EEL evaluation on O*1s* peak (4.2.2);
2. the **semiconductor band gap**, known from literature[**Schubert2005**, 76];

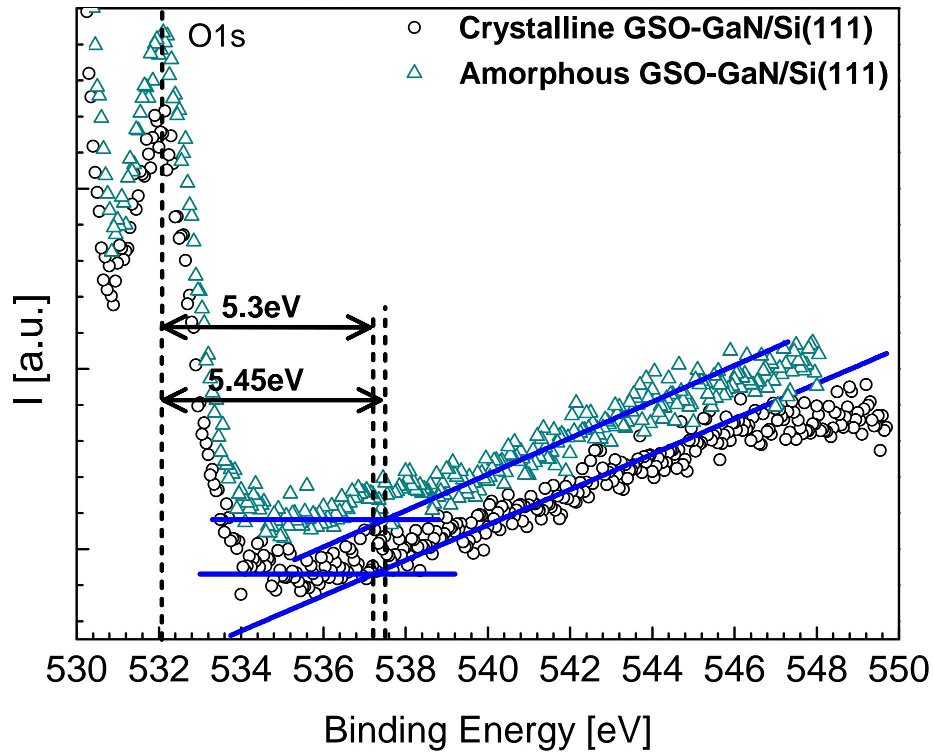

FIGURE 4.17: evaluation of E_{gap} by linear interpolation of the background at the base of the peak (high B.E.) and the inelastic scattering tail for O*1s* contribution from the oxide.

System	EEL onset [eV]	O*1s* peak [eV]	E_{gap} [eV]
cryst GSO-GaN/Si(111)	537.20	531.90	5.30 ± 0.15
cryst GSO-AlGaN/Si(111)	537.10	531.60	5.50 ± 0.15
cryst GSO-GaN/Sapphire	536.90	531.75	5.15 ± 0.15
cryst LLO-GaN/Si(111)	537.20	531.50	5.70 ± 0.15
amorph GSO-GaN/Si(111)	537.20	531.75	5.45 ± 0.15
amorph GSO-AlGaN/Si(111)	537.30	531.80	5.50 ± 0.15
amorph GSO-GaN/Sapphire	537.00	532.00	5.00 ± 0.15

TABLE 4.3: Energy gap evaluation by Miyazaki method described in 2.2.4. cryst = crystalline, amorph = amorphous.

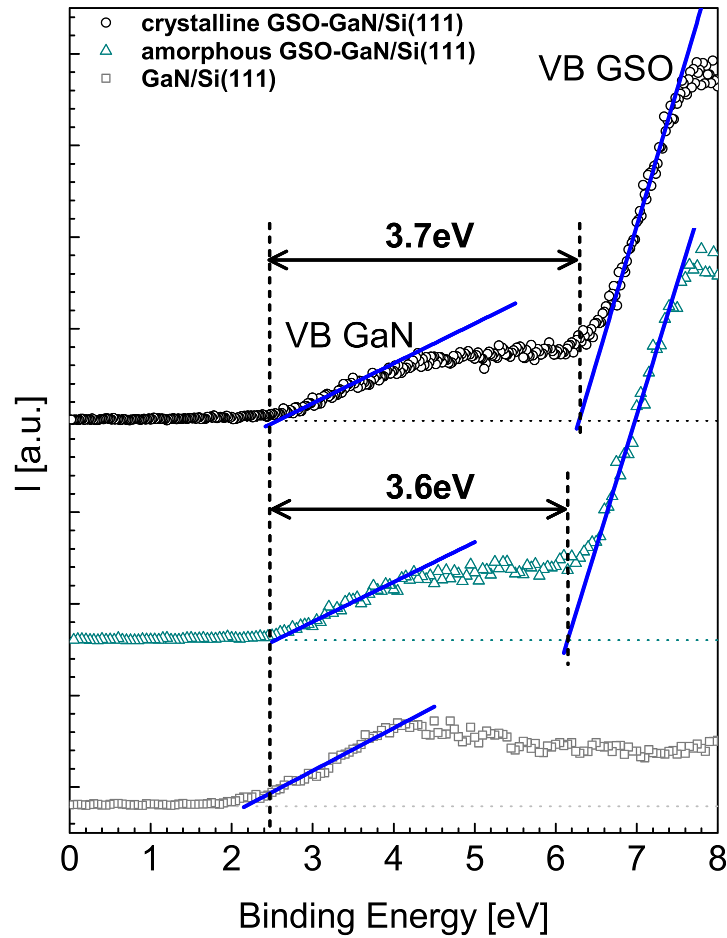

FIGURE 4.18: Valence band of crystalline and amorphous GSO-GaN/Si(111) compared to bare GaN/Si(111) and related VBO calculation.

System	Oxide VB [eV]	III-V(N) VB [eV]	VBO [eV]
cryst GSO-GaN/Si(111)	6.29	2.57	3.70 ± 0.15
cryst GSO-AlGaN/Si(111)	6.51	2.63	3.90 ± 0.15
cryst GSO-GaN/Sapphire	6.57	2.82	3.75 ± 0.15
cryst LLO-GaN/Si(111)	6.13	2.28	3.85 ± 0.15
amorph GSO-GaN/Si(111)	6.14	2.53	3.60 ± 0.15
amorph GSO-AlGaN/Si(111)	6.30	2.38	3.90 ± 0.15
amorph GSO-GaN/Sapphire	6.22	2.56	3.70 ± 0.15

TABLE 4.4: VBO evaluation after the deduction of the oxide valence band onset with respect to the semiconductor's.

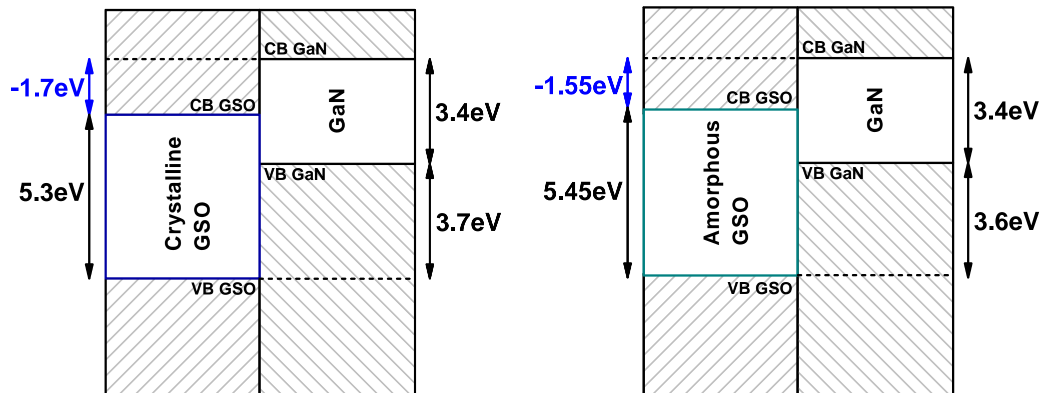

FIGURE 4.19: Band alignment of crystalline and amorphous GSO-GaN/Si(111). The bands are staggered because of the high band gap of GaN and valence band offset; the conduction band offset is negative from GaN to GSO (in blue).

3. the **valence band offset** between oxide and semiconductor derived from the VB spectrum of the thin film samples (4.2.3).

The valence band offset is of the order of 3÷4 eV, with the semiconductor VB at higher energy with respect to the oxide. Being III-V Nitrides high band gap semiconductors, with E_{gap}^{GaN} = 3.4 eV and E_{gap}^{AlGaN} = 4.6 eV, the conduction band (CB) of the semiconductor is found at an energy $\approx$ 7 eV higher than the VB of the oxide; being the $E_{gap}^{GSO/LLO}$ $\approx$ 5.5 eV, the conduction band of the oxide is placed at a lower energy with respect to the conduction band of the semiconductors.
Therefore, the band alignment between the oxide and the semiconductor is *staggered*, with the electrons feeling no potential barrier when flowing from the semiconductor to the oxide (positive voltage applied to the electrode on the oxide side in the MOS capacitor), thus a current generation through the oxide is expected when positive potential is applied. On the contrary, negative potential applied to the same electrode results in a even higher potential barrier for the electrons to overcome, therefore no current generation is expected unless very low voltages are applied, in a diode-like behaviour: a detailed explanation of the electrical behaviour related to the band alignment is written in section 4.3.1 in light of the electrical measurement results.
The band alignment of crystalline and amorphous GSO-GaN/Si(111) is reported in figure 4.19; consistently with the similar values of E_{gap} and VBO between crystalline and amorphous oxides in the same Rare Earth Oxide/III-V Nitride system, the band alignment of crystalline GSO-GaN/Si(111), GSO-AlGaN/Si(111), GSO-GaN/Sapphire and LLO-GaN/Si(111) is shown in figure 4.20, while the band alignment values for all the systems are summarised in table 4.5.

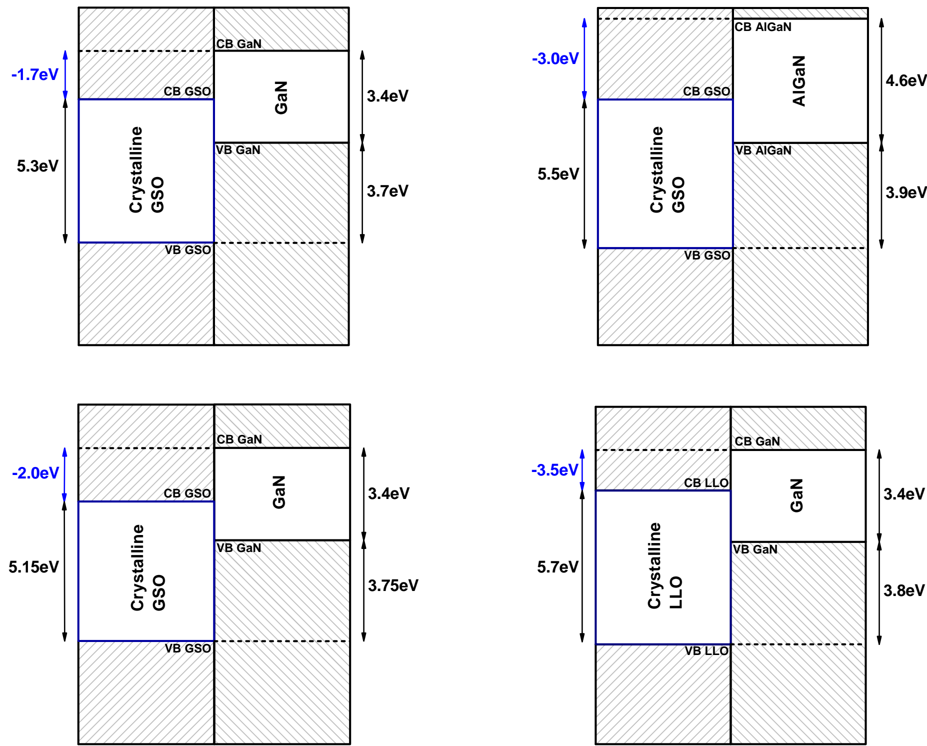

FIGURE 4.20: Band alignment of crystalline GSO-GaN/Si(111) (top left), crystalline GSO-AlGaN/Si(111) (top right), crystalline GSO-GaN/Sapphire (bottom left), crystalline LLO-GaN/Si(111) (bottom right).

System	E_{gap}^{oxide} [eV] ± 0.15	$E_{gap}^{III-V(N)}$ [eV] ± 0.15	VBO [eV] ± 0.15	CBO [eV] ± 0.15
cryst GSO-GaN/Si(111)	5.30	3.40	3.70	-1.7
cryst GSO-AlGaN/Si(111)	5.50	4.60	3.90	-3.0
cryst GSO-GaN/Sapphire	5.15	3.40	3.75	-2.0
cryst LLO-GaN/Si(111)	5.70	3.40	3.85	-3.5
amorph GSO-GaN/Si(111)	5.45	3.40	3.60	-1.55
amorph GSO-AlGaN/Si(111)	5.50	4.60	3.90	-3.0
amorph GSO-GaN/Sapphire	5.00	3.40	3.70	-2.1

TABLE 4.5: Staggered band alignment of the Rare Earth Oxide/III-V Nitride systems.

4.3 Electrical behaviour of Al/oxide/III-V nitride systems

The staggered band alignment of the Rare Earth Oxide/III-V Nitride systems is expected to produce an asymmetrical electrical behaviour, because the flow of electrons from the semiconductor to the oxide and the electrode of the MOS capacitor is not hindered by a potential barrier in the conduction band. This opposes the general trend in MOS gate dielectrics, where the band gap constitutes a potential barrier also in conduction band, as shown in picture **??**. Tests on current and capacitance response to voltage application were performed on Al/oxide/III-V nitride MOS capacitors using a two-point probe; the bias was applied to the Al pad while the substrate (body) contact, produced as described in Appendix A, was grounded.
Electrical behaviour was tested for crystalline and amorphous GSO-GaN/Si(111), crystalline and amorphous GSO-GaN/Sapphire, and crystalline GSO-AlGaN/Si(111). Amorphous GSO-AlGaN/Si(111) was not tested after the electrical response of two crystalline GSO-AlGaN/Si(111) samples, along with a TEM imaging of the GSO-AlGaN interface that showed extremely high density of threading dislocations and pinholes, discussed in section 4.4.2.

4.3.1 Current-Voltage curves

The current response to the application of a continuous voltage (I-V) was tested on different capacitors for positive and negative bias, respectively between 0÷30 V and 0÷-40 V. The I-V curves shown for each system were assembled from two different measures of I-V in positive and negative bias application; the chosen curves have the statistical value of an average behaviour, since breakdown is a stochastic process depending on the local field induced by defects and practical fluctuations in the analysis, reason why multiple measures were performed on MOS capacitors across the sample under the same operative conditions. The current was limited to 10 mA in order to avoid damages to the instrument, therefore an abrupt increase in the current up to the limit value means that the dielectric breakdown happened.
The I-V curve of crystalline GSO-GaN/Si(111) is shown in figure 4.21: breakdown occurs at $\approx$ 7 MV/cm when positive bias is applied, but it does not occur up to the limit of the instrument when a negative bias is applied. The difference in breakdown voltage is the confirmation of the assumptions made considering the staggered band alignment. No potential barrier is felt by the electrons in conduction band when they are attracted towards the positive potential of the MOS capacitor across the oxide: therefore, the dielectric is not hindering the flow by providing a potential barrier. The average breakdown field in crystalline GSO-GaN/Si(111) is 6.0 $\pm$ 1.5 MV/cm in positive bias and never less negative than -10÷-12 MV/cm under negative bias, when breakdown was actually reached (it is to remind the limit voltage of the instrument of 40V, corresponding to $\approx$ -14 MV/cm for a layer of $\approx$ 30nm).
In the I-V plot it is possible to notice that current flow (dielectric breakdown) is not immediate: the oxide layer is a resistor, despite it does not provide a potential barrier, therefore the potential applied to make current flow needs to outmatch the ohmic drop of the dielectric first. It is expected that asymmetric behaviour is representative for a staggered band alignment; the breakdown field in one direction is dependent on the thickness and defectiveness of the layer: thinner and defective layers show a higher availability of least-resistance paths through the

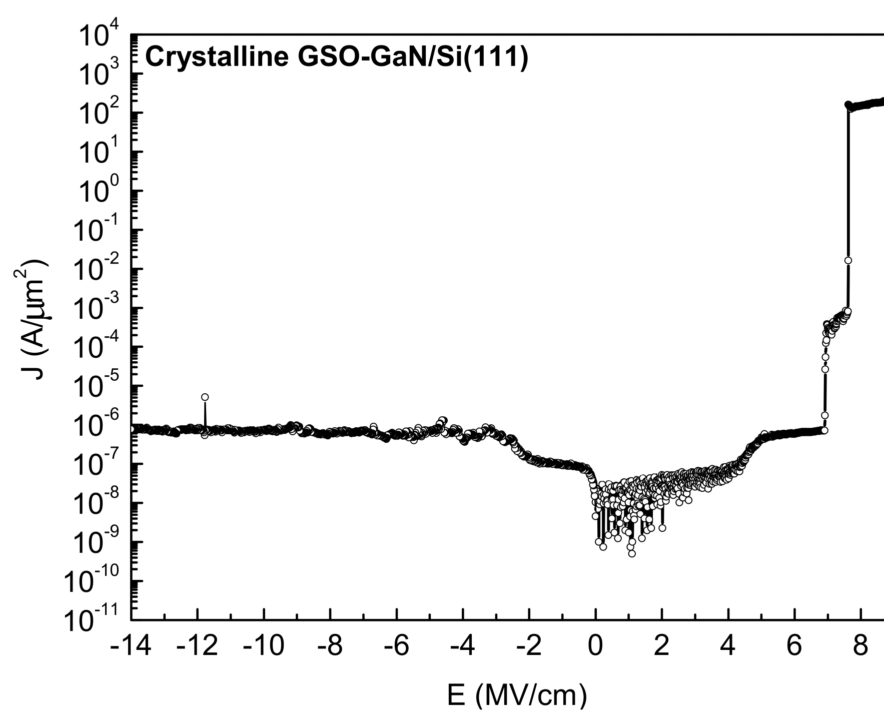

FIGURE 4.21: Asymmetric electrical behaviour of the Al/GSO/GaN/Al capacitor from crystalline GSO-GaN/Si(111), under positive and negative bias application. BD occurs at ≈ +7 MV/cm while no breakdown happens under negative bias up to the instrumental limit.

layer, therefore the probability of breakdown occurrence.
In figure (4.21) it is also possible to notice a two-step abrupt current increase, mirror of a breakdown involving two mechanisms; one-step breakdown was observed in other MOS capacitors of the same sample under positive bias, therefore it is dismissed as a statistical phoenomenon, and not a characterising mechanism of breakdown of the system.

Crystalline and amorphous GSO-GaN/Si(111) are compared in figure 4.22. The average breakdown field for amorphous GSO-GaN/Si(111) is higher than the crystalline GSO-GaN/Si(111) one, being around 8.0 ± 1.0 MV/cm. This can be explained by the fact that amorphous oxide is not sensitive to the defects in GaN, unlike the epitaxial crystalline film as already anticipated in 4.2.1 on page 75. The same trend is found in GSO-GaN/Sapphire, for which the the I-V plot is omitted.

For the same reason, GaN grown on different substrates can influence the electrical behaviour of the oxide above it through the different density of defects and pinholes generated from dislocations in the semiconductor, that is MBE deposited on different substrates with the aid of a buffer layer specifically to limit the dislocation density (Appendix A). The behaviour of crystalline GSO-GaN/Si(111) and crystalline GSO-GaN/Sapphire is compared in figure 4.23: it is possible to notice that the field is different in the two oxides, since GSO on GaN/Sapphire is only 20nm thick therefore the voltage translates in a different field. Asymmetry is preserved, with breakdown in GSO-GaN/Sapphire that occurs earlier with respect to GSO-GaN/Si(111): 2.5±2 MV/cm and 6±1.5 MV/cm respectively. TEM interface imaging suggest that GaN/Sapphire has a better quality as a substrate with respect to GaN/Si(111) despite the strain engineering buffer layer, but XPS

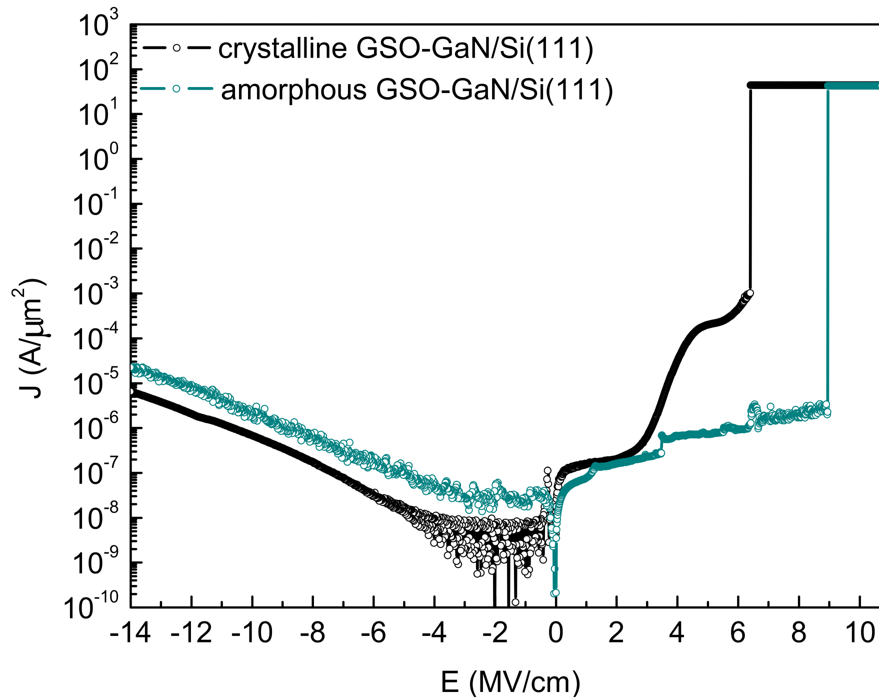

FIGURE 4.22: Crystalline and amorphous GSO-GaN/Si(111) indicative electrical behaviour compared. Statistically, the breakdown occurred earlier in the case of the crystalline oxide with respect to the amorphous oxide.

shows that GSO grown on GaN/Sapphire absorbs higher atmospheric humidity with respect to GSO-GaN/Si(111), which can be related to a higher defectiveness of the oxide layer. Further investigations with different oxide thicknesses GSO-GaN/Si(111) are required to characterise the dependence of dielectric breakdown in GSO-GaN/Sapphire on the substrate quality. In general, GSO-GaN/Sapphire appears to be less breakdown resistant than GSO-GaN/Si(111).

GSO-AlGaN/Si(111) I-V behaviour was also tested under the same conditions. It was visible that breakdown occurred immediately for all the MOS capacitors tested and applying both positive and negative bias. A sample behaviour is shown in the I-V plot in figure 4.24. The broken dielectric behaviour can be explained with an extremely high amount of least-resistance-paths across the oxide layer along all the sample; C-V measurements also resulted in a non-typical behaviour for a MOS capacitor, as shown further on (section 4.3.2), with a high contribution that can be related to traps activated by higher frequencies. TEM imaging of the interface and optical microscopy show that the AlGaN surface is characterised by an extremely high density of pinholes and dislocations, with the oxide growing on the surface and in the defects alike. Therefore, the broken behaviour can be regarded as the product of a very high defectiveness of the oxide layer grown in pinholes, rather than the characteristic behaviour of the stack. The confirmation of the staggered band alignment and other considerations on electrical behaviour of crystalline and amorphous GSO-AlGaN/Si(111) are subordinate to the production of higher quality samples, and are no longer considered in this work.

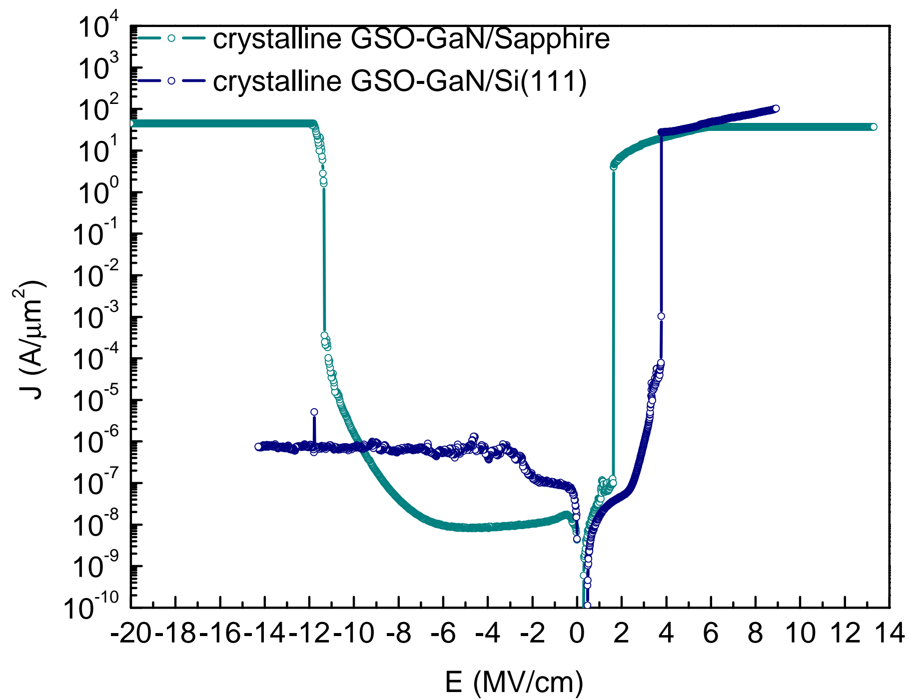

FIGURE 4.23: Crystalline GSO-GaN/Si(111) and crystalline GSO-GaN/Sapphire indicative electrical behaviour compared. Statistically, the breakdown occurred earlier in the case of GaN-on-Sapphire with respect to GaN-on-Si, according to the lower thickness of the oxide.

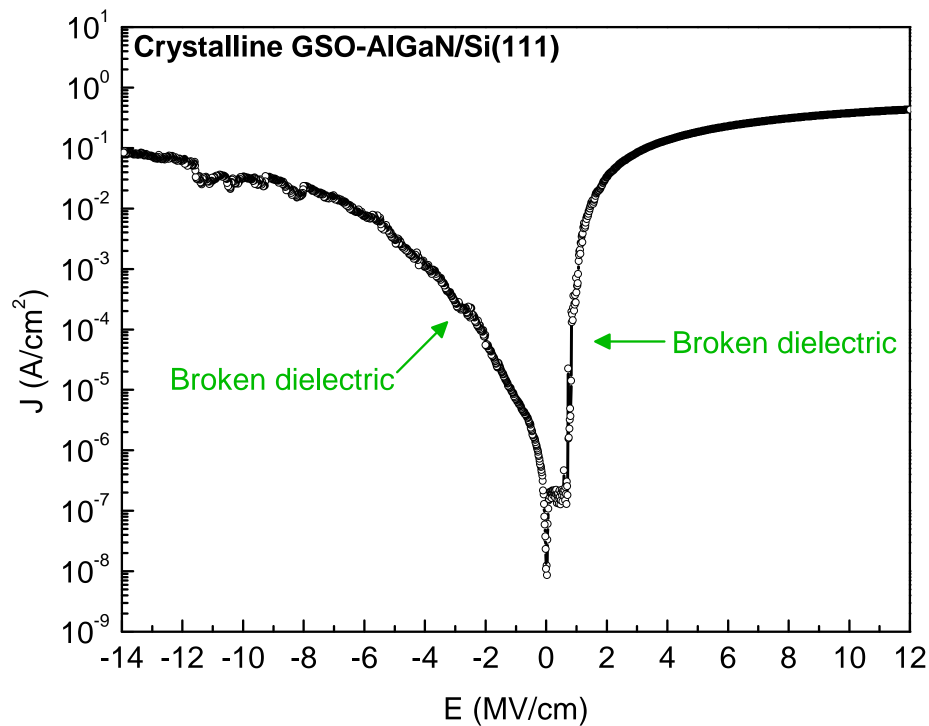

FIGURE 4.24: Average electrical behaviour of crystalline GSO-AlGaN/Si(111). The dielectric is broken on both positive and negative bias side: high density of pinholes seen in optical microscopy and TEM imaging is considered the responsible for the behaviour.

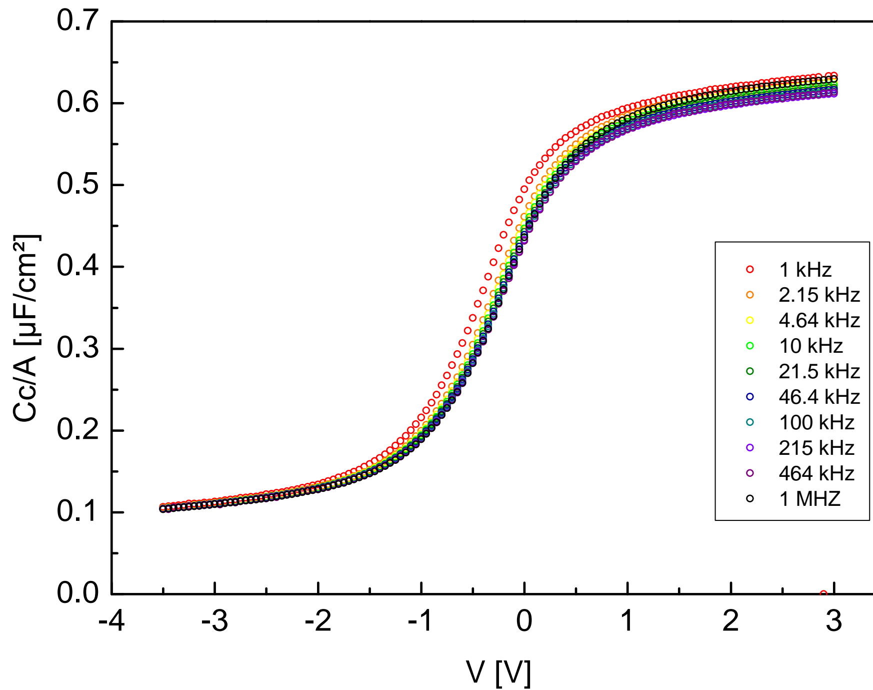

FIGURE 4.25: C-V multifrequency plot of crystalline GSO-GaN/Si(111). The MOS capacitor shows accumulation and depletion. The flatband voltage is located in negative bias, consistently with the n-type doping of GaN.

4.3.2 Capacitance-Voltage curves and determination of dielectric relative permittivity κ

The capacitance response to the application of a mixed continuous-alternated voltage (C-V) was tested for different capacitors with multi-frequency measurements, on crystalline GSO-GaN/Si(111) and crystalline LLO-GaN/Si(111). The applied bias consisted of a continuous voltage, sweeping between generally -3.5 V and +1.5÷+3.0 V, overlapped to a small-signal, harmonic, alternated voltage at a constant frequency. The frequency was tested between 1 kHz and 1 MHz on each capacitor.
Many trap-related properties can be derived from C-V behaviour with changing frequency of the MOS capacitor, but the main goal of the C-V measurements for the dielectric characterisation is to derive the relative permittivity κ of the oxide, for which the method formulated by S.Kar, exposed in section 2.3.2, was used. The method allows the extraction of the oxide capacitance even without reaching a strong accumulation regime where $C_{ox} \approx C_{accumulation}$. A sample of C-V multifrequency plot for crystalline GSO-GaN/Si(111) is shown in figure 4.25: on the y axis is displayed the capacitance normalised by the capacitor area and corrected by the measured series resistance (Cc/A).

Similar results were obtained for crystalline LLO-GaN/Si(111). The derivation of the relative permittivity according to the Kar method, for capacitance acquired at 100 kHz, lead to the results showed in table 4.6.

Therefore, the hexagonal crystalline GSO and LLO show a relatively high relative permittivity, suitable for considering the application of the oxides in high-κ dielectrics field; nonetheless, the staggered band alignment and consequently

System	Relative permittivity κ
GSO-GaN/Si(111)	21.2 ± 1.2
LLO-GaN/Si(111)	23.4 ± 0.1[2]

TABLE 4.6: Relative permittivity of the hexagonal single crystalline GSO and LLO grown epitaxially on GaN/Si(111).

asymmetric electrical behaviour precludes this possibility.
In this study, crystalline GSO shows a lower relative permittivity than crystalline LLO. This finds correspondence in literature, where generally ternary lanthanide-lanthanide rare earth oxides show higher permittivity with respect to ternary rare earth oxides containing Sc or Y. The relative permittivity can be affected by the quality of the semiconductor, as seen in section 4.4.2. The evaluation of the average CET from the dielectric capacitance resulted in slightly lower κ values, because of the slight underestimation of C_{ox} by the approximation $C_{ox} \approx C_a$.

4.4 TEM imaging of the oxide/III-V nitride interface

The interface between crystalline GSO and GaN was viewed in bright field cross-sectional TEM, in order to check the presence of interface layers and qualitatively evaluate the interface quality.
The GSO-GaN interface of crystalline GSO-GaN/Si(111) is shown in figure 4.26. The oxide and the III-V Nitride are both crystalline, with the lattice of GSO matching the lattice type of its GaN substrate. The difference in lattice parameter and in atomic radius of the elements in GSO and in GaN is visible to a close look to the image, consistently with the results achieved by XRD investigation.
The most important evidence emerging in the image is the presence of an interface layer between GaN and the GSO grown epitaxially on it. The nature of the interface layer is crystalline, suggesting it is not a native oxide or a chlorine contamination (described in section 4.2.1 on page 73) but rather part of the deposited film. The crystalline interface layer shows the same lattice parameters and ionic radius of the deposited oxide and lighter contrast, which in bright field TEM is associated to lighter atomic mass. Therefore, the epitaxial interface thin layer can be considered a Scandium segregation, referred as Sc-rich layer from now on.[3]

The same layer is present also at the GSO-GaN interface in crystalline GSO-GaN/Sapphire, as shown in figure 4.27.

4.4.1 Nature and influence of interface layers on asymmetry

TEM analysis of crystalline GSO-GaN/Si(111) and /Sapphire discussed up to now showed the presence of a Sc-rich, two-atoms thick interface layer between the semiconductor and the oxide. If the staggered band alignment is related to a

[3]The nature of the Sc-rich layer was confirmed by the TEM EDX mentioned at page 74, where the composition through the cross section is analysed: the layer results made of Sc_2O_3, with a following Gd segregation above to compensate the Sc depletion. From the composition profile it is probable that the non-uniformity is caused by Sc diffusion towards GaN from the stoichiometric layer. Further investigation is necessary to confirm the hypothesis.

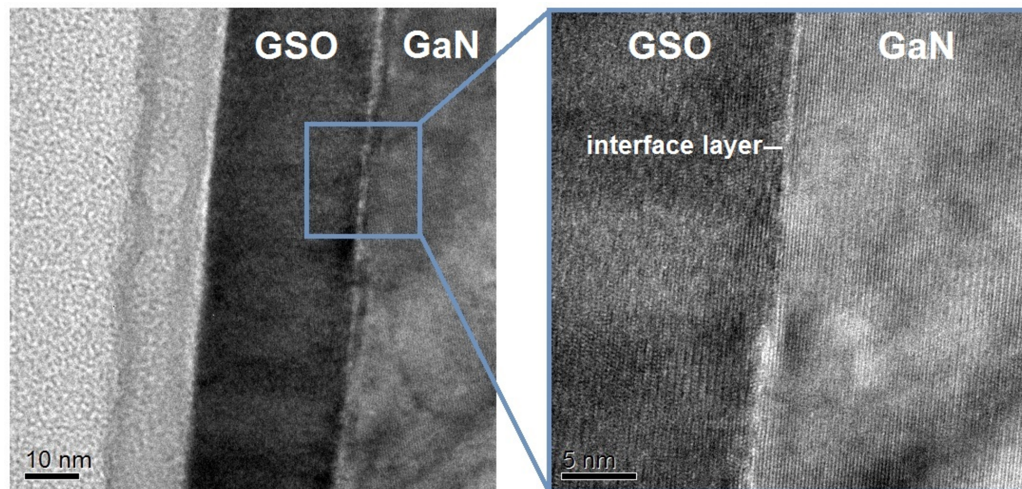

FIGURE 4.26: Bright Field TEM image of the interface between GSO and GaN in crystalline GSO-GaN/Si(111) (unmarked: glue). It is visible the lattice of both the phases and the presence of an interface layer of thickness ≈ two atoms. Considering the atomic density contrast and the aforementioned EDX (page 74) the interface layer is attributed to a Scandium segregation from $GdScO_3$.

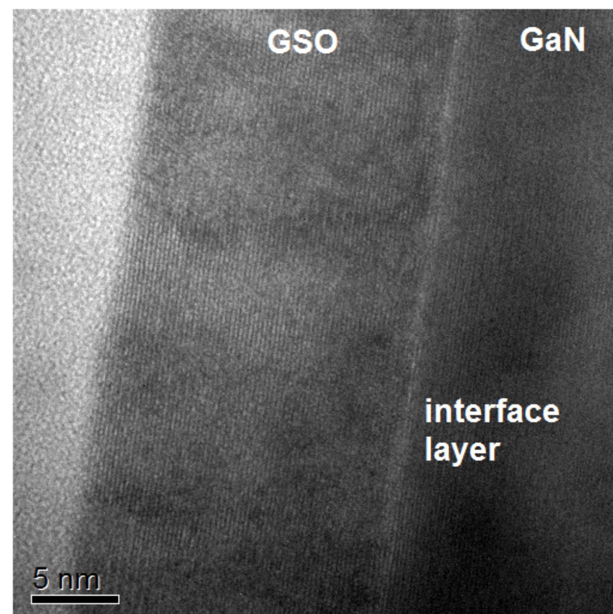

FIGURE 4.27: Bright Field TEM image of GSO-GaN interface in crystalline GSO-GaN/Sapphire. The Sc-rich interface layer is visible between GSO and GaN.

dipole effect at the GSO-GaN interface, **the Sc-rich layer may be the responsible for the peculiar asymmetry**.
Therefore, Sc-rich layer should be visible also in the amorphous GSO-GaN sample; the analogy of the interface between GSO-GaN/Si(111) and GSO-GaN/Sapphire suggests that the structural and quality differences between the two systems evidenced in section 4.1 play a marginal role in the overall staggered band alignment-asymmetric electrical behaviour, as all the systems showed it despite the more or less extended presence of defects; even GSO-AlGaN/Si(111) bands are staggered, despite the broken electric behaviour evident in section 4.3 and the defects that will be discussed further on (section 4.4.2). Therefore amorphous GSO-GaN/Si(111) is considered representative also for the same stack grown on sapphire substrate wafers.
TEM images of the amorphous GSO-GaN interface are shown in figure 4.28: as a confirmation of the hypothesis, the Sc-rich layer is clearly visible and similar to what seen in crystalline GSO-GaN interfaces, with the difference of three-atoms thickness instead of around two. It is important to notice that the layer is crystalline, despite the clear amorphous nature of the oxide layer above it: this assigns a significance to the very small peak found at $\approx 31°$ in the amorphous XRD θ-2θ spectrum shown in figure 4.2, which was previously dismissed as a local and negligible recrystallisation of the amorphous layer.

In figure 4.28b, the amorphous oxide layer is detached from the GaN (opinion from TEM experts and previous cases of failure suggest that the detachment happens during the TEM sample preparation, or anyway it is a local defect rather than a diffused situation through the sample surface), and the interface layer is still adherent to the substrate. The implication is that the major defects density is not at the (Sc-rich)-GaN interface, but at the amorphous GSO-(Sc-rich) one. It can be hypothesised that the Sc migration towards the GaN interface is driven by either:

- the better accommodation of lattice mismatch when the smaller-radius cation is over-stoichiometric;
- the dipole moment of Wurtzite dragging the more electronegative of the cations towards the interface.

The hypotheses can find confirmation or confutation by a TEM analysis of the LLO-GaN interface: La^{3+} has slightly bigger ionic radius than Lu^{3+}, for a lower nuclear charge is screened by the same inner shells electrons; electronegativity of Lu^{3+} is around 0.15 points larger than La^{3+} one, around the same difference between Sc^{3+} and Gd^{3+} where Sc is the more electronegative, as well as being the smaller of the two cations. Hence both a mismatch-driven and electrically-driven diffusion would induce a Lu-rich layer formation.
The investigation on the "extended Sc-rich" layer in LLO, and in all the samples that show the staggered band alignment, is a key analysis for a further understanding of the interface roles, and eventually their control and exploitation, in future.

4.4.2 Influence of dislocations and pinholes on performances

TEM imaging of GSO-AlGaN was acquired with the same sample preparation and operative conditions of GSO-GaN/Si(111) and GSO-GaN/Sapphire, and the interface imaging is shown in figure 4.29.

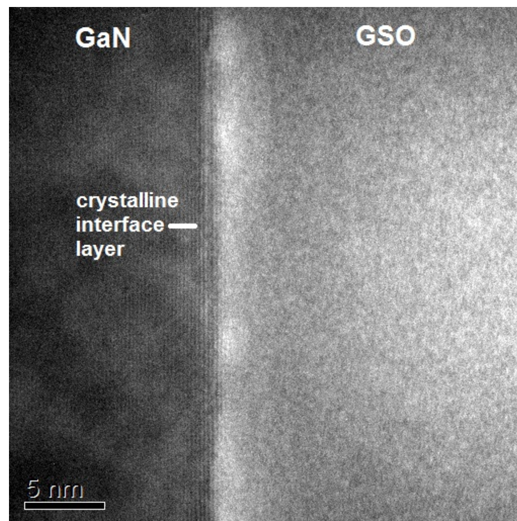

(A) TEM imaging of the amorphous GSO-GaN interface. The Sc-rich interface layer is present, and it is crystalline despite the amorphous nature of the oxide layer above.

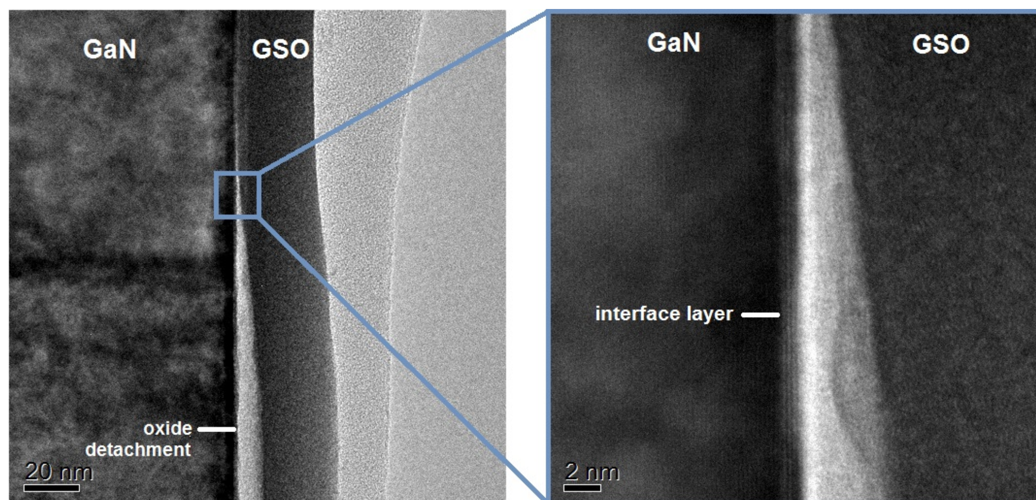

(B) detached oxide layer. The crystalline, Sc-rich interface layer is adherent to the GaN and the detachment surface is between the interface and the amorphous oxide. The interface layer has different lattice parameter than GaN.

FIGURE 4.28: Bright Field TEM imaging of the amorphous GSO-GaN/Si(111) interface.

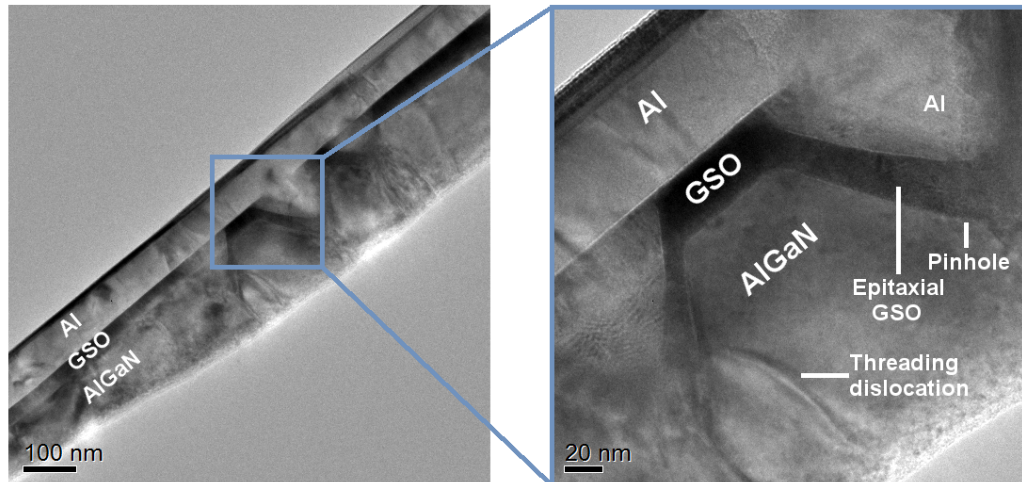

FIGURE 4.29: Bright Field TEM image of crystalline GSO-AlGaN/Si(111). Pinholes are visible in AlGaN and the growth of GSO occurred on the surface and inside the pinholes.

The image clearly shows the presence of threading dislocations through the MBE-deposited AlGaN and the pinholes generated from the III-V Nitride growth on dislocations, as mentioned in Chapter 1.4.1 on page 18. Moreover, it is possible to see that the PLD-deposited GSO grows in a relatively conformal way on top of AlGaN, disregarding the orientation of the substrate. Therefore, the oxide grows on the AlGaN flat (00l) surface and inside the pinholes, that are not (00l) surface oriented; the optical aberration of the TEM was not allowing the acquisition of a diffraction pattern localised enough to check the surface orientation of AlGaN and GSO inside the pinholes visible in the image, even though not appreciable signal from other crystallographic planes was visible in XRD θ-2θ scans. The pinhole is filled with Al from the e-beam deposition of the contacts for the fabrication of MOS capacitors. The epitaxial growth of GSO on AlGaN, evidenced by XRD analysis, induces a very high density of defects in the oxide, that therefore shows the early dielectric breakdown shown in the I-V plot in figure 4.24 on page 88.
Pinholes are present also in GaN, therefore the presence of a pinhole in GSO-AlGaN/Si(111) TEM sample could be considered a fortuitious event; nevertheless, pinholes were sensibly visible via optical microscopy in bright field, when the area of the contacts was measured in order to compute the current density and the normalised capacitance for I-V and C-V curves (the latter not shown in this work). The picture of crystalline GSO-AlGaN/Si(111) and crystalline GSO-GaN/Si(111) surface under the same conditions of light in the OM are shown in figure 4.30.

It is possible to notice that the surface is entirely covered in pinholes, unlike GaN. Assuming that the oxide grown inside the pinhole shows some growth defects at least at the bottom of the pinhole itself, or even threading dislocations through the entire dielectric layer, the immediate breakdown of the dielectric shown in all the I-V measurements taken on two crystalline GSO-AlGaN/Si(111) (of which a representative example is shown in figure 4.24) is reasonable.
In conclusion, the strain engineering buffer layer designed to absorb the dislocations, that would be produced in AlGaN from its direct growth on Si(111) because of lattice mismatches, did not prevent the dislocations propagation through the semiconductor: consequently, pinholes formation and induced defects in the oxide followed, enhancing greatly:

- the probability of immediate electric breakdown when a voltage of either polarity is applied to the capacitor;
- the bulk, oxide and interface traps availability, with a multitude of trapping-detrapping mechanisms activated at different frequencies of voltage alternation.

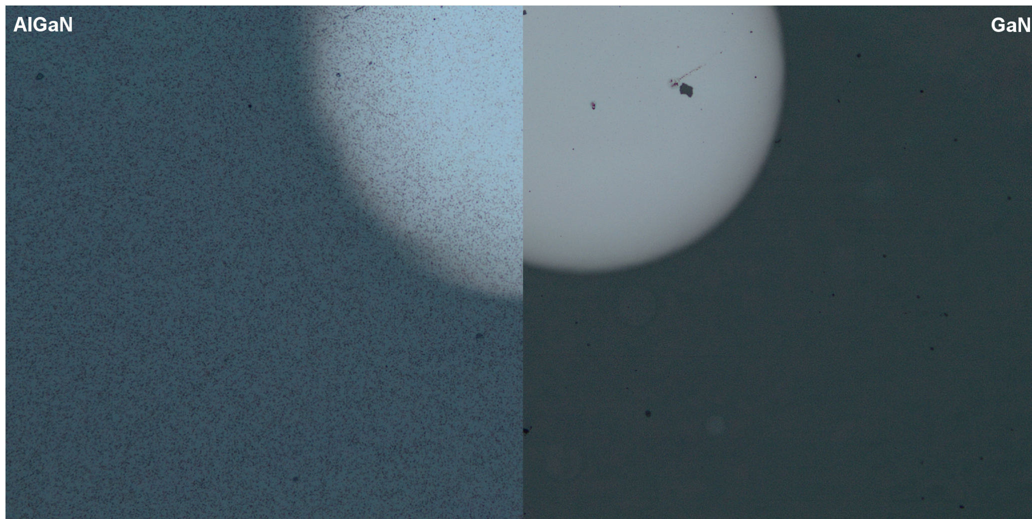

(A) surface comparison between AlGaN (high density of pinholes) and GaN (low density of pinholes).

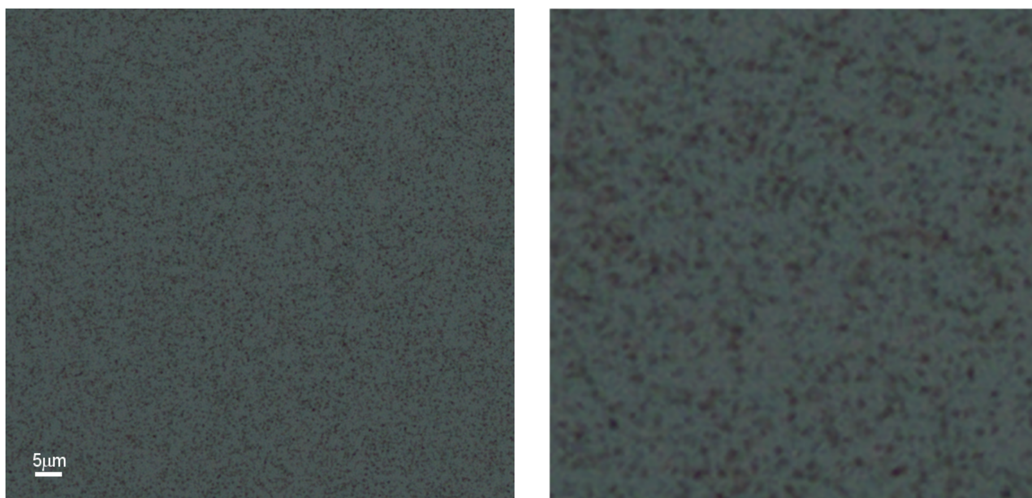

(B) close cut on the pinholes visible in AlGaN.

FIGURE 4.30: Bright Field optical microscopy shows the very high density of pinholes in AlGaN, responsible for the bad electrical behaviour of Al/GSO/AlGaN/Al capacitors.

Conclusion

This thesis work treats the characterisation of Rare Earth Oxide/III-V Nitride semiconductor systems for electronic applications. In particular, the goal of the research was the correlation between crystallographic structure and electronic properties with the electrical behaviour of the systems by means of analyses on MOS capacitors. The main system under analysis was crystalline GSO-GaN/Si(111), with further characterisation on amorphous GSO, crystalline LLO, AlGaN and GaN/Sapphire to better understand the role of the different components on the overall performance of the device.

The characterisation and correlation between the properties was successfully achieved. The main result experimentally emerged is that the band alignment between the rare-earth oxide and the III-V nitride semiconductor is unexpectedly **staggered** in all the systems, in that the valence band offset measured from XPS valence band spectra is very large and, as a result of the high band gap of the semiconductors, the conduction band of GaN and AlGaN is higher in energy than the conduction band of GSO and LLO, disregarding the crystalline or amorphous nature of the oxide, which nature was confirmed with XRD analysis and will be discussed further on. The staggered band alignment found a confirmation in the **asymmetric electrical response** of the systems: the dielectric breakdown happens much earlier when applying a positive bias to the MOS capacitors with respect to the application of a negative bias. In fact, the electrons driven by a positive bias do not feel any potential barrier flowing from the semiconductor to the oxide and gate electrode, and the only hindrance to a free electron flow is provided by the resistive nature of the oxide; in the opposite case, instead, the potential barrier to which the electrons are subjected sums to the ohmic contribution and determines a difference in positive and negative breakdown strength of the systems. GSO-AlGaN always showed a broken dielectric behaviour disregarding the bias: various analyses evidenced how this is related to a poor quality of the oxide induced by an extremely high density of defects in the semiconductor, as will be discussed along this chapter.
The epitaxy of the crystalline GSO on GaN was confirmed by XRD analyses that showed an hexagonal phase on Wurtzite GaN, where the GSO cell parameters emerged to be larger than the GaN ones, meaning that the oxide layer is relaxed on the semiconductor and therefore defects (dislocations) in the oxide close to the interface are expected. The same trend was seen for crystalline LLO-GaN and GSO-AlGaN, leading to larger lattice mismatches with respect to GSO-GaN. The substrate wafer, Si(111) and Sapphire, was seen to influence the crystalline quality of GaN layer that is mirrored in the quality of the oxide, as expected by the epitaxial growth. In particular, GaN on Sapphire is less defective, and that can be the reason for the lower series resistance measured electrically as well as the earlier dielectric breakdown under positive bias with respect to GSO-GaN/Si(111), reminding that in the positive bias case the dielectric breakdown strength is only

given by a resistive contribution, since the band alignment is staggered. Small fluctuations in the oxide lattice parameters were seen in GSO-GaN deposited on the two different substrates, meaning that the defects density in the semiconductor induced by the mismatch with the substrate wafer is relevant on the oxide growth. This is also evident from electric measurements on the two systems, and it can be hypothesised that the AlGaN semiconductor, and consequently GSO deposited on it, is extremely defective for the same growth problems on Si(111). The amorphous oxide nature was confirmed by XRD measurements as well. While the crystal or amorphous nature of the oxides was evaluated by XRD, the chemical bonds involved in the two phases were evidenced in XPS measurements. The main results in this thread were that there have not been seen any Ga-O bonds, meaning that no native oxide is present or formed prior and during the deposition of the rare earth oxides. On the side of the GSO and LLO, high hygroscopicity of the oxides was revealed. The entity of the water chemisorption can be related to the defectiveness of the oxide layer especially considering the difference between GSO-GaN and GSO-AlGaN, the latter showing a much larger hygroscopicity. Capacitance-Voltage measures allowed to determine the dielectric capacitance in the stack and therefore the relative permittivity of the high-κ oxide. The κ value is > 20 with LLO having a higher permittivity than GSO, aligned with the trends in rare earth oxides found in literature. This corresponds to a SiO_2 equivalent thickness of around 4÷5 nm, declaring hexagonal GSO and LLO fully eligible for the use as high-κ dielectrics in semiconductor industry. To this purpose, XRR measurements were used to evaluate the thickness of the oxide layer and the confirmation of the validity of the XRR values were seen in TEM imaging. The reasons for the staggered band alignment were investigated by looking for an interface layer by electron microscopy (TEM). The images captured for crystalline GSO-GaN/Si(111), crystalline GSO-GaN/Sapphire and amorphous GSO-GaN/Si(111) all showed a **crystalline, 2-3 atoms thick, Sc-rich interface layer**. The formation of the layer is hypothesised to be stress-driven or dipole-driven, because of the lattice mismatch between GSO and GaN seen with XRD analyses that drags the smaller ionic radius atom towards the interface or because of the fact that Wurtzite GaN has a net dipole moment caused by its lack of inversion symmetry. TEM of LLO-GaN interface can clarify the formation mechanism and confirm the main hypothesis that the **interface layer causes the band alignment to be staggered**. The TEM imaging of GSO-AlGaN interface consists of a further confirmation of the extremely high pinholes and dislocations density of the semiconductor, mirrored in the oxide layer, and therefore justifies the high leakages seen in current-voltage measurements.

The Rare Earth Oxide/III-V Nitride semiconductor systems therefore showed good dielectric properties technically suitable for a use in MOS gate stacks, but also staggered band alignment that prevents this application because of the unwanted current flow of carriers from channel to gate under positive bias. Considering that the staggered band alignment is linked to the interface layer between the III-V nitride and the ternary rare earth gate dielectric, its elimination would probably result in a straddling band alignment, with a conduction band offset large enough to allow its use in microelectronics; alternatively, a control on the interface layer can be exploited for considering the GSO-GaN and related stacks in other applications that require a charge separation, achieved by the heterojunction of materials with an overall staggered band alignment. Photodetectors, solar cells,

generators for water splitting are just some examples. These devices can benefit of the high temperature, high voltage and hard radiation resistance of GaN, the chemical inertness of the rare earth oxides and very different bandgaps available for transitions.

Hints for further work therefore lie in a deeper understanding of the main peculiarity of these systems and the factor that generates it. Summarising:

- **TEM imaging of LLO-GaN interface** to confirm the formation of the interface layer for every ternary rare earth oxide;
- **workfunction measurements**, to unveil how the staggered band alignment of GSO-GaN affects the overall MOS properties, beyond the leakage of current under positive bias;
- characterisation of **GSO-AlGaN systems** with less defective growth and quantification of the effects of an even larger lattice mismatch, with a view to the future implementation of different bandgaps in devices by tuning the nitride composition;
- understand the **mechanism of formation of the crystalline interface layer**, in order to prevent it, control it or tune its effect for actual devices applications.

Appendix A

Samples preparation

The samples were produced externally in Forschungzentrum Jülich. The growth process can be divided in three phases:

1. III-V Nitride MBE growth on the substrate wafer;
2. rare earth oxide PLD growth on the III-V nitride layer;
3. contact metallisation (Al) on the PLD-deposited oxide layer.

An additional step was performed in the Technion for achieving a metal contact with the semiconductor by reactive ion etching and subsequent metallisation of the exposed strip.

GaN and AlGaN were grown by molecular beam epitaxy (MBE) onto the substrate wafer, up to a thickness of $\approx$ 1000 nm and 500 nm respectively. The doping is of n-type and the density of electron donors is $\approx 10^{18}$ Si $^{atoms}/_{cm^3}$. GaN/Sapphire was produced in Forschungzentrum Jülich, directly on Al_2O_3: the strain caused by the sapphire-GaN lattice mismatch is absorbed by a first undoped GaN layer. GaN/Si(111) and AlGaN/Si(111) were bought from an external producer[1]. The MBE deposition of the nitride was preceded by a buffer layer to absorb the mismatch-induced strain: the superlattice design and composition is unknown for commercial reasons.
Afterwards, the wafer was diced in 10x10 mm samples and cleaned of surface contamination by a H_2SO_4/HCl mixture for all the samples produced.
Pulsed laser deposition was used to deposit GdScO3 and LaLuO3 epitaxially, excluding the bare nitride samples. In a vacuum chamber a pulsed, highly energetic laser was focused on a rotating target and, for a sufficient laser energy density, the target material is heated until it evaporates or forms a plasma. The plasma ions are adsorbed on the sample surface building up a thin film. Epitaxial growth was enabled by heating the sample with a SiC heater.
A KrF excimer laser with a wave length of 248 nm, a pulse width of 20 ns and a fluence of $\approx 5\ ^{J}/_{cm^2}$ at a repetition rate of 10 Hz was used in an oxygen ambient, with an oxygen partial pressure $\geq 10^3$ mBar.
The LaLuO3 and GdScO3 targets were produced of powders of 99.99% La2O3, Lu2O3, Gd2O3 and Sc2O3. The powders were mixed, ball milled in isopropanol for 24 h, calcined at 1300°C for 24 h, pressed into 25mm diameter targets and finally sintered at 1500°C for 12 h.[77]

[1]Novagan, EPFL Innovation Park PSE-D, 1015 Lausanne, Switzerland

The contacts deposition made in Jülich was performed by e-beam evaporation through a mask for the square contacts of the MOS capacitors and the Al side strip of the substrate contact. The latter was deposited on top of the oxide layer, for the series resistance and capacitance given by the oxide underneath the contact were considered negligible due to the much larger area. All the metallic contacts were 100 nm thick.

The achievement of a direct metal-semiconductor body contact from this configuration was executed in a second phase, in the Technion. The MOS capacitors were covered with Kapton tape, exposing the lateral strip only. The exposition of GaN was obtained by reactive ion etching (RIE) through the metal and oxide layers using a mixture of CF4 and O2 at $P < 5$ mTorr, room temperature and RF power of 175 W.
The etching was followed by 100 nm Al deposition by e-gun on the exposed GaN. Series resistance measures in C-V experiments showed that it is sensibly lowered (from 500 Ω to 200 Ω for GSO-GaN/Si(111)) with the achievement of a direct metal-semiconductor contact.

Bibliography

[1] S. M. Sze. *Physics of semiconductor devices*. Wiley, 1981, p. 815.
[2] S. O. Kasap. *Principles of electronic materials and devices*. McGraw-Hill, 2006, p. 874.
[3] Yuan Taur and Tak H. Ning. *Fundamentals of Modern VLSI Devices*. 2nd. Cambridge University Press, 1998, p. 149.
[4] Angus I. Kingon, Jon-Paul Maria, and S. K. Streiffer. "Alternative dielectrics to silicon dioxide for memory and logic devices". In: *Nature* 406.6799 (2000), pp. 1032–1038.
[5] Gordon E Moore. "Cramming More Components onto Integrated Circuits". In: *Electronics* 38 (1965), pp. 114–117.
[6] *International Technology Roadmap for Semiconductors - ITRS 2.0 Home Page*. 2015.
[7] John Robertson and Robert M. Wallace. "High-K materials and metal gates for CMOS applications". In: *Materials Science and Engineering: R: Reports* 88 (2015), pp. 1–41.
[8] S.-H. Lo et al. "Quantum-mechanical modeling of electron tunneling current from the inversion layer of ultra-thin-oxide nMOSFET's". In: *IEEE Electron Device Letters* 18.5 (1997), pp. 209–211.
[9] Daniel J. Lichtenwalner et al. "Overview of Materials Processing and Properties of Lanthanum-Based High-k Dielectrics". In: *ECS Transactions*. Vol. 11. 4. ECS, 2007, pp. 319–332.
[10] I.A. Bondar. "Rare-earth silicates". In: *Ceramics International* 8.3 (1982), pp. 83–89.
[11] Daniel J. Lichtenwalner et al. "Lanthanum silicate gate dielectric stacks with subnanometer equivalent oxide thickness utilizing an interfacial silica consumption reaction". In: *Journal of Applied Physics* 98.2 (2005), p. 024314.
[12] Apurba Laha et al. "Crystalline ternary rare earth oxide with capacitance equivalent thickness below 1nm for high-k application". In: *Applied Physics Letters* 88.17 (2006), p. 172107.
[13] Jürgen Schubert, Tassilo Heeg, and Martin Wagner. "Fabrication and Characterization of Rare Earth Scandate Thin Films Prepared by Pulsed Laser Deposition". In: *Rare Earth Oxide Thin Films* 126 (2007), pp. 115–126.
[14] Daniel J. Lichtenwalner. "Lanthanide-Based High-k Gate Dielectric Materials". In: Springer Berlin Heidelberg, 2013, pp. 343–369.
[15] H. Alshareef et al. "Thermally Stable N-Metal Gate MOSFETs Using La-Incorporated HfSiO Dielectric". In: *2006 Symposium on VLSI Technology, 2006. Digest of Technical Papers.* IEEE, 2006, pp. 7–8.
[16] Matthias Passlack. "Methodology for Development of High-κ Stacked Gate Dielectrics on III–V Semiconductors". In: *Materials Fundamentals of Gate Dielectrics*. Berlin/Heidelberg: Springer-Verlag, 2005, pp. 403–467.
[17] John Robertson et al. "Electronic Structure and Band Offsets of High-Dielectric-Constant Gate Oxides". In: *MRS Bulletin* 27.03 (2002), pp. 217–221.
[18] Yi Zhao et al. "Moisture-absorption-induced permittivity deterioration and surface roughness enhancement of lanthanum oxide films on silicon". In: *Applied Physics Letters* 88.7 (2006), p. 072904.
[19] Giovanna Scarel, Axel Svane, and Marco Fanciulli. "Scientific and Technological Issues Related to Rare Earth Oxides: An Introduction". In: *Rare Earth Oxide Thin Films*. Springer Berlin Heidelberg, 2007, pp. 1–14.

[20] Theodosia Gougousi. “Postdeposition reactivity of sputter-deposited high-dielectric-constant films with ambient H[sub 2]O and carbon-containing species”. In: *Journal of Applied Physics* 95.3 (2004), p. 1391.

[21] P. D. Kirsch et al. “Mobility and charge trapping comparison for crystalline and amorphous HfON and HfSiON gate dielectrics”. In: *Applied Physics Letters* 89.24 (2006), p. 242909.

[22] H. J. Osten et al. “Introducing crystalline rare-earth oxides into Si technologies”. In: *physica status solidi (a)* 205.4 (2008), pp. 695–707.

[23] G. Scarel et al. “Erratum: “Vibrational and electrical properties of hexagonal La[sub 2]O[sub 3] films” [Appl. Phys. Lett. 91, 102901 (2007)]”. In: *Applied Physics Letters* 91.18 (2007), p. 189901.

[24] A. M. Herrero et al. “Epitaxial growth of Sc[sub 2]O[sub 3] films on GaN”. In: *Applied Physics Letters* 89.9 (2006), p. 092117.

[25] M. Wagner et al. “Preparation and characterization of rare earth scandates as alternative gate oxide materials”. In: *Solid-State Electronics* 50.1 (2006), pp. 58–62.

[26] J. M. J. Lopes et al. “Amorphous lanthanum lutetium oxide thin films as an alternative high-κ gate dielectric”. In: *Applied Physics Letters* 89.22 (2006), p. 222902.

[27] G. K. Celler and Sorin Cristoloveanu. “Frontiers of silicon-on-insulator”. In: *Journal of Applied Physics* 93.9 (2003), pp. 4955–4978.

[28] Sorin Cristoloveanu. “Silicon on insulator technologies and devices: From present to future”. In: *Solid-State Electronics* 45.8 (2001), pp. 1403–1411.

[29] Shinichi Takagi et al. “III – V / Ge channel MOS device technologies in nano CMOS era”. In: *Japanese Journal of Applied Physics* 54.6S1 (2015).

[30] Yoshiki Kamata. “High-k/Ge MOSFETs for future nanoelectronics”. In: *Materials Today* 11.1 (2008), pp. 30–38.

[31] Jesus A. Del Alamo et al. “Nanometer-Scale III-V MOSFETs”. In: *IEEE Journal of the Electron Devices Society* 4.5 (2016), pp. 205–214.

[32] Class for Physics of the Royal Swedish Academy of Sciences. “Efficient blue light-emitting diodes leading to bright and energy-saving white light sources”. In: *Scientific Background on the Nobel Prize in Physics 2014* 50005 (2014), pp. 1–9.

[33] Jong Kyu Kim et al. “Enhanced light-extraction in GaInN near-ultraviolet light-emitting diode with Al-based omnidirectional reflector having NiZn/Ag microcontacts”. In: *Applied Physics Letters* 89.14 (2006), pp. 1–4.

[34] Farid Medjdoub and Krzytsztof Iniewski. *Gallium nitride (GaN) : physics, devices, and technology*. 1st ed. Taylor & Francis Group, LLC, 2016, p. 362.

[35] R.F. Davis. “III-V nitrides for electronic and optoelectronic applications”. In: *Proceedings of the IEEE* 79.5 (1991), pp. 702–712.

[36] Harald Ibach and Hans Lüth. “Semiconductors”. In: *Solid-State Physics*. Berlin, Heidelberg: Springer Berlin Heidelberg, 2009, pp. 419–515.

[37] Wenliang Wang et al. “Epitaxial growth of GaN films on unconventional oxide substrates”. In: *J. Mater. Chem. C* 2.44 (2014), pp. 9342–9358.

[38] Subramaniam Arulkumaran and Geok Ing Ng. “Gallium Nitride Transistors on Large-Diameter Si(111) Substrate”. In: *GaN: Physics, Devices and Technology*. 2016.

[39] F. Roccaforte et al. “Recent advances on dielectrics technology for SiC and GaN power devices”. In: *Applied Surface Science* 301 (2014), pp. 9–18.

[40] Basanta Roul et al. “Binary group III-nitride based heterostructures: band offsets and transport properties”. In: *Journal of Physics D: Applied Physics* 48.42 (2015), p. 423001.

[41] Rüdiger Quay. “Group III-Nitride Microwave Monolithically Integrated Circuits”. In: *GaN: Physics, Devices and Technology*. 2016. Chap. 5.

[42] E. Bahat-Treidel. “GaN-Based HEMTs for High Voltage Operation”. PhD thesis. 2012, pp. 1132–1134.

[43] S. J. Pearton. *GaN and related materials*. Gordon and Breach, 1997, pp. 295–6.

[44] P. Dogan, C. Chèze, and R. Calarco. “III-V semiconductor nanowires: Nitrides (N-based; III-N)”. In: *Semiconductor Nanowires Materials, Synthesis, Characterization and Applications*. Elsevier Inc., 2015, pp. 125–145.

[45] Annamraju Kasi Viswanath. “GaN Nanostructure-based light emitting diodes and semiconductor lasers”. In: *Journal of Nanoscience and Nanotechnology* 14.2 (2014), pp. 1947–1982.

[46] Mark Beeler and Eva Monroy. “III-Nitride Semiconductors: New Infrared Intersubband Technologies”. In: *GaN: Physics, Devices and Technology*. 2016.

[47] S. J. Pearton et al. “Review—Ionizing Radiation Damage Effects on GaN Devices”. In: *ECS Journal of Solid State Science and Technology* 5.2 (2016), Q35–Q60.

[48] Miaoling Que et al. “Progress in piezo-phototronic effect modulated photovoltaics”. In: *Journal of Physics of Condensed Matter* 28.43 (2016).

[49] Eric Higham. “GaN technology in base stations - Why and when?” In: *Technical Digest - IEEE Compound Semiconductor Integrated Circuit Symposium, CSIC* (2014).

[50] K. Matocha, T.P. Chow, and R.J. Gutmann. “High-Voltage Normally Off GaN MOSFETs on Sapphire Substrates”. In: *IEEE Transactions on Electron Devices* 52.1 (2005), pp. 6–10.

[51] A. Perez-Tomas et al. “GaN transistor characteristics at elevated temperatures”. In: *Journal of Applied Physics* 106.7 (2009), p. 074519.

[52] Keisuke Shinohara. “GaN-HEMT Scaling Technologies for High Frequency Radio Frequency and Mixed Signal Applications”. In: *GaN: Physics, Devices and Technology*. 2016.

[53] Mina Rais-Zadeh et al. “Gallium nitride as an electromechanical material”. In: *Journal of Microelectromechanical Systems* 23.6 (2014), pp. 1252–1271.

[54] Thomas E. Kazior. “Beyond Cmos: Heterogeneous integration of III-V devices, RF MEMS and other dissimilar materials/devices with Si CMOS to create intelligent microsystems”. In: *Philosophical Transactions of the Royal Society A: Mathematical, Physical and Engineering Sciences* 372.2012 (2014).

[55] E. H. Nicollian and J. R. Brews. *MOS (metal oxide semiconductor) physics and technology*. Wiley-Interscience, 2003, pp. 71–75.

[56] J. M. Ziman. *Principles of the Theory of Solids*. 2nd ed. Cambridge: Cambridge University Press, 1972.

[57] Neil W. Ashcroft and N. David. Mermin. *Solid state physics*. Saunders College Pub, 1976, p. 826.

[58] Richard D. Deslattes. “X-RAY MONOCHROMATORS AND RESONATORS FROM SINGLE CRYSTALS”. In: *Applied Physics Letters* 12.4 (1968), p. 133.

[59] Won-Sik Han, Sang-Ook Kang, and Il-Hwan Su. “An Easier Way to Calculate the Crystallographic Interplanar Angles”. In: *Korean J. Crystallography* 18.1,2 (2007), pp. 7–9.

[60] Katsuhiko Inaba et al. “High Resolution X-Ray Diffraction Analyses of (La,Sr)MnO₃/ZnO/Sapphire(0001) Double Heteroepitaxial Films”. In: *Advances in Materials Physics and Chemistry* 03.01 (2013), pp. 72–89.

[61] Pini Shekhter et al. “Epitaxial NiInGaAs formed by solid state reaction on In0.53Ga0.47As: Structural and chemical study”. In: *Journal of Vacuum Science & Technology B: Microelectronics and Nanometer Structures* 31.3 (2013), p. 031205.

[62] Jens Als-Nielsen and Des McMorrow. *Elements of Modern X-ray Physics*. Hoboken, NJ, USA: John Wiley & Sons, Inc., 2011.

[63] L. G. Parratt. “Surface Studies of Solids by Total Reflection of X-Rays”. In: *Physical Review* 95.2 (1954), pp. 359–369.

[64] P. Colombi et al. “Reproducibility in X-ray reflectometry: results from the first world-wide round-robin experiment”. In: *Journal of Applied Crystallography* 41.1 (2008), pp. 143–152.
[65] Emil Zolotoyabko. “Extended Kinematic Approach to the Simulation of High-Resolution X-ray Diffraction Spectra. Application to Structures with Buried Amorphous Layers”. In: *J. Appl. Cryst* 31 (1998), pp. 241–251.
[66] David Briggs and Martin P Seah. *Practical surface analysis by Auger and X-ray photoelectron spectroscopy*. Ed. by David Briggs and Martin P. Seah. 2nd. 1990, p. 533.
[67] J. C. Vickerman and Ian S. (Ian Stuart) Gilmore. *Surface analysis : the principal techniques*. Wiley, 2009, p. 666.
[68] Alexander V. Naumkin et al. *NIST X-ray Photoelectron Spectroscopy (XPS) Database, Version 3.5*.
[69] Seiichi Miyazaki. “Characterization of high-k gate dielectric/silicon interfaces”. In: *Applied Surface Science* 190.1 (2002), pp. 66–74.
[70] Dieter K. Schroder. *Semiconductor material and device characterization*. IEEE Press, 2006, p. 779.
[71] S. Kar. “Extraction of the capacitance of ultrathin high-K gate dielectrics”. In: *IEEE Transactions on Electron Devices* 50.10 (2003), pp. 2112–2119.
[72] R. Carin, J. P. Deville, and J. Werckmann. “An XPS study of GaN thin films on GaAs”. In: *Surface and Interface Analysis* 16.1-12 (1990), pp. 65–69.
[73] Jan Hedman and Nils Mårtensson. “Gallium nitride studied by electron spectroscopy”. In: *Physica Scripta* 22.2 (1980), pp. 176–178.
[74] S. D. Wolter et al. “Kinetic Study of the Oxidation of Gallium Nitride in Dry Air”. In: *Journal of The Electrochemical Society* 145.2 (1998), p. 629.
[75] S. W. King et al. “Cleaning of AlN and GaN surfaces”. In: *Journal of Applied Physics* 84.9 (1998), p. 5248.
[76] Junqiao Wu. “When group-III nitrides go infrared: New properties and perspectives”. In: *Journal of Applied Physics* 106.1 (2009), p. 011101.
[77] Anna Barbara Schaefer. “Growth and characterization of crystalline rare-earth based thin oxide films for the application as gate dielectric in nanotechnology”. PhD thesis. 2015.

Acknowledgements

This was a ride. I would like to give my very warm thanks to Moshe, for giving me this great opportunity but especially for the countless remarks, comments and advises through the entire work. Special thanks to Pini, for leading me through the learning process, helping me on the way - including answering to calls at ungodly hours during the overnights -, and to put up with all those green lines; to Roy, Sivan, Katia, Yehiel, Kami and Avi for the fundamental help with experiments. A more light-hearted thanks to all my colleagues already mentioned as well as not, because it was just great to share time, working place, coffees, bursts of laugh and Hebrew notions all the time. May the molestia be with you.
Furthermore I would like to thank Uli Tromm and Jürgen Schubert from Forschungzentrum Jülich for the samples fabrication and the cooperation with results.
Last but not least, I would like to thank my supervisor Carlo Casari for all the work and help from remote, and of course the patience during the thesis redaction.

Vorrei come sempre ringraziare la mia famiglia, estesa così com'è, per supportarmi e sopportarmi nelle mie scelte di studio e di vita sempre più anomale; un ringraziamento speciale alla mia sorellina Elena, meravigliosa disturbatrice della quiete.

Ringrazio infine moltissimo tutti i miei amici e compagni di viaggio, che vorrei davvero nominare uno ad uno, e su cui come sempre spicca Luca Crippa per la simbiosi che ci lega da anni.
To my friends in Israel and in the Technion: mention is needed for Angela, Josie, Er Crocchetta, Er Moscardino, Leon, the ladies from Haifa Rugby and the Pandas (healthy or broken), but my thanks are to every person met, every story shared, every soul touched. This experience would not have been half as fully incredible without you!

Sara